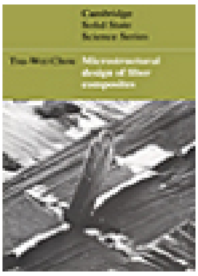

Microstructural Design of Fiber Composites

Tsu-Wei Chou

Book DOI: http://dx.doi.org/10.1017/CBO9780511600272

Online ISBN: 9780511600272

Hardback ISBN: 9780521354820

Paperback ISBN: 9780521019651

Chapter

6 - Two-dimensional textile structural composites pp. 285-373

Chapter DOI: http://dx.doi.org/10.1017/CBO9780511600272.007

Cambridge University Press

6 Two-dimensional textile structural composites

6.1 Introduction

The term 'textile structural composites' is used to identify a class of advanced composites utilizing fiber preforms produced by textile forming techniques, for structural applications. The recent interest in textile structural composites stems from the need for improvements in intra- and interlaminar strength and damage tolerance, especially in thick-section composites. Textile composites offer the potential of providing adequate structural integrity as well as shapeability for near-net-shape manufacturing (Chou and Ko 1989).

Textile structural composites provide the unique capability that the microstructure of fiber preforms can be designed to meet the needs of the performance of composite structures. Textile structural composites can be fabricated directly to their final shapes or can be assembled or readily machined to specified contours and dimensions. A total system approach is necessary to optimize the composite performance through the consideration of preform availability, cost, ease of processing, needs for secondary work such as machining, joinability of parts, and the overall performance of the composite structure. Chapters 6 and 7 discuss the fundamental characteristics of two- and three-dimensional textile preforms and the analysis of composite behavior based upon these preforms. The following discussions of yarn assembly, as well as textile preforms and characteristics, are based upon the review of Scardino (1989).

The forming of textile preforms requires knowledge of the structure of yarns and fibers. Yarns are linear assemblages of fibers formed into continuous strands having textile characteristics, i.e. substantial strength and flexibility. Figure 6.1 illustrates the idealized models of yarn structures; a yarn may consist of (a) single or (b) multiple continuous fibers, or (c) short (*staple*) fibers, where a substantial amount of twist or entanglement is needed to overcome fiber slippage. Yarns made from staple fibers are referred to as *spun yarns*. Figure 6.1(d) and (e) show that two or more single yarns can be twisted together to form ply or plied yarns. Plied yarns can be further twisted to form multiples (f). Spun yarns can also be combined to form plied yarns. Advanced textile structural composites are mostly based upon continuous filament yarns.

The relative density of fiber packing in the yarn cross-section is quantified by the fiber packing fraction, which is the ratio of fiber specific volume (volume/mass) to yarn specific volume. Fiber packing fractions are determined by a number of factors, including the number of fibers in a yarn, fiber cross-sectional shape, yarn tension, level of yarn twist and yarn manufacturing method. The yarn structures determine the translation of fiber properties into yarn properties. Consider, for example, the axial yarn elastic modulus (E_y). Hearle, Grosberg and Backer (1969) have predicted that $E_y = \cos^2\theta E_f$, where E_f is the fiber elastic modulus and θ denotes the helical angle of the fibers in a yarn. The translation efficiencies reflect the effect of fiber orientation relative to the yarn axis due to the twist as well as the fiber entanglement in the yarns. The efficiency of fiber packing in a yarn and the fiber-to-yarn strength and modulus translation need to be taken into account in the selection of yarns for textile preforms. Further discussions on the packing of fibers in a yarn are given in Chapter 7.

The selection of fiber preforms as reinforcements for composites requires additional considerations to those at the yarn level. The most basic ones, according to Scardino, are the manipulative requirements in dimensional stability, subtle conformability and

Fig. 6.1. Idealized models of various yarn structures. (After Scardino 1989.)

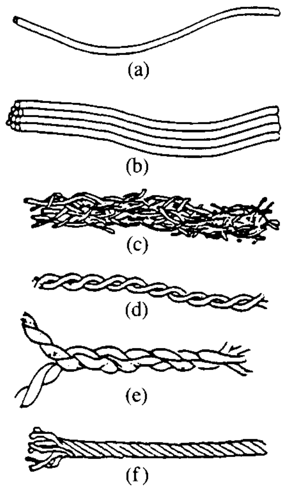

deep draw shapeability. A high degree of dimensional stability is required in pultruded, flat panel or laminated composites. Some conformability is desirable in slightly curved structural parts. Considerable extensibility of the preform is necessary for deep-draw molded composites. These factors not only are pertinent to the selection of composites processing techniques, but also dominate the fiber preform microstructure in the finished product. It should be noted that the orientations of fibers in a preform before and after matrix impregnation can be very different, and can thus have significant implication on composite performance.

6.2 Textile preforms

The major textile forming techniques for composites reinforcement are weaving, knitting, braiding and stitching. There is the lack of a definitive criterion for separating textile preforms into the two-dimensional and three-dimensional types. In Chapters 6 and 7, a rather loose criterion is applied to distinguish these two types, based upon the degree of integration of the yarns as well as the extent of strengthening in the thickness direction of the preform. Consider, for instance, the traditional weaving, knitting and braiding processes; the interaction of yarns (i.e. interlacing, interlooping) in the thickness direction is limited to two or three yarn diameters. As a result, the strengthening effect due to yarn penetration, although higher than that for conventional laminated composites, is fairly small. Therefore, these preforms are considered to be two dimensional. On the other hand, the more recently developed preforms, such as angle-interlock wovens and solid braids, are fully integrated structures, and there is a significant degree of strengthening in the thickness direction. Thus, these preforms can be categorized as three-dimensional. The foregoing definitions are independent of the actual dimensions of the preform.

The uncertainty in the separation of two- and three-dimensional preforms arises when the integration of yarns in the thickness direction is of limited extent and the resulting strengthening is not very significant. An example can be found in multiaxial warp knits. The layers of essentially straight fibers in such a construction are connected by knitting yarns. The degree of strengthening in the thickness direction depends on the type of knitting yarns used.

Figure 6.2 summarizes the major manufacturing techniques for two-dimensional textile preforms. It is feasible to insert laid-in yarns into the basic knitted or braided fabric given in Fig. 6.2, thus significantly modifying the directional stability of the fabric. The great varieties of fabric geometry so induced are not shown in Fig. 6.2 for the reason of simplicity. A brief discussion of wovens, knits and braids for reinforcing composites is given below.

6.2.1 *Wovens*

Woven fabrics, formed on a loom by interlacing two or more sets of yarns, are essentially two-dimensional constructions. When two sets of yarns are interlaced at right angles, the lon-

Fig. 6.2. Manufacturing techniques for two-dimensional textile preforms.

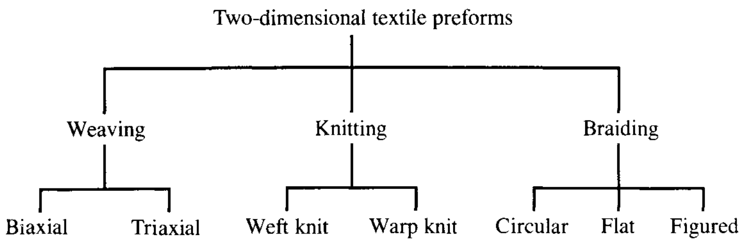

Fig. 6.3. Examples of woven fabric patterns: (a) plain weave ($n_g = 2$); (b) twill weave ($n_g = 3$); (c) four-harness satin ($n_g = 4$); (d) eight-harness satin ($n_g = 8$). (After Ishikawa and Chou 1982a.)

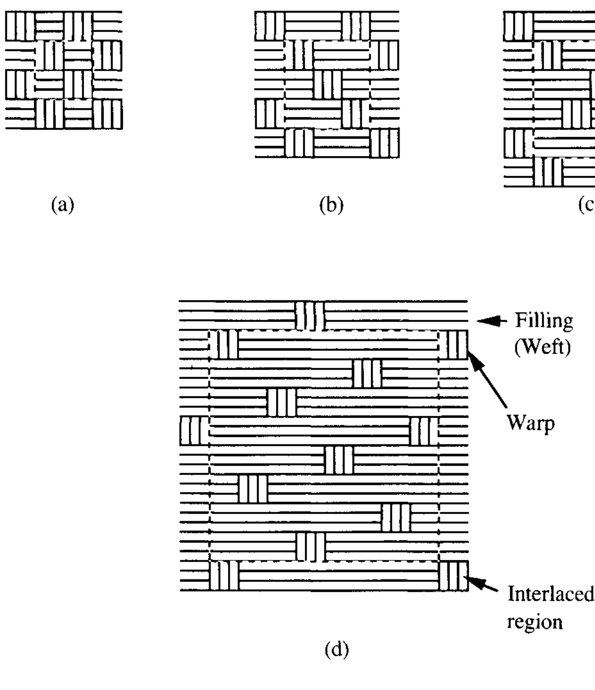

gitudinal yarns are known as the *warp*, and the widthwise yarns are known as the *filling* or *weft*. The individual yarns in the warp and filling directions are also called an *end* and a *pick*, respectively. Figure 6.3 shows examples of orthogonal woven fabrics. According to Lord and Mohamed (1982) and Schwartz, Rhodes and Mohamed (1982), the manufacture of woven fabrics based upon high speed power looms requires four operations or primary motions: (1) shedding, (2) filling insertion, (3) beat-up, and (4) warp and fabric control. Following Lord and Mohamed, and Schwartz, Rhodes and Mohamed, a brief introduction is given for these four motions.

Shedding involves the movement of the warp yarns to provide a path for the insertion of the weft yarn. One of the techniques of shedding uses heddle wires which are grouped into several frames, known as *harnesses* or *shafts* (Fig. 6.4). Each harness is operated by a separate cam; the purpose of the cam is to lift or lower the harness. As a result of the movement of the harness, the shed is formed. A cam loom is generally limited to designs repeating on six or fewer picks (Schwartz, Rhodes and Mohamed 1982). Besides the cam system, traditional fabrics are often woven on a dobby head loom. A commercially available dobby mechanism uses a maximum of about 24 harnesses, and thus allows the control of interlacing 24 different groups of warp yarns. The Jacquard head provides control

Fig. 6.4. Shedding in fabric weaving. (After Lord and Mohamed 1982.)

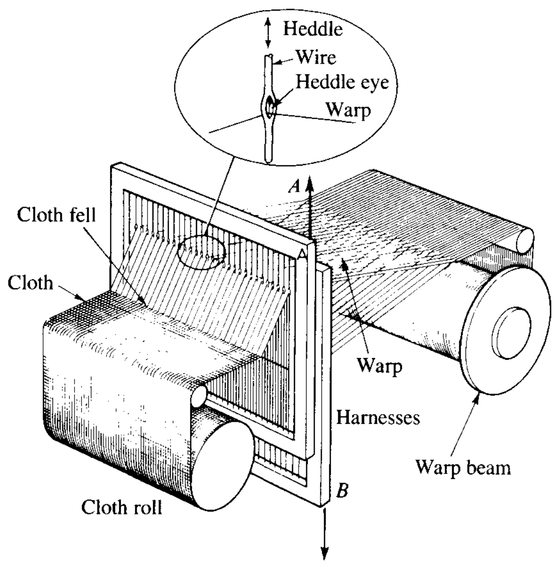

of every individual yarn across the width of the fabric, and it does not have the limitation of the dobby loom. Thus, the yarn interlacing possibilities are greatly enhanced and they are only limited by the number of warp yarns used.

The number of harness frames required for the shedding operation depends on the type of weave. Two harnesses are used for weaving plain fabrics (Fig. 6.3a), and their relative motion is carried out in two weaving cycles. In one cycle, the front harness is in the top position and the back harness is in the bottom position. In the next cycle, the harnesses change positions, and the sequence is repeated. Obviously when the two sheets of warp yarns are at the same level, the shed is closed (Schwartz, Rhodes and Mohamed 1982).

Filling insertion, as the term implies, involves the passing of a filling yarn through the open shed. Figure 6.5 shows schematically the conventional way of filling insertion by a shuttle. In order for the filling insertion motion to take place, the shed has to be sufficiently open and remain open for an adequate period of time. Consequently, the speed of the weaving process is dominated by the speed at which the shuttle travels through the shed. The transit time of the shuttle involves its acceleration and deceleration. Furthermore, it is desirable to remove the filling supply package from the filling carrier so the carrier could be made smaller and the yarn movement in the shedding is reduced. All these considerations provide the impetus for using shuttless looms.

Fig. 6.5. Filling yarn insertion in fabric weaving. (After Lord and Mohamed 1982.)

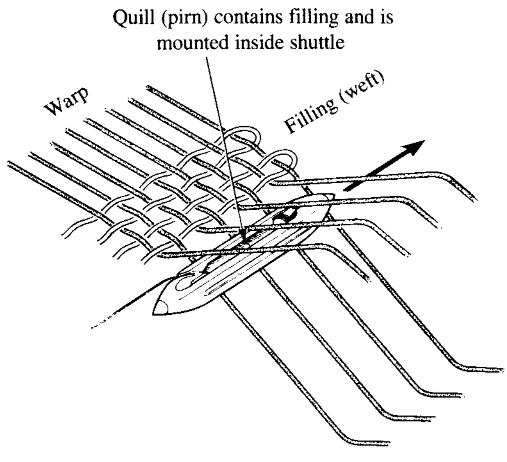

The commonly used shuttless systems include rapiers, gripper projectiles, air jets, and water jets. A rapier is a device made of metal or a composite material with an attachment on the end to carry the filling yarn through the shed. For the case of a single rigid rapier, its length should be at least equal to the loom width. In order to improve the loom speed, double rigid rapiers have been used. These consist of a 'giver', which picks up the filling yarn and carries it to the center of the shed, where the filling yarn is transferred to a 'taker' for transporting the yarn to the other end of the shed. The reduction in carrier traveling time thus doubles the number of picks that can be inserted per unit time. The gripper loom uses a small projectile to transport the filling yarn. It is feasible to use many projectiles which may be initiated from both ends or one end of the loom. In the case of fluid jet looms, the filling yarn is carried by a high pressure air or water jet.

Finally, the purpose of beat-up is for incorporating the filling yarn into the body of the fabric after the filling is inserted. This is accomplished by the use of a wire grate called a *reed*, through which the warp yarns are threaded. The reed is first moved backward to allow the insertion of the filling yarn. When the insertion is finished, the reed moves forward and drives the filling yarn into the fabric. For a continuous operation of the weaving process, it is also necessary to supply the warp yarns continuously, and to remove the fabric from the loom. It should be noted that the repeated actions of shedding and beating induce cyclic tension variations in the yarns (Schwartz, Rhodes and Mohamed 1982). The control of warp and filling yarn tension is essential in the weaving process.

Orthogonal woven fabrics exhibit good dimensional stability in the warp and weft directions. Woven fabrics offer the highest yarn packing density in relation to fabric thickness. The pure and hybrid woven fabrics used in composites are mostly in the forms of plain, basket, twill and satin weaves. Wovens are available in tubular and flat forms.

Woven fabrics provide more balanced properties in the fabric plane than unidirectional laminae; the bidirectional reforcement in a single layer of a fabric gives rise to enhanced impact resistance. The ease of handling and low fabrication cost have made fabrics attractive for structural applications. On the other hand, the limited conformability, poor in-plane shear resistance, and reduced yarn-to-fabric tensile translation efficiency due to yarn crimp are some of the disadvantages of woven fabrics.

Triaxial woven fabrics, made from three sets of yarns which interlace at 60° angles, provide higher isotropy and in-plane shear rigidity than orthogonal wovens. However, no woven fabric construction provides sufficient extensibility for deep-draw molding (Scardino 1989).

6.2.2 *Knits*

A knitted structure is characterized by its interlacing loops. Two basic types of knits can be defined according to the general direction of travel of a looped thread in the fabric (Thomas 1971). In weft knitting, the thread runs widthwise, and the loops are formed by a single weft thread (Fig. 6.6a). The loops in a horizontal

Fig. 6.6. Knitted fabrics: (a) weft knit structure; (b) warp knit structure. (After Thomas 1971.) (c) Knitted fabric with weft and warp laid-ins. (After Wray and Vitols 1982.)

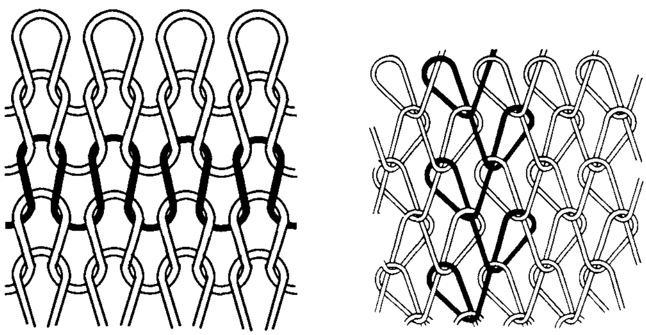

(a) (b)

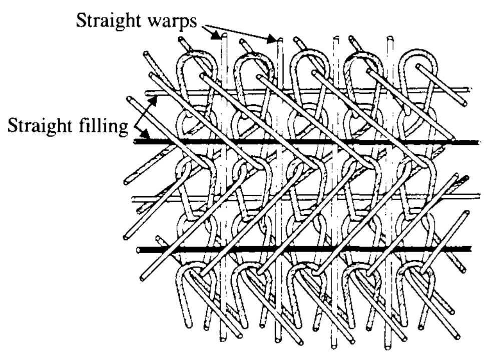

(c)

row are built up one loop at a time. In practice, many weft threads are used simultaneously in weft knitting. In warp knitting, the orientation of a looped thread is warpwise, and all the loops making up a single horizontal row are formed simultaneously (Fig. 6.6b).

The principal mechanical elements used in knitting are needles. According to Schwartz, Rhodes and Mohamed (1982), there are three major needle types: the latch needle, the bearded needle and the compound needle. The latch needle has been used most often and it contains a latch which can be closed in the knitting process.

The loops in knitted fabrics are formed essentially on a very similar principle. Following Thomas (1971), the looping process is demonstrated for a single latch needle by the consecutive steps shown in Fig. 6.7. Consider the needle which has at its stem a loop already formed during the course of the knitting process (Fig. 6.7a). A thread is then placed under the hook of the needle. The loop is restrained in its position whereas the needle is allowed to move through it. As the needle moves downward, the existing loop will push the latch and close the hook (Fig. 6.7c). When the top of the hook reaches the level of the existing loop (Fig. 6.7d), this loop is pulled out of the way by the yarn tension. Then as the needle moves upward again, the thread in the hook opens up the latch, and it becomes the next 'existing' loop. More loops are generated as the process repeats. Depending on the type of knitting machine, a variety of needle configurations and looping cycles is available. A detailed discussion of the knitting processes and knit fabrics has been given by Schwartz, Rhodes and Mohamed (1982).

Simple weft and warp knits can provide extensibility in all

Fig. 6.7. The latch needle cycle in fabric knitting. (After Thomas 1971.)

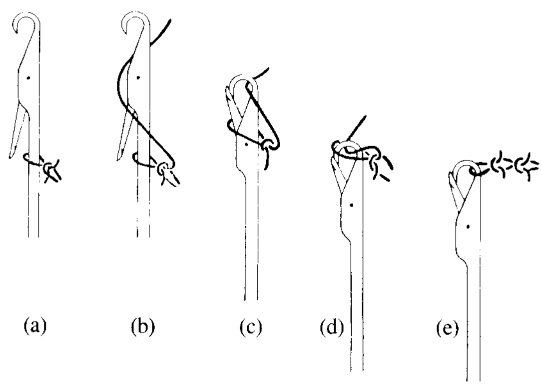

directions and are thus suitable for deep-draw molding techniques. Directional stability can be established by adding laid-in (non-knitting) yarns in the desired directions. According to Scardino, weft inserted warp knits offer flexibility in performance, from complete dimensional stability to engineered directional elongation. Furthermore, weft inserted warp knits with laid-in warp systems offer high yarn-to-fabric translation efficiencies and greater in-plane shear resistance than comparable wovens. An example of a knitted fabric with weft and warp laid-ins is shown in Fig. 6.6(c).

6.2.3 *Braids*

Braided fabrics are constructed from intertwined yarns. In order to understand the characteristics of braided preforms, it is useful to review the basic mechanisms involved in maypole braiders. The paths traced by the carriers of a maypole braider are similar to those of the dancers around the maypole.

Douglass (1964) has explained the operation of some common types of maypole braiders. A simple slide plate machine consists of a deck, a driving mechanism and a superstructure with the take up facility and the braiding guide. The deck has two metal plates. Serpent-like tracks are cut in the upper plate. Between the base plate and the track plate is a train of gears. Each horngear has a circular flanged top which is slotted to engage the bottom driving lugs of the spool carriers. Furthermore, the horngears are so arranged (Fig. 6.8) that the slots in the top flanges of two neighboring horngears will meet at the intersection of the tracks.

Fig. 6.8. Horngears and tracking in a tubular braider. (After Douglass 1964.)

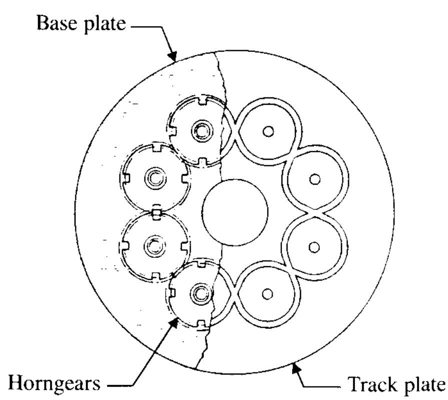

Consider a carrier with its lug engaged in one of the horngear slots and moving in the track; the contour of the track enables the carrier lug to be transferred from one horngear to the next at the intersection. Consequently, this process can be repeated and each carrier can follow a chain of interconnected figure eights in a continuous manner.

According to Douglass (1964), some common types of maypole braiders are the 'Soutache' braider, circular (tubular) braiders and flat braiders. The machine used for Soutache braiding is the simplest of all the braiders, consisting of two horngears which are slotted to take 3, 5, 7, 9, 11, 13 or 17 carriers. Figure 6.9 shows a three-carrier soutache set-up for demonstrating the mechanism of braiding. Circular braiding machines, on the other hand, have an even number of carriers, starting with eight and increasing by steps of four.

Braiders for flat products are characterized by the tracking system, which does not completely encircle the braiding center (Fig. 6.10). The two horngears at the ends of the track have an uneven number of hornslots. Unlike the circular machines, a yarn carrier in this case reverses its path at the terminal gears and as a result flat braids can be accomplished.

The geometric configurations of some two-dimensional braids are given in Fig. 6.11. Figure 6.11(a) shows the braid with a 2/2 intersection repeating pattern, and it is known as a regular, plain or standard braid. Figure 6.11(b) gives a diamond or basket braid

Fig. 6.9. Horngears for a three-carrier 'soutache' braider. (After Douglass 1964.)

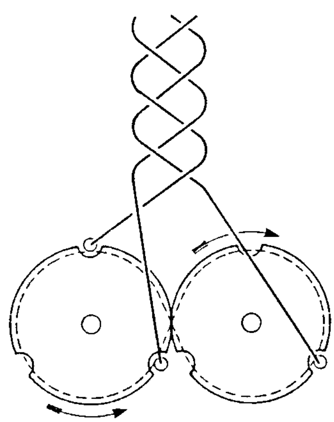

which is characterized by a 1/1 intersection repeating pattern. Figure 6.11(c) shows a regular braid with warp in-laids and it can be made by either a circular or flat braider. There are certain significant similarities and differences between woven and braided fabrics. Both fabrics utilize two sets of yarns; these are the warp and weft yarns in weaving and the yarns moving in clockwise and counter-clockwise directions in circular braiding. As far as interlacing patterns are concerned, they are unlimited in weaving and very limited in braiding (normally 1/1, 2/2 and 3/3). The angle of

Fig. 6.10. Horngears and tracking in a flat braider. (After Douglass 1964.)

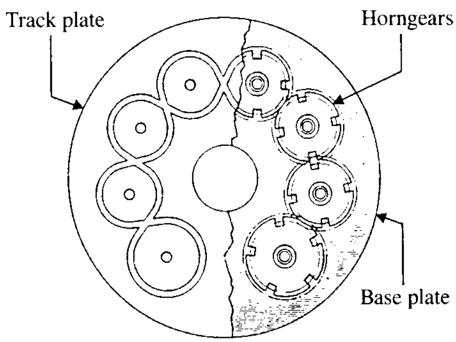

Fig. 6.11. Geometric configurations of (a) flat braid, (b) diamond or basket braid and (c) flat braid with warp in-laids. (After Du, private communication, 1990.)

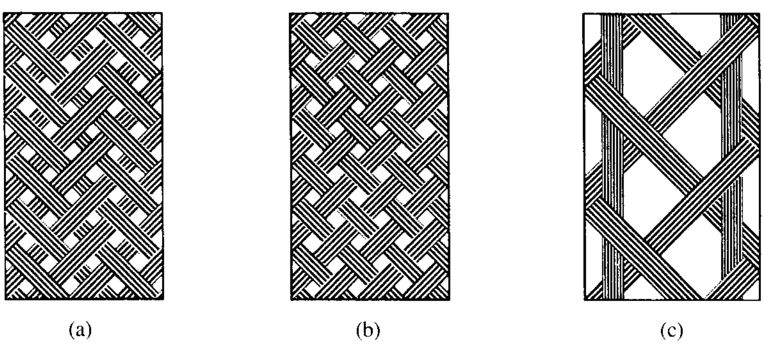

interlacing between the two sets of yarns is 90° in orthogonal woven fabrics and less than 90° in braided fabrics.

The braiding technique is highly versatile and a great variety of geometric patterns can be produced. This is demonstrated by the figured (fancy) braids which have more complex cross-sections (for example, I and T sections) than the traditional braids, or variable cross-section shapes along the axial direction. Figure 6.12 shows a flat-cord-flat fabric, and the tracking system employed for producing such a fabric (Yokoyama *et al.* 1989). The figured braids are categorized as two-dimensional fabrics for the reasons stated earlier. These fabrics could be considered as three-dimensional

Fig. 6.12. (a) A figured braid of flat-cord-flat construction; (b) configuration of the tracking system. (After Yokoyama *et al.* 1989.) Parts *A* and *B* are fabricated by flat braiding, and part *C* is fabricated by a tubular braiding mechanism. The spindles indicated by the open circles move on section *C* of the track and spindles represented by solid circles move through all sections of the track in the sequence (*A*)–(*C*)–(*B*)–(*C*)–(*A*).

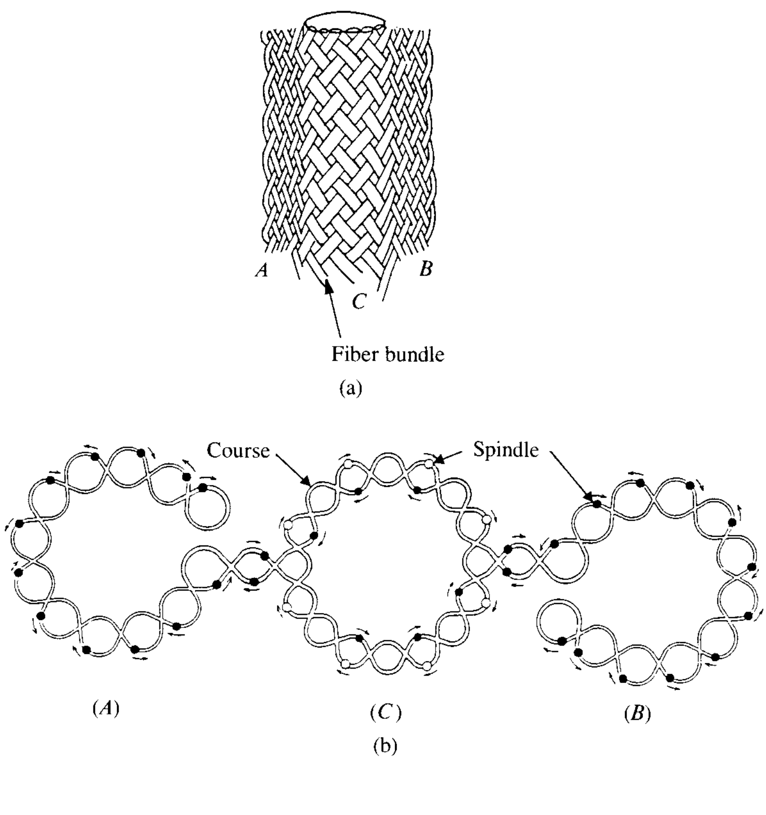

Table 6.1. *Directional behavior of two-dimensional preforms in unjammed configuration*

After Scardino (1989).

Preform construction	Directional stability			Directional conformability			Substantial directional extensibility			Substantial in-plane she resistance	
	MD	CD	BD	MD	CD	BD	MD	CD	BD	MD	CD
Woven											
Biaxial	×	×				×					
Triaxial		×	×	×						×	×
Knitted											
Weft				×	×	×	×	×	×		
Warp				×	×	×	×	×	×		
Braided											
Circular (tubular)			×	×	×					×	×
Flat			×	×	×					×	×

MD = machine direction; CD = crosswise direction; BD = bias direction.

and 90° directions. Yarn jamming in a fabric c
in two ways. First, for a fabric without laid-
n of a tensile force along the 0° or 90° direction w
until it is jammed and no further movement of
. Second, yarn jamming could occur during fa
lition is characterized by the situation that
actor = 1, i.e. there is no void space in between
. Thus, the fabric shape cannot be deformed un
oncept concerning yarn jamming is useful when
ormability and large deformation of a fabric. Th
important when one is concerned about, for inst
fiber volume fraction in a composite, and the
rming process. Chapter 7 provides examples
n the fabrication of three-dimensionally braided
r limitations in machine-made braids at the pre
ted width, diameter, thickness and shape selecti
are also non-woven fabrics which are essentia
composed of randomly oriented fiber segment
There is a lack of geometrically defined arrang
ns as compared to wovens, knits and braids.
of fiber bonding in non-wovens are: sticking fiber
mats, entangling the fibers to give frictional in
through the non-woven web with a textile y
bonding. Hearle (1989) has given in-depth trea
nics of non-woven fabrics.

o (1989) has examined the behavior of vario
f ... te
swise (90°) and bias (±45°) directions. Table

Sections 6.3 to 6.11 are excerpted from the work of Chou and Ishikawa (1989).

6.3 Methodology of analysis

The objective of the analysis in Section 6.3 is to model the thermomechanical behavior of two-dimensional orthogonal woven fabric composites. The fabrics are composed of two sets of mutually orthogonal yarns of either the same material (non-hybrid fabrics) or different materials (hybrid fabrics). Here, the term 'yarns' represents individual filaments, untwisted fiber bundles, twisted fiber bundles or rovings.

An orthogonal woven fabric consists of two sets of interlaced yarns. The length direction of the fabric is known as the *warp*, and the width direction is referred to as the *filling* or *weft*. The various types of fabric can be identified by the pattern of repeat of the interlaced regions, as shown in Fig. 6.3. Two basic geometrical parameters can be defined to characterize a fabric: n_{fg} denotes that a warp yarn is interlaced with every n_{fg}th filling yarn and n_{wg} denotes that a filling yarn is interlaced with every n_{wg}th warp yarn. The present treatment is confined to the case of $n_{wg} = n_{fg} = n_g$ for both hybrid and non-hybrid fabrics. Fabrics with $n_g \gtrsim 4$ are known as satin weaves. As defined by their n_g values, the fabrics in Fig. 6.3 are termed plain weave ($n_g = 2$), twill weave ($n_g = 3$), four-harness satin ($n_g = 4$), and eight-harness satin ($n_g = 8$). The regions in Fig. 6.3 enclosed by the dotted lines define the 'unit cells' or the basic repeating regions for the different weaving patterns. It is also noted that the top sides of the fabrics in Fig. 6.3 are dominated by the filling yarns, whereas the reverse sides are dominated by the warp yarns.

The theoretical basis of the present analysis is the classical laminated plate theory, which is given in Chapter 2. Only the key equations are recapitulated in the following for ease of reference. Under the assumptions of the Kirchhoff hypothesis, the constitutive equations are expressed in the condensed form as

$$\left\{\begin{array}{c} N \\ \hline M \end{array}\right\} = \left[\begin{array}{c|c} A & B \\ \hline B & D \end{array}\right] \left\{\begin{array}{c} \varepsilon^{\mathrm{o}} \\ \hline \kappa \end{array}\right\} \tag{6.1}$$

Here, N and M are membrane stress resultants and moment resultants, respectively; ε^{o} and κ are the strain and curvature of the laminate geometric mid-plane, respectively. The components of the stiffness matrices A, B and D are evaluated as follows:

$$(A_{ij}, B_{ij}, D_{ij}) = \sum_{k=1}^{n} \int_{h_{k-1}}^{h_k} (1, z, z^2)(\bar{Q}_{ij})_k \, \mathrm{d}z \qquad (i, j = 1, 2, 6) \tag{6.2}$$

where the reduced stiffness constants $\bar{Q}_{ij}$ corresponding to the lamina defined by h_k and h_{k-1} in the thickness direction are used in the calculations. The subscripts 1, 2 and 6 in Eq. (6.2) indicate, in the xyz coordinate system, the x direction, the y direction, and the x–y plane, respectively. More explicitly, Eq. (6.2) can be written as

$$\begin{aligned} A_{ij} &= \sum_{k=1}^{n} (\bar{Q}_{ij})_k (h_k - h_{k-1}) \\ B_{ij} &= \tfrac{1}{2} \sum_{k=1}^{n} (\bar{Q}_{ij})_k (h_k^2 - h_{k-1}^2) \\ D_{ij} &= \tfrac{1}{3} \sum_{k=1}^{n} (\bar{Q}_{ij})_k (h_k^3 - h_{k-1}^3) \end{aligned} \tag{6.3}$$

The inverted form of Eq. (6.1) is given by

$$\left\{ \begin{array}{c} \varepsilon^{\mathrm{o}} \\ \hline \kappa \end{array} \right\} = \left[\begin{array}{c|c} A' & B' \\ \hline B' & D' \end{array} \right] \left\{ \begin{array}{c} N \\ \hline M \end{array} \right\} \tag{6.4}$$

When the effect of temperature change is taken into account, the constitutive relation of Eq. (6.1) should be written as

$$\left\{ \begin{array}{c} N \\ \hline M \end{array} \right\} = \left[\begin{array}{c|c} A & B \\ \hline B & D \end{array} \right] \left\{ \begin{array}{c} \varepsilon^{\mathrm{o}} \\ \hline \kappa \end{array} \right\} - \Delta T \left\{ \begin{array}{c} \tilde{A} \\ \hline \tilde{B} \end{array} \right\} \tag{6.5}$$

where

$$\begin{Bmatrix} \tilde{A}_x \\ \tilde{A}_y \\ \tilde{A}_{xy} \end{Bmatrix} = \sum_{k=1}^{n} \int_{h_{k-1}}^{h_k} \begin{bmatrix} \bar{Q}_{11} & \bar{Q}_{12} & \bar{Q}_{16} \\ \bar{Q}_{12} & \bar{Q}_{22} & \bar{Q}_{26} \\ \bar{Q}_{16} & \bar{Q}_{26} & \bar{Q}_{66} \end{bmatrix}_k \begin{Bmatrix} \alpha_{xx} \\ \alpha_{yy} \\ \alpha_{xy} \end{Bmatrix}_k \mathrm{d}z \tag{6.6}$$

$$\begin{Bmatrix} \tilde{B}_x \\ \tilde{B}_y \\ \tilde{B}_{xy} \end{Bmatrix} = \sum_{k=1}^{n} \int_{h_{k-1}}^{h_k} \begin{bmatrix} \bar{Q}_{11} & \bar{Q}_{12} & \bar{Q}_{16} \\ \bar{Q}_{12} & \bar{Q}_{22} & \bar{Q}_{26} \\ \bar{Q}_{16} & \bar{Q}_{26} & \bar{Q}_{66} \end{bmatrix}_k \begin{Bmatrix} \alpha_{xx} \\ \alpha_{yy} \\ \alpha_{xy} \end{Bmatrix}_k z \, \mathrm{d}z \tag{6.7}$$

ΔT indicates a small uniform temperature change, and α denotes the thermal expansion coefficients. After inversion, Eq. (6.5) becomes

$$\left\{\frac{\varepsilon^{o}}{\kappa}\right\} = \left[\begin{array}{c|c} A' & B' \\ \hline B' & D' \end{array}\right]\left\{\frac{N}{M}\right\} + \Delta T\left\{\frac{\tilde{A}'}{\tilde{B}'}\right\} \tag{6.8}$$

where

$$\left\{\frac{\tilde{A}'}{\tilde{B}'}\right\} = \left[\begin{array}{c|c} A' & B' \\ \hline B' & D' \end{array}\right]\left\{\frac{\tilde{A}}{\tilde{B}}\right\} \tag{6.9}$$

The constants $\tilde{A}'$ and $\tilde{B}'$ represent, respectively, the in-plane thermal expansion and thermal bending coefficients.

Based upon the iso-stress and iso-strain assumptions, the above constitutive equations can be used to obtain the bounds of the thermoelastic properties. The upper bounds of compliance constants are obtained from the iso-stress assumption; the lower bounds of stiffness constants are then obtained by inverting the compliance constant matrix. Similarly, the upper bounds of stiffness constants are derived from the iso-strain assumption; the lower bounds of compliance constants are then obtained by inverting the stiffness constant matrix. Three techniques for modeling the stiffness and strength properties of fabric composites are introduced in Sections 6.4–6.6 based upon the laminated plate analysis. They are known as the 'mosaic model', 'crimp (fiber undulation) model', and 'bridging model'. The prediction of thermal expansion coefficients of fabric composites is given in Section 6.8 based upon these three models. The analytical techniques so developed are also applied to hybrid fabric composites (Sections 6.9 and 6.10). Finally, the thermoelastic behavior of two-dimensional textile structural composites reinforced with triaxial fabrics is presented in Section 6.11. The following discussions are based on the work of Ishikawa and Chou (1982a–c, 1983a–d), Ishikawa (1981), Chou (1985, 1986, 1989a&b), Yang and Chou (1986, 1987) and Byun and Chou (1989).

6.4 Mosaic model

The basis of idealization of the 'mosaic model' can be seen from Fig. 6.13. Figure 6.13(a) is a cross-sectional view of an eight-harness satin. The consolidation of the fabric with a matrix material is depicted in Fig. 6.13(b), which can be simplified as the mosaic model of Fig. 6.13(c). The key simplification of the mosaic model is the omission of the fiber continuity and crimp (undulation) that exist in an actual fabric.

In general, a fabric composite idealized by the mosaic model can be regarded as an assemblage of pieces of asymmetric cross-ply laminates. Figure 6.14(a) shows the mosaic model of a unit cell for an eight-harness satin composite. The elastic stiffness constants of a cross-ply laminate (Fig. 6.14b) can be derived on the basis of Eqs. (6.3). Assuming that fibers are aligned along the x direction, the stiffness constants, Q_{ij}, of a unidirectional lamina, which has

Fig. 6.13. Idealization of the mosaic model. (a) Cross-sectional view of a woven fabric before resin impregnation; (b) woven fabric composite; (c) idealization of the mosaic model. (After Ishikawa and Chou 1983b.)

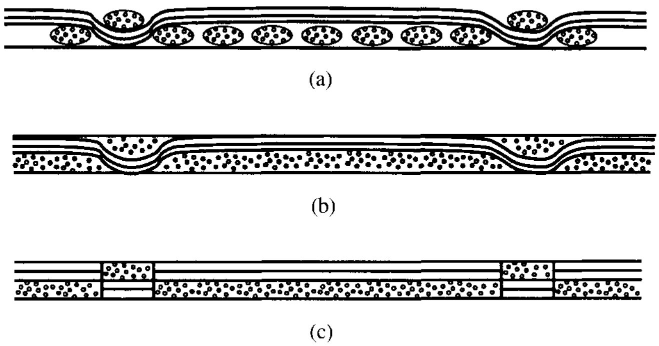

Fig. 6.14. The mosaic model. (a) Repeating region in an eight-harness satin composite; (b) a basic cross-ply laminate; (c) parallel model; (d) series model. (After Ishikawa and Chou 1983b.)

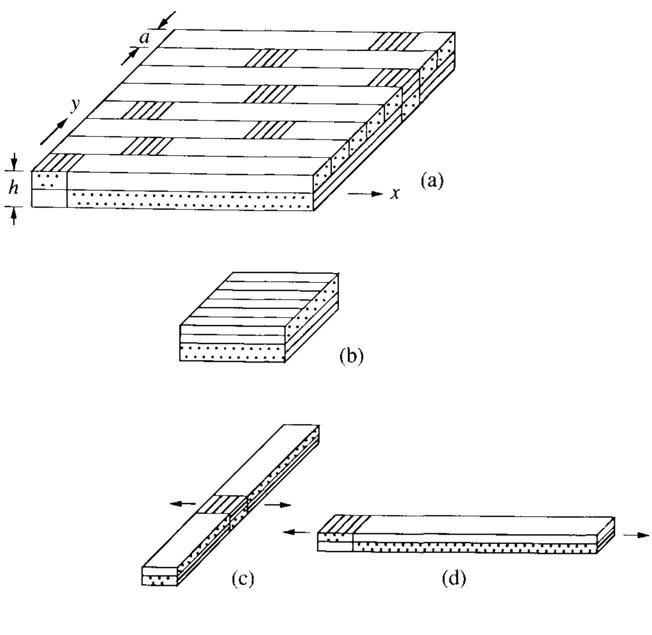

orthotropic symmetry in the x–y plane, are given by

$$Q_{ij} = \begin{bmatrix} E_{11}/D_v & \nu_{12}E_{22}/D_v & 0 \\ \nu_{21}E_{11}/D_v & E_{22}/D_v & 0 \\ 0 & 0 & G_{12} \end{bmatrix} \tag{6.10}$$

where

$$D_v = 1 - \nu_{12}\nu_{21} \tag{6.11}$$

Here, E_{11} and E_{22} are the Young's moduli, G_{12} is the in-plane shear modulus, and ν_{12} denotes the Poisson's ratio relating the transverse strain in the x_2 direction and the applied strain in the x_1 direction. The Q_{ij} constants are symmetrical, i.e. $Q_{ij} = Q_{ji}$ (see Chapter 2).

From Eqs. (6.3) and (6.10), the elastic stiffness constants of the cross-ply laminate shown in Fig. 6.14(b) can be derived. The laminate is composed of two unidirectional laminae of thickness $h/2$. The total laminate thickness is h and the x–y coordinate plane is positioned at the geometrical mid-plane of the laminate. Thus, in Eqs. (6.3), $k = 1$ and 2 define, respectively, the laminae with fibers in the y and x directions. The non-vanishing stiffness constants are

$$\begin{aligned} A_{11} &= A_{22} = (E_{11} + E_{22})h/(2D_v) \\ A_{12} &= \nu_{12}E_{22}h/D_v \\ A_{66} &= G_{12}h \\ B_{11} &= -B_{22} = (E_{11} - E_{22})h^2/(8D_v) \\ D_{11} &= D_{22} = (E_{11} + E_{22})h^3/(24D_v) \\ D_{12} &= \nu_{12}E_{22}h^3/(12D_v) \\ D_{66} &= G_{12}h^3/12 \end{aligned} \tag{6.12}$$

The extension-bending coupling constants B_{11} and B_{22} do not vanish because $E_{11} \neq E_{22}$. Also, it is understood that A_{ij}, B_{ij}, and D_{ij} are symmetrical constants.

Using Eqs. (6.12), Eq. (6.1) can be written in the following explicit form:

$$\begin{aligned} \begin{Bmatrix} N_x \\ N_y \\ N_{xy} \end{Bmatrix} &= \begin{bmatrix} A_{11} & A_{12} & 0 \\ A_{12} & A_{11} & 0 \\ 0 & 0 & A_{66} \end{bmatrix} \begin{Bmatrix} \varepsilon^{o}_{xx} \\ \varepsilon^{o}_{yy} \\ \gamma^{o}_{xy} \end{Bmatrix} + \begin{bmatrix} B_{11} & 0 & 0 \\ 0 & -B_{11} & 0 \\ 0 & 0 & 0 \end{bmatrix} \begin{Bmatrix} \kappa_{xx} \\ \kappa_{yy} \\ \kappa_{xy} \end{Bmatrix} \\ \begin{Bmatrix} M_x \\ M_y \\ M_{xy} \end{Bmatrix} &= \begin{bmatrix} B_{11} & 0 & 0 \\ 0 & -B_{11} & 0 \\ 0 & 0 & 0 \end{bmatrix} \begin{Bmatrix} \varepsilon^{o}_{xx} \\ \varepsilon^{o}_{yy} \\ \gamma^{o}_{xy} \end{Bmatrix} + \begin{bmatrix} D_{11} & D_{12} & 0 \\ D_{12} & D_{11} & 0 \\ 0 & 0 & D_{66} \end{bmatrix} \begin{Bmatrix} \kappa_{xx} \\ \kappa_{yy} \\ \kappa_{xy} \end{Bmatrix} \end{aligned} \tag{6.13}$$

Inverting Eqs. (6.13), the following are obtained:

$$\begin{Bmatrix} \varepsilon_{xx}^{o} \\ \varepsilon_{yy}^{o} \\ \gamma_{xy}^{o} \end{Bmatrix} = \begin{bmatrix} A'_{11} & A'_{12} & 0 \\ A'_{12} & A'_{11} & 0 \\ 0 & 0 & A'_{66} \end{bmatrix} \begin{Bmatrix} N_x \\ N_y \\ N_{xy} \end{Bmatrix} + \begin{bmatrix} B'_{11} & B'_{12} & 0 \\ -B'_{12} & -B'_{11} & 0 \\ 0 & 0 & 0 \end{bmatrix} \begin{Bmatrix} M_x \\ M_y \\ M_{xy} \end{Bmatrix}$$

$$\begin{Bmatrix} \kappa_{xx} \\ \kappa_{yy} \\ \kappa_{xy} \end{Bmatrix} = \begin{bmatrix} B'_{11} & -B'_{12} & 0 \\ -B'_{12} & -B'_{11} & 0 \\ 0 & 0 & 0 \end{bmatrix} \begin{Bmatrix} N_x \\ N_y \\ N_{xy} \end{Bmatrix} + \begin{bmatrix} D'_{11} & D'_{12} & 0 \\ D'_{12} & D'_{11} & 0 \\ 0 & 0 & D'_{66} \end{bmatrix} \begin{Bmatrix} M_x \\ M_y \\ M_{xy} \end{Bmatrix} \tag{6.14}$$

In the bound approach, the two-dimensional extent of the fabric composite plate is simplified by considering two one-dimensional models where the pieces of cross-ply laminates are either in parallel or in series as shown in Figs. 6.14(c) and (d). In the parallel model, a uniform state of strain, ε^{o}, and curvature, κ, in the laminate midplane is assumed as a first approximation. For the one-dimensional repeating region of length $n_g a$, where a denotes the yarn width, an average membrane stress, $\bar{N}_x$, is defined as

$$\begin{aligned} \bar{N}_x &= \frac{1}{n_g a} \int_0^{n_g a} N_x \, dy \\ &= \frac{1}{n_g a} \left[\int_0^{a} (A_{11}\varepsilon_{xx}^{o} + A_{12}\varepsilon_{yy}^{o} + B_{11}\kappa_{xx}) \, dy \right. \\ &\quad \left. + \int_a^{n_g a} (A_{11}\varepsilon_{xx}^{o} + A_{12}\varepsilon_{yy}^{o} + B_{11}\kappa_{xx}) \, dy \right] \\ &= (A_{11}\varepsilon_{xx}^{o} + A_{12}\varepsilon_{yy}^{o}) + \frac{1}{n_g a}[aB_{11}^{T} + (n_g a - a)B_{11}^{L}]\kappa_{xx} \\ &= A_{11}\varepsilon_{xx}^{o} + A_{12}\varepsilon_{yy}^{o} + \left(1 - \frac{2}{n_g}\right) B_{11}^{L}\kappa_{xx} \end{aligned} \tag{6.15}$$

The factor $(1 - 2/n_g)$ appears because the terms B_{11} for the interlaced region (B_{11}^{T}) and non-interlaced region (B_{11}^{L}) have opposite signs, namely, $B_{11}^{T} = -B_{11}^{L}$. It is noted that B_{11}^{L} is derived for a cross-ply with the same configuration as in Fig. 6.14(b), where the upper surface ($z > 0$) shows fibers in the x direction. B_{11}^{T} is for a cross-ply obtained by exchanging the positions of the two laminae in Fig. 6.14(b). Other average stress resultants can be written similar to Eq. (6.15) for uniform mid-plane strain, ε^{o}, and curvature, κ. The moment resultant, $\bar{M}_x$, for example, is

$$\begin{aligned}\bar{M}_x &= \frac{1}{n_{\mathrm{g}}a}\int_0^{n_{\mathrm{g}}a} M_x \,\mathrm{d}y \\ &= D_{11}\kappa_{xx} + D_{12}\kappa_{yy} + \left(1 - \frac{2}{n_{\mathrm{g}}}\right)B_{11}^{\mathrm{L}}\varepsilon_{xx}^{\mathrm{o}}\end{aligned} \tag{6.16}$$

Let $\bar{A}_{ij}$, $\bar{B}_{ij}$, and $\bar{D}_{ij}$ be the stiffness constant matrices relating the average stress resultant $\bar{N}$ and moment resultant $\bar{M}$ with ε^{o} and κ. Then

$$\begin{aligned}\bar{A}_{ij} &= A_{ij} \\ \bar{B}_{ij} &= \left(1 - \frac{2}{n_{\mathrm{g}}}\right)B_{ij}^{\mathrm{L}} \\ \bar{D}_{ij} &= D_{ij}\end{aligned} \tag{6.17}$$

These components provide upper bounds for the stiffness constants of the fabric composite based upon the one-dimensional model. If these stiffness constants are inverted, lower bounds of the elastic compliance constants can be obtained. All the elastic stiffness constants A, B and D are computed using the basic laminate where the top layer is composed of the filling yarn (Fig. 6.14b).

In the series model, the disturbance of stress and strain near the interface of the interlaced region is neglected. Let the model be subjected to a uniform in-plane force, N_x, in the longitudinal direction. The assumption of constant stress leads to the definition of an average curvature. For instance, the average curvature, $\bar{\kappa}_{xx}$, along the x direction is

$$\begin{aligned}\bar{\kappa}_{xx} &= \frac{1}{n_{\mathrm{g}}a}\int_0^{n_{\mathrm{g}}a} \kappa_{xx}\,\mathrm{d}x \\ &= \frac{1}{n_{\mathrm{g}}a}\left[\int_0^a B_{11}'N_x\,\mathrm{d}x + \int_a^{n_{\mathrm{g}}a} B_{11}'N_x\,\mathrm{d}x\right] \\ &= \frac{1}{n_{\mathrm{g}}a}[aB_{11}'^{\mathrm{T}} + a(n_{\mathrm{g}}-1)B_{11}'^{\mathrm{L}}]N_{\mathrm{x}} \\ &= \left(1 - \frac{2}{n_{\mathrm{g}}}\right)B_{11}'^{\mathrm{L}}N_x\end{aligned} \tag{6.18}$$

It is also understood that the terms B'_{11} for the interlaced region (B'^{T}_{11}) and non-interlaced region (B'^{L}_{11}) are equal and opposite in sign. Other average curvature and mid-plane strain expressions can be written similar to Eq. (6.18) for uniformly applied N and M. Let $\bar{A}'_{ij}$, $\bar{B}'_{ij}$, and $\bar{D}'_{ij}$ be the compliance constant matrices relating the average mid-plane strain, $\bar{\varepsilon}^{\mathrm{o}}$, and curvature, $\bar{\kappa}$, with the stress resultant, N, and moment resultant, M. Thus

$$\begin{aligned} \bar{A}'_{ij} &= A'_{ij} \\ \bar{B}'_{ij} &= \left(1 - \frac{2}{n_{\mathrm{g}}}\right) B'^{\mathrm{L}}_{ij} \\ \bar{D}'_{ij} &= D'_{ij} \end{aligned} \tag{6.19}$$

Equations (6.19) give the upper bounds for the composite compliance constants and, after inversion, the lower bounds for the stiffness constants.

In summary, both upper and lower bounds for the elastic stiffness and compliance constants can be obtained from the mosaic model. Numerical results demonstrating the relationship between these bounds and $1/n_{\mathrm{g}}$ are shown in Fig. 6.15 for $\bar{A}_{11}$ and $\bar{A}'_{11}$ and in Fig. 6.16 for $\bar{B}'_{11}$. The material properties of a carbon/epoxy composite given in Table 6.2, with fiber volume fraction in the impregnated yarn of 60%, are adopted in the calculations. Bidirectional fiber

Fig. 6.15. Variations of $\bar{A}'_{11}$ and $\bar{A}_{11}$ with $1/n_{\mathrm{g}}$. (After Ishikawa and Chou 1983b.)

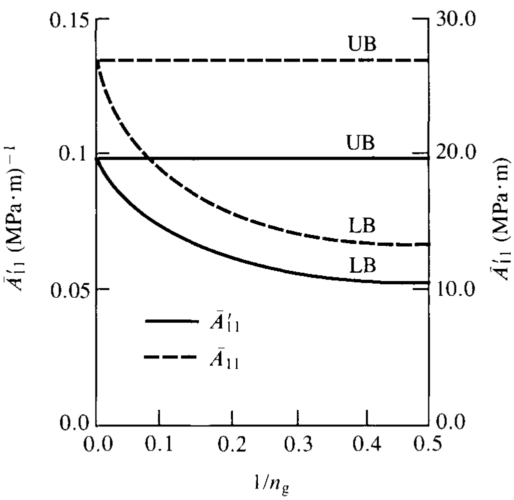

composites are represented by the limiting case of $1/n_g \to 0$ ($n_g \to \infty$) and the upper and lower bounds of the elastic constants coincide with each other. Plain weaves are represented by the case of $1/n_g = 0.5$. The coupling effects for plain weave composites vanish, as can be seen from Eqs. (6.17) and (6.19), and both the upper and lower bounds of $\bar{B}'_{ij}$ ($\bar{B}_{ij}$) are identical, i.e. zero. However, the bounds of $\bar{A}_{ij}$ ($\bar{A}'_{ij}$) do not coincide for plain weave composites.

6.5 Crimp (fiber undulation) model

The crimp model is developed in order to consider the continuity and undulations of fibers in a fabric composite. Although the formulation of the problem developed in the following is valid for all n_g values, the crimp model is particularly suited for fabrics with low n_g values. The crimp model also provides the basis of analysis for the bridging model (Section 6.6).

Figure 6.17 depicts the geometry of the model where the undulation shape is defined by the parameters $h_1(x)$, $h_2(x)$, and a_u. The parameters $a_o = (a - a_u)/2$ and $a_2 = (a + a_u)/2$ are automatically determined by specifying a_u, which is geometrically arbitrary in the range from 0 to a. Because a pure matrix region appears in

Fig. 6.16. Variations of the average coupling compliance with $1/n_g$. (After Ishikawa and Chou 1983b.)

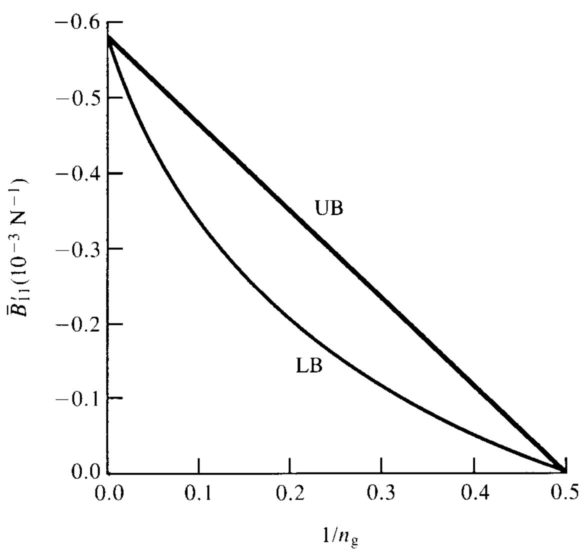

Material properties of unidirectional laminae

	Fiber volume fraction in impregnated yarns	E_{11}(GPa)	E_{22}(GPa)	G_{12}(GPa)	ν_{12}	ε_2^b	Thickness (mm)	$\alpha_1(10^{-7}/°C)$
xy[1]	60%	113	8.82	4.46	0.3	—	0.4	—
	65%	132	9.31	4.61	0.28	—	0.4	−25.0
ster[2]	60%	47.5	15.9	6.23	0.27	0.38%	0.4	—
nide[3]	50%	41.2	15.7	5.59	0.3	0.5%	0.244	—
xy[4]	65%	85.3	5.5	2.54	0.4	—	—	−11.0

, Koyama and Kobayashi (1977), Ishikawa (1981), Ishikawa and Chou (1983b). (2) Kimpara, Hamamoto ar
shikawa and Chou (1982b). (4) Chou and Ishikawa (1989).

the model, the 'overall' fiber volume fraction, V_f, can be different from that in the yarn region.

To simulate the actual configuration, the following form of crimp is assumed for the filling:

$$h_1(x) = \begin{cases} 0 & (0 \le x \le a_o) \\ \left[1 + \sin\left\{\left(x - \frac{a}{2}\right)\frac{\pi}{a_u}\right\}\right] h_t/4 & (a_o \le x \le a_2) \\ h_t/2 & (a_2 \le x \le n_g a/2) \end{cases} \tag{6.20}$$

The sectional shape of the warp yarn is expressed by

$$h_2(x) = \begin{cases} h_t/2 & (0 \le x \le a_o) \\ \left[1 - \sin\left\{\left(x - \frac{a}{2}\right)\frac{\pi}{a_u}\right\}\right] h_t/4 & (a_o \le x \le a/2) \\ -\left[1 + \sin\left\{\left(x - \frac{a}{2}\right)\frac{\pi}{a_u}\right\}\right] h_t/4 & (a/2 \le x \le a_2) \\ -h_t/2 & (a_2 \le x \le n_g a/2) \end{cases} \tag{6.21}$$

It is assumed that the laminated plate theory is applicable to each infinitesimal piece of the model along the x axis. Thus, A_{ij}, B_{ij}, and

Fig. 6.17. Fiber crimp model. (After Ishikawa and Chou 1982b.)

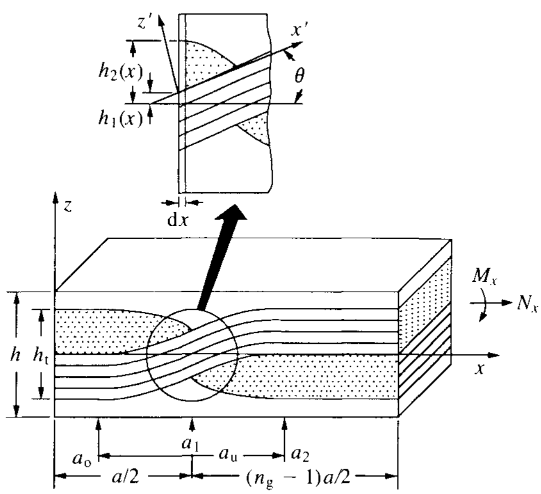

D_{ij} are expressed as functions of x $(0 \leq x \leq a/2)$ by

$$\begin{aligned}
A_{ij}(x) &= \int_{-h/2}^{h_1(x)-h_t/2} Q_{ij}^{\mathrm{M}}\,\mathrm{d}z + \int_{h_1(x)-h_t/2}^{h_1(x)} Q_{ij}^{\mathrm{F}}(\theta)\,\mathrm{d}z \\
&\quad + \int_{h_1(x)}^{h_2(x)} Q_{ij}^{\mathrm{W}}\,\mathrm{d}z + \int_{h_2(x)}^{h/2} Q_{ij}^{\mathrm{M}}\,\mathrm{d}z \\
&= Q_{ij}^{\mathrm{M}}[h_1(x) - h_2(x) + h - h_t/2] \\
&\quad + Q_{ij}^{\mathrm{F}}(\theta)h_t/2 + Q_{ij}^{\mathrm{W}}[h_2(x) - h_1(x)] \\
B_{ij}(x) &= \tfrac{1}{2}Q_{ij}^{\mathrm{F}}(\theta)[h_1(x) - h_t/4]h_t + \tfrac{1}{4}Q_{ij}^{\mathrm{W}}[h_2(x) - h_1(x)]h_t \\
D_{ij}(x) &= \tfrac{1}{3}Q_{ij}^{\mathrm{M}}\{[h_1(x) - h_t/2]^3 - h_2^3(x) + h^3/4\} \\
&\quad + \tfrac{1}{3}Q_{ij}^{\mathrm{F}}(\theta)[h_t^3/8 - 3h_t^2 h_1(x)/4 \\
&\quad + 3h_t h_1^2(x)/2] + \tfrac{1}{3}Q_{ij}^{\mathrm{W}}[h_2^3(x) - h_1^3(x)]
\end{aligned} \tag{6.22}$$

where superscripts F, W and M signify the filling yarn, warp yarn and matrix, respectively. Similar expressions can be written for $a/2 \leq x \leq n_g a/2$.

The local stiffness of the filling yarn, $Q_{ij}^{\mathrm{F}}(\theta)$, in the above equations is calculated as a function of the local off-axis angle, $\theta(x)$, which is defined as

$$\theta(x) = \arctan\left(\frac{\mathrm{d}h_1(x)}{\mathrm{d}x}\right) \tag{6.23}$$

Consider a filling yarn composed of parallel fibers. The fiber direction is denoted as the 1 direction; the 2 and 3 directions are perpendicular to the fiber and they define the transversely isotropic plane. Then, from the Young's moduli (E_{11}, $E_{22} = E_{33}$), shear moduli ($G_{12} = G_{13}$, G_{23}) and Poisson's ratio (ν_{12}) of the filling yarn, the elastic constants of the filling yarn with respect to the xyz axes in Fig. 6.17 can be defined (Lekhnitskii 1963). Here, the angle between the 1 and x axes is θ:

$$\begin{aligned}
\frac{1}{E_{xx}^{\mathrm{F}}(\theta)} &= \frac{\cos^4\theta}{E_{11}} + \left(\frac{1}{G_{12}} - \frac{2\nu_{21}}{E_{22}}\right)\cos^2\theta\sin^2\theta + \frac{\sin^4\theta}{E_{22}} \\
E_{yy}^{\mathrm{F}}(\theta) &= E_{22} = E_{33} \\
\frac{1}{G_{xy}^{\mathrm{F}}(\theta)} &= \frac{\cos^2\theta}{G_{12}} + \frac{\sin^2\theta}{G_{23}} \\
\nu_{yx}^{\mathrm{F}}(\theta) &= \nu_{21}\cos^2\theta + \nu_{32}\sin^2\theta
\end{aligned} \tag{6.24}$$

It is also understood from the assumption of transverse isotropy of the filling yarn that $\nu_{12} = \nu_{13}$, $E_{11}/\nu_{12} = E_{22}/\nu_{21}$, $\nu_{23} = \nu_{32}$, and $G_{23} = E_{22}/2(1 + \nu_{23})$.

Thus, the local stiffness constants of the undulated portion of the filling yarn, referring to the *xyz* coordinate axes, are given as functions of the fiber orientation angle θ

$$Q_{ij}^{\mathrm{F}}(\theta) = \begin{bmatrix} E_{xx}^{\mathrm{F}}(\theta)/D_\nu & E_{xx}^{\mathrm{F}}(\theta)\nu_{yx}^{\mathrm{F}}(\theta)/D_\nu & 0 \\ E_{xx}^{\mathrm{F}}(\theta)\nu_{yx}^{\mathrm{F}}(\theta)/D_\nu & E_{yy}^{\mathrm{F}}(\theta)/D_\nu & 0 \\ 0 & 0 & G_{xy}^{\mathrm{F}}(\theta) \end{bmatrix} \quad (i,j = 1, 2, 6) \tag{6.25}$$

where

$$D_\nu = 1 - (\nu_{yx}^{\mathrm{F}}(\theta))^2 E_{xx}^{\mathrm{F}}(\theta)/E_{yy}^{\mathrm{F}}(\theta) \tag{6.26}$$

By substituting Eq. (6.25) into Eqs. (6.22), the local plate stiffness constants can be evaluated. The local compliance constants, $A'_{ij}(x)$, $B'_{ij}(x)$, and $D'_{ij}(x)$ are then obtained by inverting the stiffness constants $A_{ij}(x)$, $B_{ij}(x)$, and $D_{ij}(x)$.

Define the average in-plane compliance of the model under a uniformly applied in-plane stress resultant by

$$\bar{A}_{ij}^{\prime\mathrm{C}} = \frac{2}{n_{\mathrm{g}}a}\int_0^{n_{\mathrm{g}}a/2} A'_{ij}(x)\,\mathrm{d}x \tag{6.27}$$

where the superscript C signifies the crimp model. Since $A'_{ij}(x)$ is a constant within the straight yarn portion of Fig. 6.17, Eq. (6.27) can be rewritten as

$$\bar{A}_{ij}^{\prime\mathrm{C}} = \left(1 - \frac{2a_{\mathrm{u}}}{n_{\mathrm{g}}a}\right)A'_{ij} + \frac{2}{n_{\mathrm{g}}a}\int_{a_0}^{a_2} A'_{ij}(x)\,\mathrm{d}x \tag{6.28}$$

where A'_{ij} in the first term on the right-hand side of Eq. (6.28) denotes the compliance of the straight portion of the yarns, namely a cross-ply laminate, and is independent of x. The other average compliance coefficients $\bar{B}_{ij}^{\prime\mathrm{C}}$ and $\bar{D}_{ij}^{\prime\mathrm{C}}$ are obtained in a similar manner.

$$\bar{B}_{ij}^{\prime\mathrm{C}} = \left(1 - \frac{2}{n_{\mathrm{g}}}\right)B'_{ij} + \frac{2}{n_{\mathrm{g}}a}\int_{a_0}^{a_2} B'_{ij}(x)\,\mathrm{d}x \tag{6.29}$$

$$\bar{D}_{ij}^{\prime\mathrm{C}} = \left(1 - \frac{2a_{\mathrm{u}}}{n_{\mathrm{g}}a}\right)D'_{\mathrm{ij}} + \frac{2}{n_{\mathrm{g}}a}\int_{a_0}^{a_2} D'_{ij}(x)\,\mathrm{d}x \tag{6.30}$$

In the case of $n_g = 2$, $\bar{B}_{ij}^{\prime C}$ vanishes because $B_{ij}'(x)$ is an odd function with respect to $x = a/2$, the center of undulation, due to the assumed form of $h_1(x)$. Furthermore, Eqs. (6.28)–(6.30) coincide with the upper bounds of the compliance of Eqs. (6.19) as a_u tends to zero. The integrations in Eqs. (6.28)–(6.30) are conducted numerically because of the complexity of the integrands. The final results of the average elastic stiffness, $\bar{A}_{ij}^{C}$, $\bar{B}_{ij}^{C}$ and $\bar{D}_{ij}^{C}$, for the entire strip can be reached by the inversion of $\bar{A}_{ij}^{\prime C}$, $\bar{B}_{ij}^{\prime C}$ and $\bar{D}_{ij}^{\prime C}$. If this procedure is applied in the warp direction, balanced properties such as $\bar{A}_{11}^{C} = \bar{A}_{22}^{C}$ can be realized.

Numerical results demonstrating the relationship between the in-plane stiffness, $\bar{A}_{11}$, and $1/n_g$ are given in Fig. 6.18 based upon the unidirectional lamina properties of a carbon/epoxy system (Table 6.2). In Fig. 6.18, UB and LB represent, respectively, the results of the upper and lower bound predictions of the mosaic model; CM denotes the crimp model; circles indicate finite element results. Figure 6.18 demonstrates the reduction in $\bar{A}_{11}$ due to fiber undulation, and the reduction is most severe in plain weave ($1/n_g = 0.5$) as compared to cross-ply laminates ($1/n_g = 0$).

The relationship between the coupling compliance $\bar{B}_{11}'$ and $1/n_g$ is

Fig. 6.18. $\bar{A}_{11}^{C}$ vs. $1/n_g$ for carbon/epoxy composites, $V_f = 60\%$. Finite element results are indicated by (○) for the mosaic model and by (●) for the crimp model. —— mosaic model; - - - - crimp model. (After Ishikawa and Chou 1982b.)

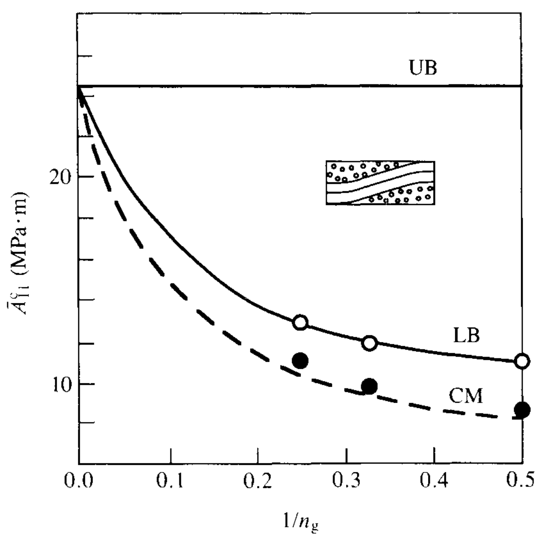

demonstrated in Fig. 6.16. The results from the crimp model coincide exactly with those of the upper bound predictions. This is due to the fact that the second term on the right-hand side of Eq. (6.29) vanishes due to the assumed asymmetrical shape of fiber undulation and, hence, the odd function representation of B'_{ij} with respect to $x = a/2$.

6.6 Bridging model and experimental confirmation

The crimp model which is based upon a single fiber yarn has led to the concept of a bridging model for general satin composites. Such a model is desirable because the interlaced regions in a satin weave are often separated from one another. The hexagonal shape of the repeating unit in a satin weave, as shown in Fig. 6.19, is modified to a square shape (Fig. 6.19b) for simplicity of calculation. A schematic view of the bridging model is shown in Fig. 6.19(c) for a repeating unit which consists of the interlaced region and its surrounding areas. This model is valid only for satin weaves where $n_g \geq 4$. The four regions labeled I, II, IV and V consist of

Fig. 6.19. Concept of the bridging model: (a) shape of the repeating unit of eight-harness satin; (b) modified shape for the repeating unit; (c) idealization for the bridging model. (After Ishikawa and Chou 1982b.)

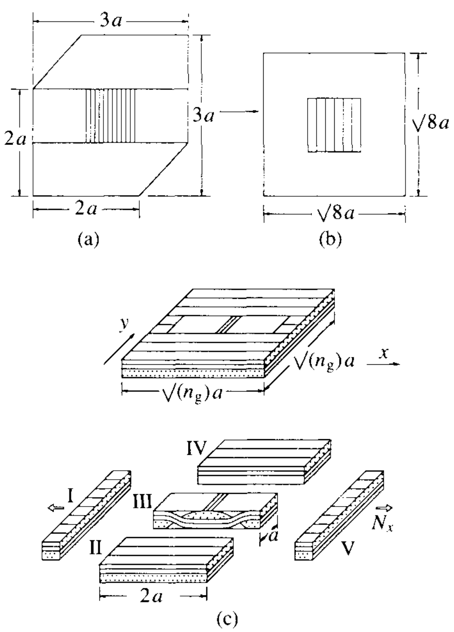

straight filling yarns, and hence can be regarded as pieces of cross-ply laminates of thickness h_t. Region III has an interlaced structure with an undulated filling yarn. Although the undulation and continuity in the warp yarns are ignored in this model, their effect is expected to be small because the applied load is assumed to be in the filling direction.

The in-plane stiffness in region III, where $n_g = 2$, has been derived in Section 6.5 and has been found to be lower than that of a cross-ply laminate. Therefore, regions II and IV carry higher loads than region III; all three of these regions act as bridges for load transfer between regions I and V. It is also assumed that regions II, III and IV have the same average mid-plane strain and curvature. Then, the average stiffness constants for the regions II, III and IV are

$$\begin{aligned}
\bar{A}_{ij} &= \frac{1}{\sqrt{n_g}}[(\sqrt{(n_g)} - 1)A_{ij} + \bar{A}_{ij}^{C}] \\
\bar{B}_{ij} &= \frac{1}{\sqrt{n_g}}(\sqrt{(n_g)} - 1)B_{ij} \\
\bar{D}_{ij} &= \frac{1}{\sqrt{n_g}}[(\sqrt{(n_g)} - 1)D_{ij} + \bar{D}_{ij}^{C}]
\end{aligned} \tag{6.31}$$

$\bar{A}_{ij}^{C}$ and $\bar{D}_{ij}^{C}$ for the undulated portion III in Fig. 6.19 are obtained from $\bar{A}_{ij}^{\prime C}$ and $\bar{D}_{ij}^{\prime C}$ of Eqs. (6.28) and (6.30), and $\bar{B}_{ij}^{\prime C} = 0$. A_{ij}, B_{ij}, and D_{ij} in Eqs. (6.31) for the cross-ply laminates of regions II and IV in Fig. 6.19 are given in Eqs. (6.12).

It is also postulated that the total in-plane force carried by regions II, III and IV is equal to that by region I or V. Then, the following average compliance constants are derived:

$$\begin{aligned}
\bar{A}_{ij}^{\prime S} &= \frac{1}{\sqrt{n_g}}[2\bar{A}_{ij}' + (\sqrt{(n_g)} - 2)A_{ij}'] \\
\bar{B}_{ij}^{\prime S} &= \frac{1}{\sqrt{n_g}}[2\bar{B}_{ij}' + (\sqrt{(n_g)} - 2)B_{ij}'] \\
\bar{D}_{ij}^{\prime S} &= \frac{1}{\sqrt{n_g}}[2\bar{D}_{ij}' + (\sqrt{(n_g)} - 2)D_{ij}']
\end{aligned} \tag{6.32}$$

where $\bar{A}_{ij}'$, $\bar{B}_{ij}'$, and $\bar{D}_{ij}'$ are determined by inverting Eqs. (6.31) and the superscript S denotes properties of the entire satin plane. Finally, $\bar{A}_{ij}^{S}$, $\bar{B}_{ij}^{S}$ and $\bar{D}_{ij}^{S}$ can be obtained by inverting Eqs. (6.32).

The fiber crimp model is effective for plain weave composites whereas the bridging model is valid for satin weave composites. This is because there are no straight yarn regions surrounding an interlaced region in the plain weave. Therefore, no bridging effect is expected in plain weave composites, and the analysis based on the fiber undulation model provides a reasonable prediction of the behavior of plain weave composites.

Numerical results for the relationship between the in-plane elastic stiffness $\bar{A}^S_{11}$ and $1/n_g$ are indicated in Fig. 6.20, also using the unidirectional laminar properties of Table 6.2. A prediction by the present theory agrees with experimental results (Ishikawa and Chou 1982b). It should be noted that the overall fiber volume fraction of a fabric composite is slightly less than that of the impregnated yarns due to the resin rich region in the vicinity of the undulation. For instance, for a fiber volume fraction of 65%, the average overall fiber volume fraction in a repeating unit (Fig. 6.19) for $n_g = 8$, $h_t = h$, and $a_u = a$ is around 62%.

Ishikawa, Matsushima, Hayashi and Chou (1985) have conducted experimental verifications of the analytical models for elastic moduli

Fig. 6.20. $\bar{A}^S_{11}$ vs. $1/n_g$ for carbon/epoxy composites, $V_f = 65\%$. —— Upper and lower bounds; – – – bridging model solution; (▲, ●) experimental results for a cross-ply laminate and eight-harness satin, respectively. (After Ishikawa and Chou 1982b.)

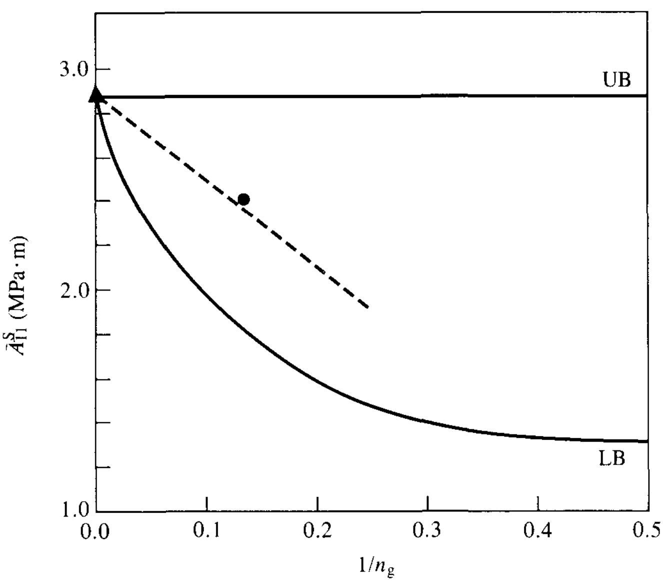

of fabric composites. The experimental materials used include plain weave and eight-harness satin fabric reinforced composites of carbon/epoxy. Ply numbers are 1, 4, 8 and 20 for plain weave fabrics and 2 for eight-harness satin. Yarn orientations are [0°/90°], [15°/−75°], [30°/−60°] and [±45°], as defined by the angles between the loading axis and the yarn direction.

Experimental and theoretical results are compared in Figs. 6.21–6.23. Figure 6.21 presents results of the in-plane stiffness, A_{11}, non-dimensionalized by the corresponding A_{11} of the cross-ply laminate as a function of $1/n_g$. Experimental results of four-ply plain weave and two-ply 8 harness weave composites are given. The symbol ⯁ signifies both the averaged value indicated by the solid circle, and the scattering indicated by the horizontal bars. Theoretical predictions of the bridging model (BM) are adopted for $n_g \geq 4$ and the crimp model (CM) for $4 \geq n_g \geq 2$ according to the reason stated earlier. Abbreviations LWC and LWA denote, respectively, the limiting cases where local warping is completely constrained and allowed. Also, UB and LB are, respectively, upper bound and lower bound predictions of the mosaic model.

A good correlation between theory and experiments can be observed for eight-harness satin composites. The experimental data

Fig. 6.21. Relationships between non-dimensionalized in-plane stiffness and $1/n_g$; ⯁ experiments. (After Ishikawa *et al.* 1985.)

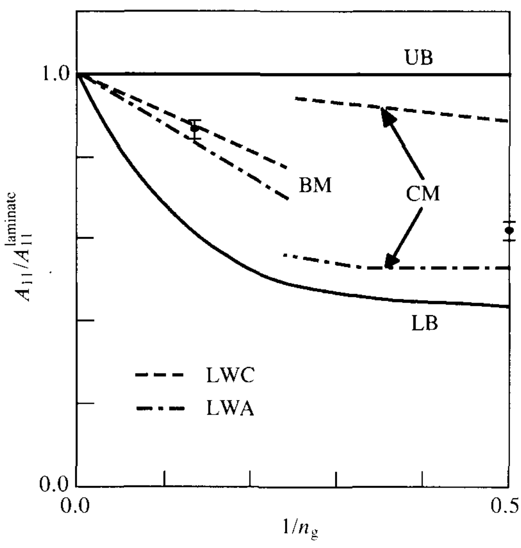

lie in between the LMC and LMA predictions. These results suggest good predictability of the theory based upon the bridging model for satin weave composites. There exists a significant discrepancy between the LWC and LWA curves of plain weave composites even though slight improvement is achieved over the simple bound theory.

Constraint of local warping is another factor governing the in-plane modulus. Neighboring layers in a fabric laminate tend to suppress the warping of one another. Thus, a dependence of elastic moduli on ply number appears for plain weave composites. This effect is demonstrated in Fig. 6.22 where experimental results of specimens of four different ply numbers are indicated. The in-plane stiffness A_{11} of the fabric composite is non-dimensionalized by A_{11} of the cross-ply. Small variations in the theoretical predictions are caused by the scattering of the measured h/a. The in-plane modulus increases from the value for one-ply, which is slightly higher than the LWA prediction, and reaches values slightly lower than the LWC prediction.

The in-plane off-axis elastic moduli results are presented in Fig. 6.23. The off-axis behavior is symmetric with respect to $\phi = 45°$ because it is assumed that the elastic properties in both the filling and warp directions are identical.

In summary, the experimental results of eight-harness satin composites coincide very well with theoretical predictions. There is

Fig. 6.22. Dependence of in-plane stiffness on ply number in plain weave composites: - - - - LWC; —·— LWA; experiments. (After Ishikawa *et al.* 1985.)

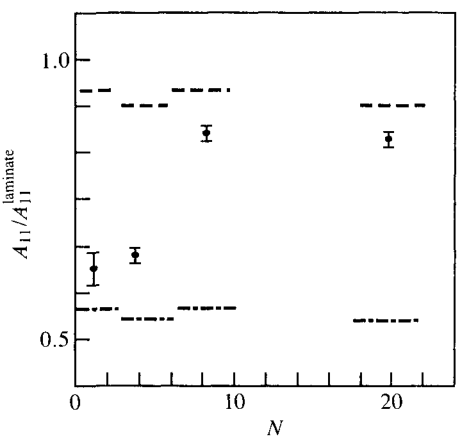

still a discrepancy in the predictions of elastic moduli of plain weave composites based upon two limiting cases: local warping completely prohibited or allowed. All on-axis measured moduli fall in between the two predictions.

6.7 Analysis of the knee behavior and summary of stiffness and strength modeling

Both the crimp model and bridging model described above are now extended to the study of the stress–strain behavior of woven fabric composites after initial fiber failure, known as the *knee phenomenon*. The essential experimental fact for the knee phenomenon is that the breaking strain in the transverse layer, ε_2^b, is much smaller than that of the longitudinal layer in cross-ply laminates. Only the failure of the transverse yarns, which occurs in the warp direction in the present model, is considered. Thus, a failure criterion based upon maximum strain is adopted.

In the following, the crimp model is utilized and attention is confined to the one-dimensional behavior of fabric composites

Fig. 6.23. Off-axis moduli of plain weave and eight-harness satin. E = axial Young's modulus; G = in-plane shear modulus; – – – LWC; —·—: LWA. (After Ishikawa *et al.* 1985.)

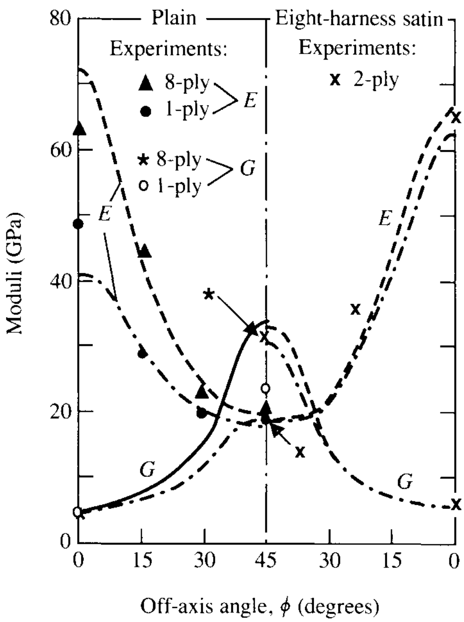

under an applied stress resultant N_x. Then Eq. (6.4) is reduced to

$$\begin{aligned} \varepsilon_{xx}^{o} &= A'_{11}N_x + B'_{11}M_x \\ \kappa_{xx} &= B'_{11}N_x + D'_{11}M_x \end{aligned} \tag{6.33}$$

where M_x is the locally induced moment resultant due to the application of N_x. By assuming first that no bending deflection by the coupling effect is allowed along the x axis,

$$\kappa_{xx} = B'_{11}N_x + D'_{11}M_x = 0 \tag{6.34}$$

This assumption can be realized only if the fabric composite plate is symmetrical with respect to its mid-plane. However, in practical multi-layer fabric composites arranged symmetrically to their mid-planes, this assumption is expected to be approximately true. From Eqs. (6.33) and (6.34)

$$\varepsilon_{xx}^{o} = A''_{11}N_x \tag{6.35}$$

where $A''_{11} = A'_{11} - B'^{2}_{11}/D'_{11}$.

The quantity A''_{11} may be referred to as a *modified in-plane compliance* and it is a function of x. Since N_x is uniform along the x direction, $A''_{11}(x)$ represents a strain distribution before the first transverse matrix cracking. Figure 6.24 depicts two examples of the mid-plane strain distribution relative to that at the point $x = 0$ in Fig. 6.17 and for $a_u = a$. It can easily be seen that the fiber undulation causes local softening and that the maximum strain appears at the center of undulation ($x = a/2$). Also, the strain along the thickness direction at each section is uniform and equal to ε_{xx}^{o} owing to the classical plate theory and the absence of bending. Although the strain distribution calculated from finite element analysis (Ishikawa and Chou 1983b) deviates slightly from the assumed uniform distribution, the present idealization provides a simple method for analyzing the knee phenomenon.

Assume that the region of the highest strain reaches the transverse failure strain ε_2^{b} first, and the damaged area in the warp yarn propagates as the load increases. It is further assumed that classical lamination theory is still valid in this failure process, and that the effective elastic moduli of such a failed region in the warp yarn are much lower than those of a sound area and can be expressed as

$$Q'^{W}_{ij} = \begin{bmatrix} Q^{W}_{11}/100 & Q^{W}_{12}/100 & 0 \\ Q^{W}_{12}/100 & Q^{W}_{22} & 0 \\ 0 & 0 & Q^{W}_{66}/100 \end{bmatrix} \tag{6.36}$$

Here, $Q_{ij}^{\prime W}$ denotes the reduced stiffness of the warp yarns after failure, and it is assumed that, with the exception of Q_{22}^{W}, the Q_{ij} components are reduced by a factor of 1/100 to reflect the weakening effect of transverse cracking. The assumption of the applicability of the classical lamination theory implies that the complex stress and strain fields around the failed region are neglected. Such a successive failure process will continue until the lowest strain in the region reaches ε_2^b. At that time, all the warp regions have failed completely. Beyond this point, the stress–strain curve becomes a straight line again until the final failure of the filling yarns.

Next, consider the case where the restraint on bending is removed. From the classical lamination theory (Chapter 2)

$$\varepsilon_{xx}(z) = \varepsilon_{xx}^{o} + z\kappa_{xx} \tag{6.37}$$

The strain state under an in-plane stress resultant, N_x, is given by

$$\varepsilon_{xx}(z) = (A'_{11} + zB'_{11})N_x \tag{6.38}$$

Thus, the strain field under the prescribed N_x is determined from A'_{11}, B'_{11}, and z. Since the strain in a vertical section is distributed linearly according to Eq. (6.37), it is necessary to determine the height, h_3, where the strain reaches the critical value, ε_2^b. If the

Fig. 6.24. Relative strain distribution along the x axis in the fiber crimp model without bending, $a_u = a$; —— carbon/epoxy; - - - glass/polyester. (After Ishikawa and Chou 1982b.)

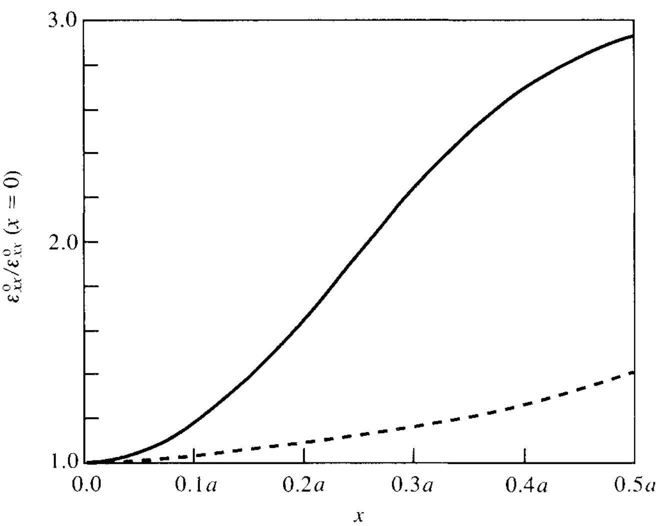

strain at the outer edge of the warp yarns, $\varepsilon_2(h_2)$ according to Eq. (6.37), is larger than ε_2^b, then, for $a_o \le x \le a/2$,

$$h_3(x) = h_2 - (h_2 - h_1)\frac{\varepsilon_2(h_2) - \varepsilon_2^b}{\varepsilon_2(h_2) - \varepsilon_2(h_1)} \tag{6.39}$$

Based upon the h_3 value, the plate stiffness in Eqs. (6.22) needs to be modified after the initial failure. For instance, for $a_o \le x \le a/2$,

$$\begin{aligned} A_{ij}(x) = {} & Q_{ij}^M[h_1(x) - h_2(x) + h - h_t/2] \\ & + Q_{ij}^F(\theta)h_t/2 + Q_{ij}^W[h_3(x) - h_1(x)] + Q_{ij}'^W[h_2(x) - h_3(x)] \end{aligned} \tag{6.40}$$

Modifications similar to Eq. (6.40) are made for B_{ij} and D_{ij} in Eqs. (6.22).

Figure 6.25 presents two numerical examples for a glass/polyester plain weave composite of $a_u = a$ and overall $V_f = 36.8\%$ with and without bending. The finite element analysis and acoustic emission results of Kimpara, Hamamoto and Takehana (1977) are also given. Basic material properties are shown in Table 6.2. The prediction for

Fig. 6.25. Stress–strain curves for plain weave composites of glass/polyester, $V_f = 36.8\%$, and experimental data of acoustic emission; —— analytical results for no bending; – · – · analytical results for unconstrained bending; – – – – finite element simulation; (——) total count in acoustic emission measurement. The vertical arrow indicates the specified value of ε_2^b. (After Ishikawa and Chou 1982b.)

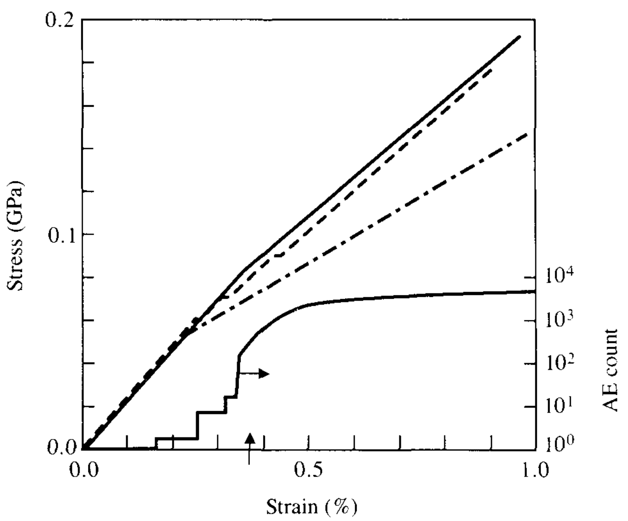

the case without bending compares very favorably with the finite element simulation. It is quite reasonable that the case with bending shows much lower stiffness because it is not subjected to lateral constraints.

In actual plain weave composites, local bending deformation caused by the coupling effect in each interlaced region is constrained by adjacent regions for which the stiffness constants B_{ij} have opposite signs. Therefore, as far as plain weave composites are concerned, one-dimensional analysis for the case without bending should give a reasonable prediction of the knee behavior under in-plane loading.

The bridging model and the process of successive warp yarn failure can be combined to analyze the knee behavior in satin composites. The approaches for plain weave composites are adopted here. First, define the stiffness of the fabric composite under an applied stress resultant N_x without bending to be A_{11}^*. It is noted that $A_{11}^* = 1/A_{11}''$ and the compliance A_{11}'' follows the definition in Eq. (6.35). The average stiffness for regions II, III and IV of Fig. 6.19 is denoted as $\bar{A}_{11}^*$ and calculated by taking the volume average:

$$\bar{A}_{11}^* = (1/\sqrt{n_g})\bar{A}_{11}^{*C} + (1 - 1/\sqrt{n_g})A_{11}^* \tag{6.41}$$

Then the compliance of the whole satin composite is calculated from an average over its length. Define the compliance $\bar{A}_{11}'' = 1/\bar{A}_{11}^*$. The assumption of uniformity of N_x along the x direction leads to

$$\bar{A}_{11}''^{\,S} = (2/\sqrt{n_g})\bar{A}_{11}'' + (1 - 2/\sqrt{n_g})A_{11}''$$

where the superscript S indicates satin composites. Finally, the stiffness of the whole satin composite can be obtained as

$$\bar{A}_{11}^{*S} = 1/\bar{A}_{11}''^{\,S} \tag{6.42}$$

It should be noted that the inversion of the compliance and stiffness constants cannot generally be achieved by merely taking the reciprocal of the respective components (i.e. $C_{ij} \neq 1/S_{ij}$). However, under the assumptions made in the derivations of Eqs. (6.33)–(6.35), Eq. (6.42) is valid for this one-dimensional problem. Expressions similar to Eqs. (6.41) and (6.42) for the case of unconstrained bending can also be obtained but are omitted here. The rest of the procedure for analyzing the knee phenomenon follows that for the plain weave case. The initial failure of the warp yarns occurs at the point of highest strain, for example the center of undulation in the case without bending. Also, since there are regions of uniform strain such as the bridging zones in this model, the entire area of these regions may fail simultaneously, according to the present assumptions.

Figure 6.26 compares numerical and experimental results for stress–strain curves of an eight-harness satin glass fabric/polyimide composite (Table 6.2). Since the test pieces were nearly symmetrical with respect to their mid-planes, the analysis of the case without bending is selected for comparison; the agreement is quite good, particularly for strain values up to the knee point. A theoretical stress–strain curve for a plain weave composite of the same material is also shown in Fig. 6.26. Here, a knee point is defined by a deviation of 0.01% in strain from the linear strain. Then, the knee stress in the eight-harness satin is higher than that of the plain weave, although knee strains are nearly identical. It can be concluded that the elastic stiffness and knee stress in satin composites are higher than those in plain weave composites due to the presence of the bridging zones.

The following is a summary of the stiffness and strength models for two-dimensional orthogonal woven fabric composites:

(1) A fabric composite can be idealized as an assemblage of pieces of asymmetric cross-ply laminates. The upper and

Fig. 6.26. Theoretical and experimental stress–strain curves for glass/polyimide composites, $V_f = 50\%$ in impregnated yarns; —— bridging model solution without bending for eight-harness satin (overall $V_f = 47.7\%$); – – – – fiber undulation model solution without bending for plain weave (overall $V_f = 40.9\%$); — — — experimental curve; (●) knee points. (After Ishikawa and Chou 1982b.)

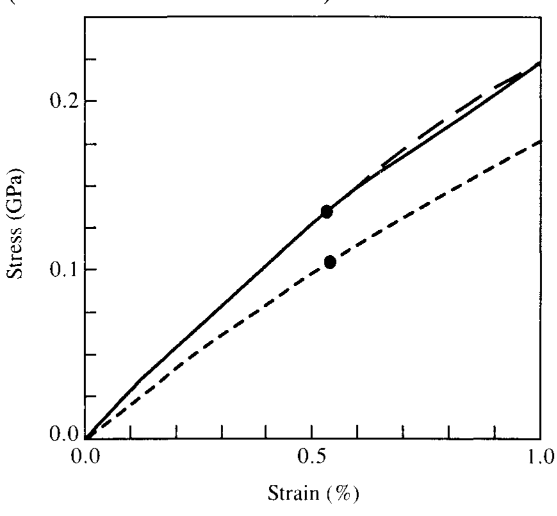

lower bounds of elastic stiffness and compliance of fabric composite plates in such a 'mosaic model' are obtained under the assumption of constant strain and constant stress.

(2) The 'crimp model', which is a one-dimensional approximation and takes into account fiber continuity and undulation, is particularly suited for predicting elastic properties of plain weave composites. The analytical results based upon the crimp model demonstrate that fiber undulation leads to a softening in the in-plane stiffness as compared to the mosaic model. However, fiber undulation has no effect on the coupling constants. Therefore, the solution of the coupling compliance based upon the mosaic model is considered to be reliable.

Both the results of the crimping model and of the mosaic model for the compliance constants $\bar{A}'_{11}$ and $\bar{B}'_{11}$ compare very favorably with the results of a finite element analysis (Ishikawa and Chou 1983b).

(3) In the case of $\bar{D}_{11}$, Ishikawa and Chou (1983b) have adopted a transverse shear deformation theory for a modification of the mosaic model, and examined the response of a fabric composite plate under both cylindrical bending and lateral force. Numerical results of $\bar{D}'_{11}$ based upon the modified transverse shear deformation theory coincide well with the finite element results.

(4) The effect of fiber undulation shapes on $\bar{A}'^{c}_{11}$ in the crimp model is shown in Fig. 6.27. The geometrical parameters a and h are chosen to be 1.0 and 0.4, respectively. The calculations are performed for the range of a_u/h values from 0 to a/h, where the case $a_u \to 0$ corresponds to the configuration of a mosaic model. The results show that $\bar{A}'^{c}_{11}$ is susceptible to the shape of undulation, particularly at small n_g values. The highest $\bar{A}'^{c}_{11}$ value, i.e. the lowest in-plane stiffness, is obtained at around $a_u/h = 1$. On the other hand, the $\bar{A}'^{c}_{11}$ values at $a_u/h = 0$ and a/h are not far apart. Because in actual fabrics $a_u/h \approx a/h$, the mosaic model ($a_u/h = 0$) seems to be effective in evaluating the in-plane stiffness of a fabric.

(5) The crimp model has been applied to examine the knee phenomenon of plain weave composites. The predicted knee behavior of a glass/polyester composite without bend-

ing shows excellent agreement with the stress–strain curve obtained by using a finite element analysis.

(6) The bound method based upon the mosaic model is useful for a rough estimation of fabric composite stiffness properties. The crimp model offers better predictability than the mosaic model for the in-plane and bending moduli. However, the crimp model is inadequate for evaluating the elastic properties of satin weave composites with large n_g.

(7) A bridging model has been developed to examine the stiffness and strength of general satin composites. The interlaced regions in a satin fabric are often separated from one another by the non-interlaced regions. Since the regions with straight yarns surrounding an interlaced region have higher in-plane stiffnesses than the latter, they carry higher loads and play the role of load transferring bridges.

(8) The initial elastic stiffness of satin composites can be predicted by the bridging model. The analysis of an eight-harness satin carbon/epoxy composite demonstrates good agreement with experimental data.

Fig. 6.27. Relationship between average in-plane compliance and undulation length. (After Ishikawa and Chou 1983b.)

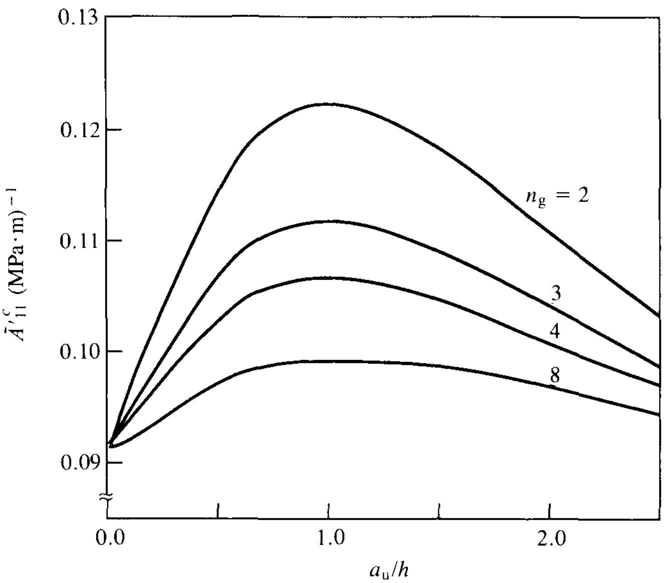

(9) The concept of successive failure of the warp yarns and the bridging idealization have been combined to study the knee behavior in satin composites. The theoretical results for an eight-harness satin glass reinforced polyimide composite compare favorably with the experimental curve. It can be concluded that the bridging regions surrounding an interlaced region are responsible for the higher stiffness and knee stress in strain composites than those in plain weave composites.

6.8 In-plane thermal expansion and thermal bending coefficients

The constitutive equations of a laminated plate taking into account the effects of a small uniform temperature change are given in Eqs. (6.5)–(6.9). In the following, the analytical techniques developed for the mosaic model, crimp model, and bridging model are applied to analyze the thermal problem.

First, for applying the mosaic model, a long strip of the fabric composite (Fig. 6.14a) is again considered. The laminate is free of externally applied load. The average strains and curvatures of a one-dimensional strip of width a along the filling or warp direction due to a uniform temperature change, ΔT, can be expressed in the following forms:

$$\begin{aligned}\bar{\varepsilon}^{\mathrm{o}}_{xx} &= \frac{1}{n_{\mathrm{g}}a}\int_0^{n_{\mathrm{g}}a} \Delta T\tilde{A}'_x(x)\,\mathrm{d}x = \Delta T\tilde{A}'_1\\ \bar{\varepsilon}^{\mathrm{o}}_{yy} &= \frac{1}{n_{\mathrm{g}}a}\int_0^{n_{\mathrm{g}}a} \Delta T\tilde{A}'_y(y)\,\mathrm{d}y = \Delta T\tilde{A}'_2\end{aligned} \tag{6.43}$$

$$\begin{aligned}\bar{\kappa}_{xx} &= \frac{1}{n_{\mathrm{g}}a}\int_0^{n_{\mathrm{g}}a} \Delta T\tilde{B}'_x(x)\,\mathrm{d}x = \Delta T\frac{n_{\mathrm{g}}-2}{n_{\mathrm{g}}}\tilde{B}'_x\\ \bar{\kappa}_{yy} &= \frac{1}{n_{\mathrm{g}}a}\int_0^{n_{\mathrm{g}}a} \Delta T\tilde{B}'_y(y)\,\mathrm{d}y = \Delta T\frac{n_{\mathrm{g}}-2}{n_{\mathrm{g}}}\tilde{B}'_y\end{aligned} \tag{6.44}$$

It should be noted that $\tilde{B}'_x$ has opposite signs in the regions $x = 0$–a and $x = a$–$(n_{\mathrm{g}} - 1)a$; the same is true for $\tilde{B}'_y$.

Because of the nature of the cross-ply laminates $\tilde{A}'_{xy}$ and $\tilde{B}'_{xy}$ vanish. From Eqs. (6.43) and (6.44), the average thermal expansion and thermal bending coefficients for the mosaic model are given by

$$\begin{aligned} &\bar{\tilde{A}}'_x = \tilde{A}'_x, \qquad \bar{\tilde{A}}'_y = \tilde{A}'_y \\ &\bar{\tilde{B}}'_x = \left(1 - \frac{2}{n_g}\right)\tilde{B}'_x, \qquad \bar{\tilde{B}}'_y = \left(1 - \frac{2}{n_g}\right)\tilde{B}'_y \end{aligned} \tag{6.45}$$

Next, the crimp model is applied; the forms of fiber crimp for the filling and warp yarns follow the assumed shapes of Eqs. (6.20) and (6.21), respectively. By assuming no in-plane force and moment and following the derivations of Eqs. (6.43) and (6.44), the fiber crimp model gives

$$\begin{aligned} \bar{\tilde{A}}'^{C}_x &= \left(1 - \frac{2a_u}{n_g a}\right)\tilde{A}'_x + \frac{2}{n_g a}\int_{a_0}^{a_2} \tilde{A}'_x(x)\,dx \\ \bar{\tilde{A}}'^{C}_y &= \left(1 - \frac{2a_u}{n_g a}\right)\tilde{A}'_y + \frac{2}{n_g a}\int_{a_0}^{a_2} \tilde{A}'_y(y)\,dy \end{aligned} \tag{6.46}$$

$$\begin{aligned} \bar{\tilde{B}}'^{C}_x &= \left(1 - \frac{2}{n_g}\right)\tilde{B}'_x + \frac{2}{n_g a}\int_{a_0}^{a_2} \tilde{B}'_x(x)\,dx \\ \bar{\tilde{B}}'^{C}_y &= \left(1 - \frac{2}{n_g}\right)\tilde{B}'_y + \frac{2}{n_g a}\int_{a_0}^{a_2} \tilde{B}'_y(y)\,dy \end{aligned} \tag{6.47}$$

Here, the superscript C signifies the crimp model. It is understood that $\bar{\tilde{A}}'^{C}_{xy}$ and $\bar{\tilde{B}}'^{C}_{xy}$ vanish for cross-ply constructions. Since $\tilde{B}'_x$ and $\tilde{B}'_y$ are odd functions of location with respect to the center of undulation (Eq. (6.20)) the integration in Eqs. (6.47) vanishes and

$$\begin{aligned} \bar{\tilde{B}}'^{C}_x &= \left(1 - \frac{2}{n_g}\right)\tilde{B}'_x \\ \bar{\tilde{B}}'^{C}_y &= \left(1 - \frac{2}{n_g}\right)\tilde{B}'_y \end{aligned} \tag{6.48}$$

The expressions of $\bar{\tilde{B}}'$ from Eqs. (6.45) and (6.48) are identical. Thus, fiber crimp has no effect on the thermal bending coefficients. The same conclusion has been obtained for the extension–bending coupling constant in Section 6.5.

For the in-plane thermal expansion coefficient, it is necessary to evaluate the integration in Eqs. (6.46). This is done on the assumption that the classical laminated plate theory is applicable to each infinitesimal piece of width dx of the one-dimensional strip shown in Fig. 6.17. The following steps are taken to obtain $\tilde{A}'_x(x)$ and $\tilde{A}'_y(y)$. Consider $\tilde{A}'_x(x)$ as an example. First, $\tilde{A}_x(x)$ and $\tilde{B}_x(x)$

are evaluated from Eqs. (6.6) and (6.7) for $0 \leq x \leq a/2$, and the results are

$$\tilde{A}_x(x) = q_x^{\mathrm{M}}(h_1(x) - h_2(x) + h - h_t/2) + q_x^{\mathrm{F}}(\theta)h_t/2 + q_x^{\mathrm{W}}(h_2(x) - h_1(x)) \tag{6.49}$$

$$\tilde{B}_x(x) = \tfrac{1}{2}q_x^{\mathrm{F}}(\theta)(h_1(x) - h_t/4)h_t + \tfrac{1}{4}q_x^{\mathrm{W}}(h_2(x) - h_1(x))h_t \tag{6.50}$$

where the superscripts F, W and M signify the filling yarn, warp yarn, and matrix region, respectively. Next, from Eq. (6.6), $q_x = \bar{Q}_{11}\alpha_{xx} + \bar{Q}_{12}\alpha_{yy} + \bar{Q}_{16}\alpha_{xy}$; $q_x^{\mathrm{F}}(\theta)$, in particular, is determined from the local stiffness matrix $Q_{ij}^{\mathrm{F}}(\theta)$, following the procedures outlined in Section 6.5. Furthermore, the off-axis thermal expansion coefficients are given by

$$\begin{aligned} \alpha_{xx}^{\mathrm{F}}(\theta) &= \cos^2\theta\alpha_{11}^{\mathrm{F}} + \sin^2\theta\,\theta\alpha_{22}^{\mathrm{F}} \\ \alpha_{yy}^{\mathrm{F}}(\theta) &= \alpha_{22}^{\mathrm{F}} \\ \alpha_{xy}^{\mathrm{F}}(\theta) &= 0 \end{aligned} \tag{6.51}$$

where α_{11} and α_{22} denote, respectively, thermal expansion coefficients parallel and transverse to the fiber direction in a unidirectional fiber composite. Thus, $\tilde{A}_x(x)$ and $\tilde{B}_x(x)$ can be determined from Eqs. (6.49) and (6.50). Then, the $\tilde{A}_i'(x)$ and $\tilde{B}_i'(x)$ components are obtained by inverting $\tilde{A}_i(x)$ and $\tilde{B}_i(x)$ as in Eq. (6.9).

Numerical integration of Eqs. (6.46) has been conducted and the results for $\bar{\tilde{A}}_x'^{\mathrm{C}}$ and $\bar{\tilde{B}}_x'^{\mathrm{C}}$ as functions of $1/n_{\mathrm{g}}$ are given in Fig. 6.28. The balanced thermal property such as $\bar{\tilde{A}}_x' = \bar{\tilde{A}}_y'$ for a fabric composite can be realized if the above procedure of calculation is conducted for one-dimensional strips along both the filling and warp directions.

Lastly, the bridging model is applied to analyze the thermal properties. It has been noted in Section 6.6 that regions II and IV of Fig. 6.19 are stiffer than the crimped region III and, hence, they carry more load when an external force is applied in the x direction. Regions II, III and IV are termed *bridging regions*. For the thermal property analysis, assuming no mechanical loading, the equilibrium of the bridging regions requires

$$a\begin{Bmatrix} N^{\mathrm{C}} \\ M^{\mathrm{C}} \end{Bmatrix} + (\sqrt{(n_{\mathrm{g}})} - 1)a\begin{Bmatrix} N \\ M \end{Bmatrix} = 0 \tag{6.52}$$

where the superscript C again denotes the crimped region, and N and M without superscripts are for the cross-ply laminate. Furthermore, under the assumption of uniform strain and curvature in the bridging regions II, III and IV, it is defined that

$$\begin{aligned} \{\varepsilon^{oC}\} &= \{\bar{\varepsilon}^{o}\} \\ \{\kappa^{C}\} &= \{\bar{\kappa}\} \end{aligned} \tag{6.53}$$

where the bar denotes the average of the bridging regions.

Substituting Eq. (6.5) into Eq. (6.52), and taking into account Eqs. (6.53), the results are expressed in the condensed form

$$\left(\left[\begin{array}{c|c} A^{C} & B^{C} \\ \hline B^{C} & D^{C} \end{array}\right] + (\sqrt{(n_g)} - 1)\left[\begin{array}{c|c} A & B \\ \hline B & D \end{array}\right]\right)\left\{\frac{\bar{\varepsilon}^{o}}{\bar{\kappa}}\right\} = \Delta T\left(\left\{\frac{\tilde{A}^{C}}{\tilde{B}^{C}}\right\} + (\sqrt{(n_g)} - 1)\left\{\frac{\tilde{A}}{\tilde{B}}\right\}\right) \tag{6.54}$$

Fig. 6.28. Variation of the thermal deformation coefficients with $1/n_g$ for carbon/epoxy composites, $V_f = 60\%$ and $a_u/a = 1.0$; ——— $\bar{\bar{A}}'_x$; — — — $\bar{\bar{B}}'_x$; (●) experimental results of $\bar{\bar{B}}'_x$ at 300°K. (After Ishikawa and Chou 1983a.)

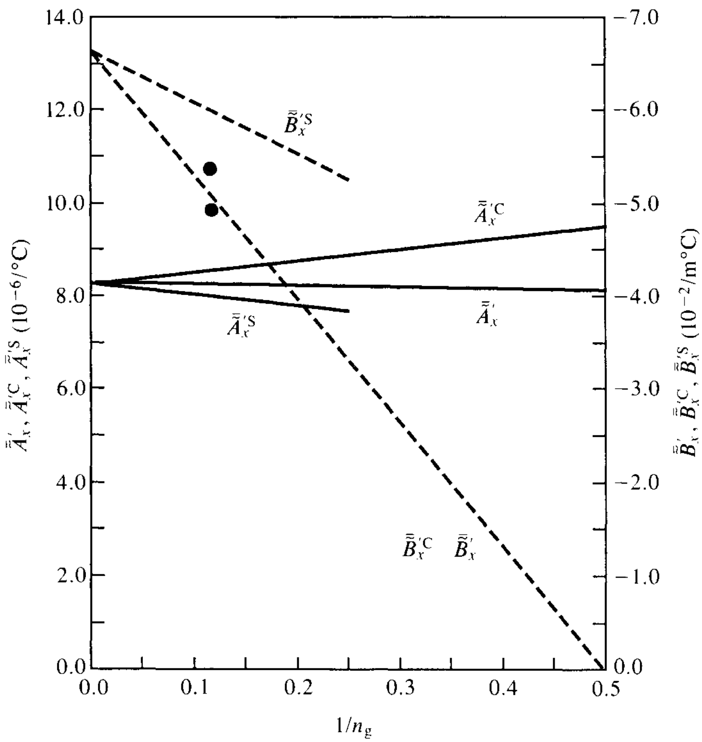

The quantities on the left-hand side of Eq. (6.54) can be related to the average elastic stiffness in the bridging regions as

$$\left[\begin{array}{c|c} A^{\mathrm{C}} & B^{\mathrm{C}} \\ \hline B^{\mathrm{C}} & D^{\mathrm{C}} \end{array}\right] + (\sqrt{(n_{\mathrm{g}})} - 1)\left[\begin{array}{c|c} A & B \\ \hline B & D \end{array}\right] = \sqrt{n_{\mathrm{g}}}\left[\begin{array}{c|c} \bar{A} & \bar{B} \\ \hline \bar{B} & \bar{D} \end{array}\right] \tag{6.55}$$

Hence, Eq. (6.54) can be written as

$$\begin{aligned} \left\{\frac{\bar{\varepsilon}^{\mathrm{o}}}{\bar{\kappa}}\right\} = \Delta T \left[\begin{array}{c|c} \bar{A}' & \bar{B}' \\ \hline \bar{B}' & \bar{D}' \end{array}\right]\Bigg(\frac{1}{\sqrt{n_{\mathrm{g}}}}\left\{\frac{\tilde{A}^{\mathrm{C}}}{\tilde{B}^{\mathrm{C}}}\right\} \\ + \left(1 - \frac{1}{\sqrt{n_{\mathrm{g}}}}\right)\left\{\frac{\tilde{A}}{\tilde{B}}\right\}\Bigg) \end{aligned} \tag{6.56}$$

Here, $\bar{A}'_{ij}$, $\bar{B}'_{ij}$, and $\bar{D}'_{ij}$ are obviously obtained by inverting $\bar{A}_{ij}$, $\bar{B}_{ij}$, and $\bar{D}_{ij}$. In comparison to Eq. (6.8) the quantities in the parentheses on the right-hand side of Eq. (6.56) can be regarded as the average values for the bridging regions and hence they are denoted by $\bar{\tilde{A}}^*_{\mathrm{j}}$ and $\bar{\tilde{B}}^*_j$. Thus, we obtain, in index notation

$$\left\{\frac{\bar{\tilde{A}}'_i}{\bar{\tilde{B}}'_i}\right\} = \left[\begin{array}{c|c} \bar{A}'_{ij} & \bar{B}'_{ij} \\ \hline \bar{B}'_{ij} & \bar{D}'_{ij} \end{array}\right]\left\{\frac{\bar{\tilde{A}}^*_j}{\bar{\tilde{B}}^*_j}\right\} \tag{6.57}$$

Finally, the whole satin composite of Fig. 6.19 can be regarded as a linkage of regions I, II–III–IV and V in series. The average strain and curvature for the entire model are given in condensed form as

$$\begin{aligned} \left\{\frac{\bar{\varepsilon}^{\mathrm{oS}}}{\bar{\kappa}^{\mathrm{S}}}\right\} &= \frac{1}{\sqrt{n_{\mathrm{g}}}}\left(2\left\{\frac{\bar{\varepsilon}^{\mathrm{o}}}{\bar{\kappa}}\right\} + (\sqrt{(n_{\mathrm{g}})} - 2)\left\{\frac{\varepsilon^{\mathrm{o}}}{\kappa}\right\}\right) \\ &= \Delta T\left(\frac{2}{\sqrt{n_{\mathrm{g}}}}\left\{\frac{\bar{\tilde{A}}'}{\bar{\tilde{B}}'}\right\} + \left(1 - \frac{2}{\sqrt{n_{\mathrm{g}}}}\right)\left\{\frac{\tilde{A}'}{\tilde{B}'}\right\}\right) \end{aligned} \tag{6.58}$$

where the superscript s signifies the properties of the satin composite, and ε^{o} and κ denote, respectively, mid-plane strain and curvature for the cross-plies in regions I and V of Fig. 6.19. From Eq. (6.58), the components of the thermal expansion and thermal bending coefficients of the satin composite are expressed as

$$\left\{\frac{\bar{\tilde{A}}'^{\mathrm{S}}_i}{\bar{\tilde{B}}'^{\mathrm{S}}_i}\right\} = \frac{2}{\sqrt{n_{\mathrm{g}}}}\left\{\frac{\bar{\tilde{A}}'_i}{\bar{\tilde{B}}'_i}\right\} + \left(1 - \frac{2}{\sqrt{n_{\mathrm{g}}}}\right)\left\{\frac{\tilde{A}_i}{\tilde{B}'_i}\right\} \tag{6.59}$$

Figure 6.28 shows the numerical results of the analysis based upon the elastic properties of Table 6.2. Also, $\alpha_{11} = 0.0$ and $\alpha_{22} = 3.0 \times 10^{-5}/°\mathrm{C}$. The general characteristics of the variations of thermal deformation coefficients with $1/n_g$ are very similar to those of the compliance constants $\bar{A}'_{11}$ and $\bar{B}'_{11}$ as discussed earlier. For the thermal bending coefficients, there is considerable discrepancy between the results obtained from the one-dimensional models and the bridging model.

The geometrical shape of the fiber undulation also affects $\bar{\bar{A}}'_x$; this is demonstrated in Fig. 6.29 using the carbon/epoxy properties of Table 6.2. The results indicate that the in-plane thermal expansion coefficient of satin weave composites is less sensitive to a_u/h than that of plain weave composites. Furthermore, the fiber crimp model predicts a larger effect on $\bar{\bar{A}}'_x$ due to a_u/h than the bridging model. In general, the bridging model predictions are also less sensitive to the n_g values than the crimp model predictions. In both models, the maximum in $\bar{\bar{A}}'_x$ occurs at $a_u/h \approx 1$.

Experimental data on thermal expansion coefficients of fabric

Fig. 6.29. The effect of fiber undulation on $\bar{\bar{A}}'_x$ of carbon/epoxy composites; solid lines: crimp model; broken lines: bridging model. (After Ishikawa and Chou 1983a.)

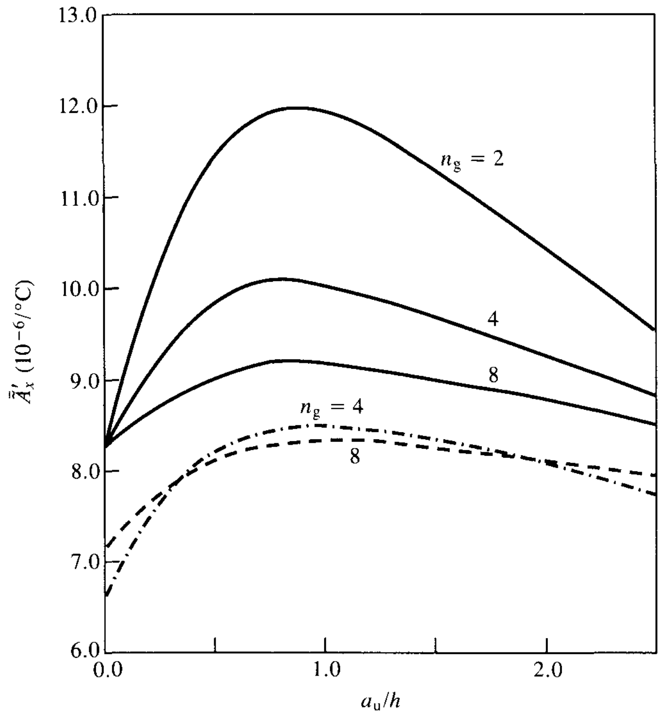

composites are quite limited. Rogers *et al.* (1977, 1981) and Yates *et al.* (1978) have performed measurements of thermal expansion of carbon fiber reinforced plastics. These experiments, however, are based upon thick specimens with 15–25 plies. Due to the constraint of the neighboring layers, an individual ply in the laminate is not free to bend. As a result, modifications to the analysis developed above are necessary for making a meaningful comparison with experiments.

It is assumed that the thermal expansion of a lamina without bending can be realized if there exist bending moments $\{M\}$, under a temperature change, ΔT, and no in-plane force is allowed. Thus,

$$\{N\} = \{\kappa\} = 0 \tag{6.60}$$

Equations (6.8) and (6.60) give

$$[D']\{M\} + \Delta T\{\tilde{B}'\} = 0 \tag{6.61}$$

Then,

$$\{M\} = -\Delta T[D']^{-1}\{\tilde{B}'\} \tag{6.62}$$

Substituting Eq. (6.62) into Eq. (6.8), and from the expression of ε°, a modified in-plane thermal expansion coefficient for the case without in-plane force and external bending can be defined as

$$\{\tilde{A}''\} = \{\tilde{A}'\} - [B'][D']^{-1}\{\tilde{B}'\} \tag{6.63}$$

Equation (6.63) can be evaluated for the mosaic, crimp and bridging models provided that the appropriate constants are given for a particular model. Also, note the presence of elastic compliance constants in Eq. (6.63). Thus, it is necessary to evaluate, for instance, $\bar{B}'^{S}_{ij}$ and $\bar{D}'^{S}_{ij}$ for calculating $\tilde{A}''^{S}$, and $\bar{B}'^{C}_{ij}$ and D'^{C}_{ij} for $\tilde{A}''^{C}$. The above modifications are of practical significance because it is desirable to overcome the anti-symmetrical behavior such as that of $\tilde{B}'_i$ by suitable stacking in laminate constructions.

Figure 6.30 gives the variation of $\tilde{A}'_1$ with $1/n_g$. The theoretical predictions are based upon both the crimp and bridging models using the thermoelastic properties of the unidirectional carbon/epoxy composite of Table 6.2. The experimental results of Rogers *et al.* (1981) for five-harness satin composites are also shown in Fig. 6.30. Two estimated values for a/h were used for the analysis, and a/a_u is assumed to be unity. The bridging model prediction coincides fairly well with experimental results. It is also obvious that the in-plane thermal expansion coefficients are more sensitive to n_g in the case without bending (Fig. 6.30) than in the case of unconstrained bending (Fig. 6.28).

In summary, the following can be stated regarding the thermal property modeling of two-dimensional woven fabric composites:

(1) The mosaic model provides a simple means for estimating thermal expansion and thermal bending coefficients.
(2) The one-dimensional crimp model predicts slightly higher in-plane thermal expansion coefficients and the same thermal bending coefficients compared to those obtained from the mosaic model. The limited experimental data on thermal bending coefficients coincide rather well with the predictions of the mosaic and crimp models.

Fig. 6.30. Comparison of theoretical predictions with the experimental results of Rogers *et al.* (1981) for five-harness satin carbon/epoxy composites; —— $a/h = 3.75$; — — — $a/h = 7.5$; $a_u/a = 1.0$; CM and BM indicate fiber crimp and bridging models, respectively; (●) experimental results at 300 K. (After Ishikawa and Chou 1983a.)

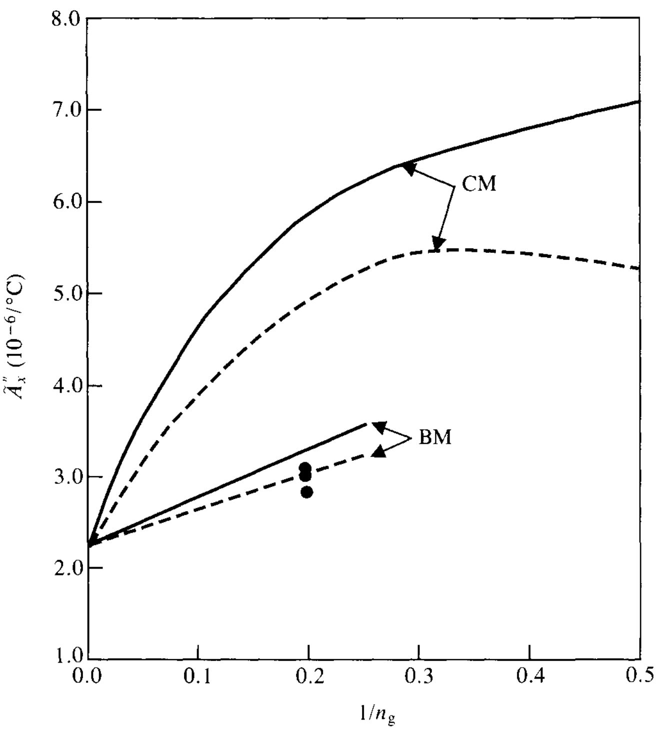

(3) The bridging model is particularly suited for the prediction of thermal expansion constants for satin composites. The experimental results on in-plane thermal expansion coefficients for a five-harness satin composite agree well with the theory.

6.9 Hybrid fabric composites: mosaic model

Hybrid woven fabrics provide a wide variety of material selection for designers with a new degree of freedom in tailoring composites to achieve a better balance of stiffness and strength, increased elongation to failure, better damage tolerance, and significant improvement of cost-effectiveness in fabrication. A basic difference between hybrid and non-hybrid composites is that material variation as well as geometrical variation come into play for the former case.

Figure 6.31 shows an example of a hybrid fabric composite for $n_g = 8$. The front view is dominated by filling yarns and the back side by warp yarns. There are two kinds of fiber materials, denoted by α and β, although there is no restriction regarding the number of fiber materials in a hybrid fabric. For the case of Fig. 6.31, the pattern of arrangement of fiber types in the filling direction repeats

Fig. 6.31. A hybrid woven fabric with $n_g = 8$, $n_{fm} = 2$ and $n_{wm} = 3$. (a) Front view; (b) back view. (After Ishikawa and Chou 1982a.)

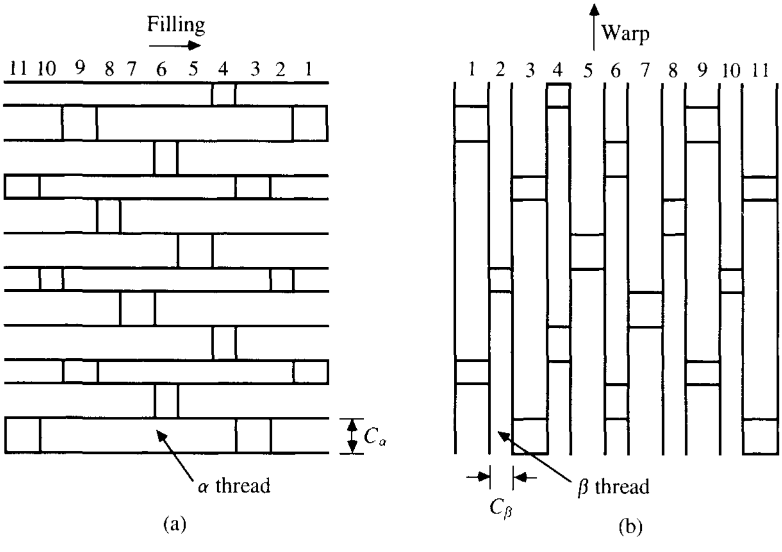

for every two warp yarns; thus it is defined that $n_{fm} = 2$. In the warp direction, the pattern of arrangement of fiber types repeats for every three filling yarns, and $n_{wm} = 3$. The subscript 'm' indicates a material parameter. The following analysis is limited to fabrics containing only two types of fiber densely woven in both directions, i.e. no gaps are allowed (Ishikawa and Chou 1982a, 1983d).

6.9.1 *Definitions and idealizations*

It has been adopted that n_g ($=n_{fg} = n_{wg}$) specifies the fabric geometrical pattern, and n_{fm} and n_{wm} define the fabric material arrangements. The notation n_m will be used when consideration of the material parameter is not restricted to any one direction.

In the following, the discussions are first focussed on the pattern of hybrid fabrics in one dimension, along the filling or warp direction. Under the assumption of the mosaic model (Section 6.4), a fabric composite can simply be regarded as an assemblage of pieces of asymmetrical cross-ply laminates.

If n_g and n_m are numbers not divisible by each other in a given direction, warp or filling, the pattern of the hybrid fabric will repeat in that direction for every $n_g \times n_m$ yarns in the orthogonal fabric. For instance, for $n_g = 5$ and $n_{fm} = 3$, Fig. 6.32 shows the pattern of fabric repeats in the filling direction for every 15 warp yarns. In general, the pattern of a fabric is repeated in the filling direction after every n_f warp yarns, where n_f is the least common multiple (LCM) of n_{fg} and n_{fm}, or $n_f = \mathrm{LCM}(n_{fg}, n_{fm})$. Similarly, it is defined that $n_w = \mathrm{LCM}(n_{wg}, n_{wm})$.

Although the size of a basic repeating unit in the filling direction, for instance, is determined by n_f, the detail of fiber arrangement

Fig. 6.32. A fabric where n_g and n_{fm} are not divisible by each other in the filling direction; α and β denote two types of fibers. (After Ishikawa and Chou 1982a.)

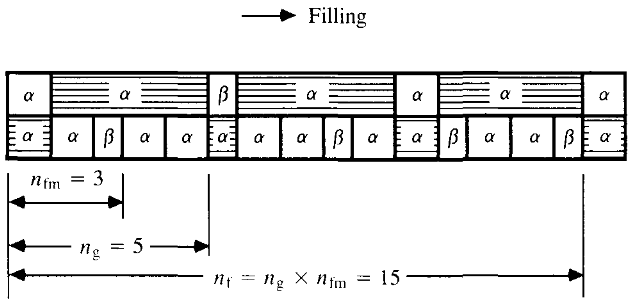

may vary. Figure 6.33 shows two cases of fabric pattern in the filling direction for $n_{fg} = 8$. Here, α and β denote the two types of fiber material of the hybrid. The notation ξ is used to indicate that the filling yarn can be of either α or β type. It is obvious from Fig. 6.33 that the different repeating patterns are generated by continuously shifting the positions of the warp yarns in the filling direction. In general, the number of repeating patterns in the filling direction for a given n_f is equal to the greatest common measure (GCM) of n_{fg} and n_{fm} and is denoted by $n_{fi} = \mathrm{GCM}(n_{fg}, n_{fm})$. Naturally, $n_{fi} = 1$ for the case of Fig. 6.32. Again the notation n_i can be used if the discussion is independent of the direction.

Further comments are necessary for identifying the nature of the interlaced regions of a hybrid fabric. In Fig. 6.33 the interlaced region is 'homogeneous' if the yarns are identical or 'heterogeneous' if the yarns are of different types. The notations $\mathrm{HO1}^{\alpha}$, $\mathrm{HE3}^{\beta}$, etc. are simply for identification purposes pertaining to later discussions. The types of interlacing are termed 'mixed' if both homogeneous and heterogeneous interlacing appear in a repeating pattern. This can occur when n_g and n_m are numbers not divisible (Fig. 6.32) or divisible (for instance $n_g = 8$, $n_{fm} = 4$) by each other.

Fig. 6.33. Homogeneous and heterogeneous interlacings. (a) $n_{fg} = 8$, $n_{fm} = 2$ ($n_{fm}^{\alpha} = n_{fm}^{\beta} = 1$); (b) $n_{fg} = 8$, $n_{fm} = 4$ ($n_{fm}^{\alpha} = 3$, $n_{fm}^{\beta} = 1$). (After Ishikawa and Chou 1982a.)

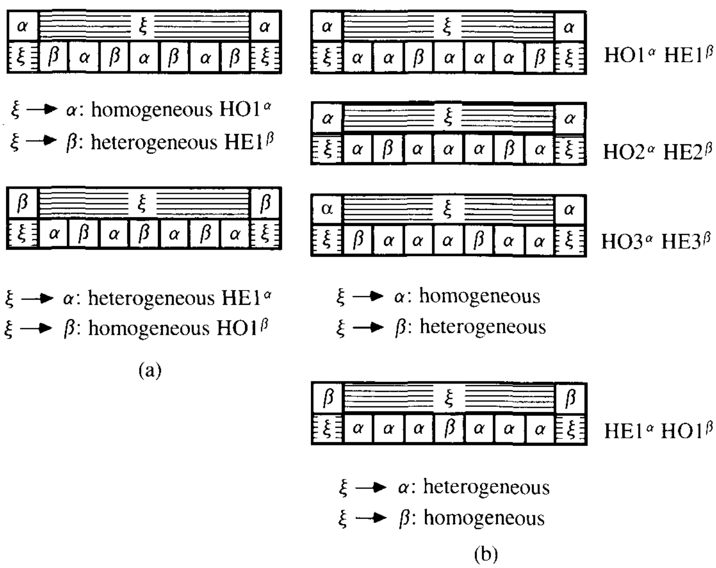

Fig. 6.34. Two-dimensional basic repeating unit of a hybrid fabric for $n_g = 8$ and $n_{fm} = 4$. (a) n, n_g and n_{wm} are not divisible by each other. (b) $n_{wm} = 4$; n_g and n_{wm} are divisible by each (1) mixed interlacing; (2) homogeneous interlacing. (After Ishikawa and Chou, 1982a.)

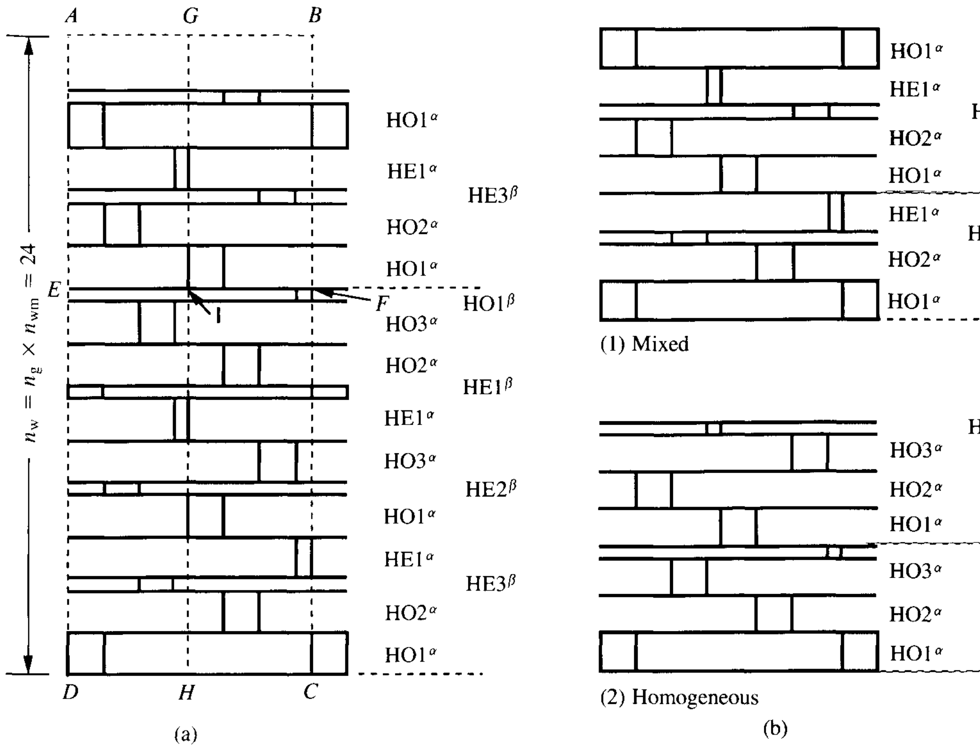

Next, hybrid fabric patterns in two dimensions are identified on the basis of the above definitions established for one-dimensional considerations. Figure 6.34 shows hybrid fabric patterns for $n_g = 8$, $n_{fm} = 4$, and $n_{wm} = 3$ (Fig. 6.34a) and $n_{wm} = 4$ (Fig. 6.34b). It should be noted that all the interlacing patterns of Fig. 6.33(b) appear in Fig. 6.34(a). The area denoted *ABCD* in Fig. 6.34(a) is a possible repeating unit of the fabric. However, there are repetitions in the geometrical and material patterns within this area. The patterns of *AGIE* and *IFCH* are identical. So are the patterns of *GBFI* and *EIHD*. Consequently, the smallest repeating unit of the fabric in two dimensions can be represented by either *AGHD* or *EFCD*. The area *EFCD*, for instance, contains 12 ($n_g n_{wm}/(n_g/n_{fi})$) filling yarns. It can be further concluded that if n_g and n_m are numbers not divisible by each other in one direction (filling or warp) there exists only one kind of basic repeating unit for defining the two-dimensional fabric. This is true regardless of whether n_g and n_m are numbers divisible or not by each other in the other direction.

On the other hand, there exists more than one type of basic repeating unit in the two-dimensional fabric if n_g and n_m are numbers divisible by each other in both directions. This is illustrated in Fig. 6.34(b). In Fig. 6.34(b1) both homogeneous and heterogeneous interlacing in the filling direction occur and the pattern is considered to be 'mixed' in two dimensions. The pattern is homogeneous in two dimensions for Fig. 6.34(b2). Two other mixed patterns exist: [HO1$^\alpha$, HE2$^\beta$, HO3$^\alpha$, HE1$^\alpha$] and [HE1$^\beta$, HO2$^\alpha$, HO3$^\alpha$, HE1$^\alpha$], and no heterogeneous pattern exists for the geometrical and material parameters given in Fig. 6.34(b).

Let l_f and l_w be the edge lengths of a basic repeating unit in a two-dimensional fabric. If n_g and n_{wm} are numbers not divisible by each other for the repeating unit *AGHD* in Fig. 6.34(a).

$$\begin{aligned} l_w &= (n_{wm}^\alpha C_\alpha + n_{wm}^\beta C_\beta) n_g \\ l_f &= n_{fm}^\alpha C_\alpha + n_{fm}^\beta C_\beta \end{aligned} \tag{6.64}$$

C_α and C_β denote yarn widths as shown in Fig. 6.31. The area of the two-dimensional repeating unit is then given by

$$A_r = n_g (n_{wm}^\alpha C_\alpha + n_{wm}^\beta C_\beta)(n_{fm}^\alpha C_\alpha + n_{fm}^\beta C_\beta) \tag{6.65}$$

This equation is valid for n_g and n_m, which are numbers not divisible by each other in either the filling or the warp direction as well as in both directions.

Alternate expressions for Eqs. (6.64) can be given by considering the repeating unit of *EFCD* in Fig. 6.34(a):

$$l_{\mathrm{w}}=(n_{\mathrm{wm}}^{\alpha}C_{\alpha}+n_{\mathrm{wm}}^{\beta}C_{\beta})n_{\mathrm{fi}}$$
$$l_{\mathrm{f}}=(n_{\mathrm{fm}}^{\alpha}C_{\alpha}+n_{\mathrm{fm}}^{\beta}C_{\beta})n_{\mathrm{g}}/n_{\mathrm{fi}} \tag{6.66}$$

When n_{g} and n_{m} are numbers divisible by each other in both directions

$$A_{\mathrm{r}}=\frac{n_{\mathrm{w}}}{n_{\mathrm{wm}}}(n_{\mathrm{wm}}^{\alpha}C_{\alpha}+n_{\mathrm{wm}}^{\beta}C_{\beta})(n_{\mathrm{fm}}^{\alpha}C_{\alpha}+n_{\mathrm{fm}}^{\beta}C_{\beta}) \tag{6.67}$$

for $n_w \geq n_{\mathrm{f}}$, and

$$A_{\mathrm{r}}=\frac{n_{\mathrm{f}}}{n_{\mathrm{fm}}}(n_{\mathrm{wm}}^{\alpha}C_{\alpha}+n_{\mathrm{wm}}^{\beta}C_{\beta})(n_{\mathrm{fm}}^{\alpha}C_{\alpha}+n_{\mathrm{fm}}^{\beta}C_{\beta}) \tag{6.68}$$

for $n_{\mathrm{f}} \geq n_{\mathrm{w}}$.

In summary, the pattern of a regular hybrid satin fabric can be determined by the parameters C_{α}, C_{β}, n_{g}, n_{m} and, hence, n_{i}, n_{f} and n_{w}. The 'regularity' of fabrics deserves some comment. The concept of regularity is based on the geometrical consideration. For instance, in the regular satin weave of Fig. 6.3(d), the geometrical distribution of the interlaced regions in two dimensions can be determined uniquely by two vectors, i.e. (3, 1) and (1, 3). The vector (3, 1) translates to an interlaced region by three yarns in the filling direction and one yarn in the warp direction. Other combinations of vectors are also possible, for instance (3, 1) and (−2, 2) or (2, −2) and (1, 3). An example of an irregular satin is shown in Fig. 6.3(c), where $n_{\mathrm{g}}=4$ and a set of two vectors cannot be found to generate the locations of all the interlaced regions. The term 'balanced' hybrid fabric is also used in the analysis. In such a fabric, the total number and arrangements of yarns of each material in the filling and warp directions are identical. Hence, the relations $A_{11}=A_{22}$, $D_{11}=D_{22}$ and $B_{11}=-B_{22}$ hold for a balanced hybrid fabric.

6.9.2 *Bounds of stiffness and compliance constants*

On the basis of the idealizations given in Fig. 6.13, the hybrid fabric composite can be modeled as an assemblage of pieces of cross-ply laminates. It is further assumed that the shear deformation in the thickness direction is neglected.

There exist four different types of material combinations in a cross-ply asymmetrical laminate as depicted in Fig. 6.35, where the upper lamina is assumed to be composed of filling yarns. In the superscripts used in Fig. 6.35 the first Greek letter identifies the upper layer material and the second letter is for the lower layer. The derivations of the components of A_{ij}, B_{ij} and D_{ij} of Eqs. (6.3) for the hybrid fabric composites are straightforward. Also, it is understood that the cross-terms A_{16}, A_{26}, B_{16}, B_{26}, D_{16} and D_{26} for these asymmetrical cross-ply laminates vanish; this is also true when the upper lamina is composed of warp yarns.

6.9.2.1 *Iso-strain*

The distributions of stress resultant (and moment) and strain (and curvature) over the laminate mid-plane vary with location in the hybrid fabric composite. As a first approximation, the assumption of iso-strain in the mid-plane is adopted. Equations (6.3) are then applied to a fundamental region in the laminate. This region, if repeated, should reproduce the geometrical and material arrangements of the entire idealized fabric. Thus, the behavior of the fundamental region should reflect that of the whole laminate. The dimensions of the fundamental region are denoted by l_f and l_w in the filling and warp directions, respectively. It is also defined that $r = C_\beta / C_\alpha$ (see Fig. 6.31).

Fig. 6.35. Material combinations in a cross-ply asymmetrical laminate. The elastic constants for the plies are denoted by: (a) $A_{ij}^{\alpha\alpha}$, $B_{ij}^{\alpha\alpha}$, $D_{ij}^{\alpha\alpha}$, $A_{ij}^{\prime\alpha\alpha}$, $B_{ij}^{\prime\alpha\alpha}$ and $D_{ij}^{\prime\alpha\alpha}$; (b) $A_{ij}^{\alpha\beta}$, $B_{ij}^{\alpha\beta}$, $D_{ij}^{\alpha\beta}$, $A_{ij}^{\prime\alpha\beta}$, $B_{ij}^{\prime\alpha\beta}$ and $D_{ij}^{\prime\alpha\beta}$; (c) $A_{ij}^{\beta\alpha}$, $B_{ij}^{\beta\alpha}$, $D_{ij}^{\beta\alpha}$, $A_{ij}^{\prime\beta\alpha}$, $B_{ij}^{\prime\beta\alpha}$ and $D_{ij}^{\prime\beta\alpha}$; (d) $A_{ij}^{\beta\beta}$, $B_{ij}^{\beta\beta}$, $D_{ij}^{\beta\beta}$, $A_{ij}^{\prime\beta\beta}$, $B_{ij}^{\prime\beta\beta}$ and $D_{ij}^{\prime\beta\beta}$. (After Ishikawa and Chou 1982a.)

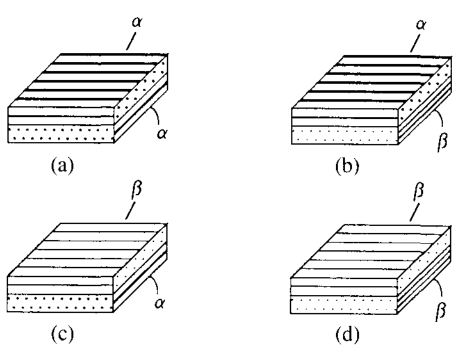

(A) $\bar{A}_{ij}$ and $\bar{D}_{ij}$

The average stress resultant $\bar{N}_x$, for example, is given as an average over the fundamental region in the x–y plane:

$$\bar{N}_x = \frac{1}{l_f l_w} \int_0^{l_w} \int_0^{l_f} N_x \, dx \, dy$$
$$= \frac{1}{l_f l_w} \int_0^{l_w} \int_0^{l_f} [A_{11}^{\xi\eta} \varepsilon_{xx}^o + A_{12}^{\xi\eta} \varepsilon_{yy}^o + B_{11}^{\xi\eta} \kappa_{xx} + B_{12}^{\xi\eta} \kappa_{yy}] \, dx \, dy \tag{6.69}$$

Here, ξ and η stand for the α and β material phases. From Eq. (6.69) the following expressions for the effective stiffness constants of a hybrid fabric composite are given:

$$(\bar{A}_{ij}, \bar{B}_{ij}, \bar{D}_{ij}) = \frac{1}{l_f l_w} \int_0^{l_w} \int_0^{l_f} (A_{ij}^{\xi\eta}, B_{ij}^{\xi\eta}, D_{ij}^{\xi\eta}) \, dx \, dy \tag{6.70}$$

These averages, in their simple forms, provide upper bounds for the fabric composite stiffness. If these stiffness constants are inverted, lower bounds for the elastic compliance constants can also be obtained.

Both $A_{ij}^{\xi\eta}$ and $D_{ij}^{\xi\eta}$ for the upper ply are identical to those for the lower ply; general expressions of $\bar{A}_{ij}$ and $\bar{D}_{ij}$ can be written regardless of the relative magnitude of n_g and n_m. For instance,

$$\bar{A}_{ij} = \frac{1}{(n_{fm}^{\alpha} + n_{fm}^{\beta} r)(n_{wm}^{\alpha} + n_{wm}^{\beta} r)}$$
$$\times [n_{fm}^{\alpha} n_{wm}^{\alpha} A_{ij}^{\alpha\alpha} + (n_{fm}^{\beta} n_{wm}^{\alpha} A_{ij}^{\alpha\beta}$$
$$+ n_{fm}^{\alpha} n_{wm}^{\beta} A_{ij}^{\beta\alpha}) r + n_{fm}^{\beta} n_{wm}^{\beta} A_{ij}^{\beta\beta} r^2] \tag{6.71}$$

where n_{fm}^{α} and n_{fm}^{β} denote the number of α and β yarns, respectively, within the repeating length of n_{fm} yarns in the filling direction. Naturally, $n_{fm}^{\alpha} + n_{fm}^{\beta} = n_{fm}$, and $n_{wm}^{\alpha} + n_{wm}^{\beta} = n_{wm}$. The expression for $\bar{D}_{ij}$ can be obtained if $A_{ij}^{\xi\eta}(\xi, \eta = \alpha, \beta)$ in Eq. (6.71) are replaced by $D_{ij}^{\xi\eta}$. Finally, it should be noted that $\bar{A}_{ij}$ and $\bar{D}_{ij}$ can be reduced to the special case of non-hybrid fabric composites (Ishikawa and Chou 1983b). The upper bounds of $\bar{A}_{ij}$ and $\bar{D}_{ij}$ thus obtained are identical to those of A_{ij} and D_{ij} of intermingled hybrids in cross–ply laminate form.

(B) $\bar{B}_{ij}$

The $\bar{B}_{ij}$ constants can be obtained with the same approach as for $\bar{A}_{ij}$ and $\bar{D}_{ij}$. However, here it is necessary to distinguish the weaving pattern as indicated by n_g and n_m. Hence, the algebra is more complicated. If n_g and n_m are numbers not divisible by each other in one direction

$$\bar{B}_{ij} = \frac{(n_g - 2)}{n_g} \frac{1}{(n_{fm}^{\alpha} + n_{fm}^{\beta} r)(n_{wm}^{\alpha} + n_{wm}^{\beta} r)} \times [n_{fm}^{\alpha} n_{wm}^{\alpha} B_{ij}^{\alpha\alpha} + (n_{fm}^{\beta} n_{wm}^{\alpha} B_{ij}^{\alpha\beta} + n_{fm}^{\alpha} n_{wm}^{\beta} B_{ij}^{\beta\alpha}) r + n_{fm}^{\beta} n_{wm}^{\beta} B_{ij}^{\beta\beta} r^2] \tag{6.72}$$

In the case where n_g and n_m are numbers divisible by each other in both directions, the expression of $\bar{B}_{ij}$ depends upon whether the interlacing is homogeneous, heterogeneous or mixed. For instance, for the case of homogeneous interlacing where $n_f \geq n_w$

$$\bar{B}_{ij} = \frac{1}{n_g (n_{fm}^{\alpha} + n_{fm}^{\beta} r)(n_{wm}^{\alpha} + n_{wm}^{\beta} r)} \times [(n_g n_{fm}^{\alpha} - 2n_{fi}) n_{wm}^{\alpha} B_{ij}^{\alpha\alpha} + n_g (n_{fm}^{\beta} n_{wm}^{\alpha} B_{ij}^{\alpha\beta} + n_{fm}^{\alpha} n_{wm}^{\beta} B_{ij}^{\beta\alpha}) r + (n_g n_{fm}^{\beta} - 2n_{fi}) n_{wm}^{\beta} B_{ij}^{\beta\beta} r^2] \tag{6.73}$$

Similar expressions can be derived for heterogeneous interlacing. In the case of mixed interlacing, the expressions depend upon the details of the material arrangement. However, the differences among the B_{ij}s for homogeneous, heterogeneous and mixed interlacings are, in general, not significant within the usual range of r, around unity. Therefore, Eq. (6.73) can be used as an approximation of $\bar{B}_{ij}$ for such r values when n_g and n_m are numbers divisible by each other in both directions.

6.9.2.2 *Iso-stress*

As another method of estimating the bounds of elastic moduli the assumption of iso-stress is made. Derivations similar to that of Eq. (6.69) can be performed to obtain the average strain expression of the hybrid fabric composite. The average elastic constants are then given by

$$(\bar{A}'_{ij}, \bar{B}'_{ij}, \bar{D}'_{ij}) = \frac{1}{l_f l_w} \int_0^{l_w} \int_0^{l_f} (A'^{\xi\eta}_{ij}, B'^{\xi\eta}_{ij}, D'^{\xi\eta}_{ij}) \, dx \, dy \tag{6.74}$$

By replacing $A_{ij}^{\xi\eta}$, $B_{ij}^{\xi\eta}$ and $D_{ij}^{\xi\eta}$ in Eqs. (6.71)–(6.73) by $A'^{\xi\eta}_{ij}$, $B'^{\xi\eta}_{ij}$ and $D'^{\xi\eta}_{ij}$, explicit expressions of Eq. (6.74) can be obtained. These are upper bounds for the composite compliance constants; they can be inverted to obtain the lower bounds for the stiffness constants.

6.9.3 *One-dimensional approximation*

The approximate solution presented below is based upon a combination of the series model of Ishikawa (1981) for non-hybrid fabric composites and the mechanics of materials approach for unidirectional composites. The basic assumptions are that the hybrid fabric composite can be divided into repeating regions in the form of one-dimensional strips, and the equilibrium and compatibility conditions are not exactly satisfied. Figure 6.36 shows that the hybrid fabric composite is divided into strips along the filling and warp directions. It is then assumed that the stress resultant (N) is uniform in each strip.

The division of the strips is made according to the elastic moduli under consideration; along the filling (x) direction for A_{11}, B_{11}, D_{11}, A'_{11}, B'_{11} and D'_{11} and along the warp (y) direction for A_{22}, B_{22}, D_{22}, A'_{22}, B'_{22} and D'_{22}. Either the x or the y direction is admissible for determination of all the other non-zero constants.

Evidently the average strain in an α yarn is different from that of a β yarn. The one-dimensional average strain for the α yarn, for instance, can be written by considering the stress and moment resultants in the x direction only:

$$\bar{\varepsilon}^{o\alpha}_{xx} = \frac{1}{l_f}\int_0^{l_f} \varepsilon^{o}_{xx}\,dx$$

$$= \frac{1}{l_f}\left[N_x \int_0^{l_f} A'^{\xi\eta}_{11}\,dx + M_x \int_0^{l_f} B'^{\xi\eta}_{11}\,dx\right] \tag{6.75}$$

Fig. 6.36. One-dimensional model of hybrid fabric composites. (After Ishikawa and Chou 1982a.)

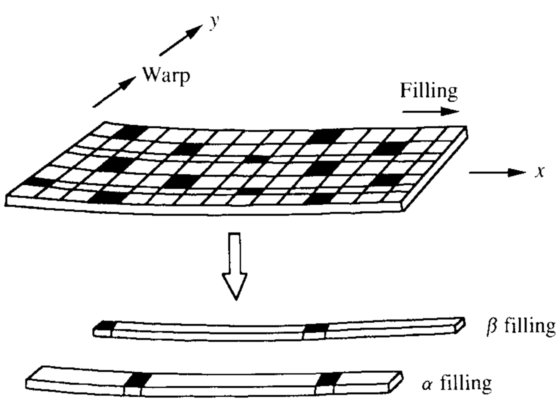

where ξ and η stand for α and β. For the case where n_g and n_{fm} are numbers not divisible by each other in the filling direction, the following expressions for the averaged compliances are obtained for the α-filling yarns:

$$\bar{A}'^{\alpha}_{ij} = \frac{1}{(n^{\alpha}_{fm} + n^{\beta}_{fm}r)} (n^{\alpha}_{fm} A'^{\alpha\alpha}_{ij} + n^{\beta}_{fm} A'^{\alpha\beta}_{ij} r)$$

$$\bar{B}'^{\alpha}_{ij} = \frac{(n_g - 2)}{n_g} \frac{1}{(n^{\alpha}_{fm} + n^{\beta}_{fm}r)} (n^{\alpha}_{fm} B'^{\alpha\alpha}_{ij} + n^{\beta}_{fm} B'^{\alpha\beta}_{ij} r) \tag{6.76}$$

$$\bar{D}'^{\alpha}_{ij} = \frac{1}{(n^{\alpha}_{fm} + n^{\beta}_{fm}r)} (n^{\alpha}_{fm} D'^{\alpha\alpha}_{ij} + n^{\beta}_{fm} D'^{\alpha\beta}_{ij} r)$$

Naturally, expressions of $\bar{A}^{\alpha}_{ij}$, $\bar{B}^{\alpha}_{ij}$ and $\bar{D}^{\alpha}_{ij}$ for the α-filling yarns can be obtained by inverting $\bar{A}'^{\alpha}_{ij}$, $\bar{B}'^{\alpha}_{ij}$ and $\bar{D}'^{\alpha}_{ij}$ of Eqs. (6.76). A similar procedure can be applied to the β-filling yarns.

Finally, if the average strain and curvature in the α-yarns ($\bar{\varepsilon}^{\alpha}$ and $\bar{\kappa}^{\alpha}$) are not very much different from those in the β-yarn, it is not unreasonable to approximate the entire composite plate with a uniform strain field. Thus, the stiffness constants can be obtained from a volume average. For example,

$$\bar{A}_{11} = \frac{1}{(n^{\alpha}_{wm} + n^{\beta}_{wm}r)} (n^{\alpha}_{wm} \bar{A}^{\alpha}_{11} + n^{\beta}_{wm} \bar{A}^{\beta}_{11} r) \tag{6.77}$$

6.9.4 *Numerical results*

Consider the numerical example for the case of a carbon/ Kevlar fabric in an epoxy matrix. The basic elastic properties of the constituent unidirectional laminae used in this idealized mosaic model are given in Table 6.2. The fiber volume fraction is chosen to be 65% in order to match that of the experimental systems.

Figure 6.37 shows the relationship between $\bar{A}_{11}/h$ and relative fiber volume fraction for 'balanced fabrics' where $A_{11} = A_{22}$. The carbon and Kevlar yarns are designated as α and β yarns, respectively. Fabric parameters are chosen so as to coincide with those of Zweben and Norman (1976): $n_g = 8$, $n_{fm} = 4$ and $n_{wm} = 4$, while n^{α}_{fm}, n^{β}_{fm}, n^{α}_{wm}, and n^{β}_{wm} vary from 0 to 4. The numbers in parentheses correspond to values of n^{α}_{fm}, n^{β}_{fm}, n^{α}_{wm}, and n^{β}_{wm}. The ratio of the yarn width, r, varies from zero to infinity as the relative fiber volume fraction changes. Since n_g and n_m in this example are numbers divisible by each other, the lower bound predictions are affected by the weaving patterns. Only the lower bound for the case (3, 1; 3, 1) is shown for the full range of relative fiber volume fractions. Also, only homogeneous interlacing types are considered in Fig. 6.37. The upper bounds are identical to one another for these three weaving patterns and are shown by a straight line similar to the predictions of the rule-of-mixtures. The circles and triangles represent the experimental results of Zweben and Norman for carbon/Kevlar hybrid fabrics and laminates composed of unidirectional laminae of the parent components. The fabrics used in the experiments are equivalent to, in the present terminology, the categories of (3, 1; 3, 1) and (2, 2; 2, 2). The relative yarn width is close to $r = 1$ and the interlacing pattern is of the homogeneous type. These results fall in between the bound predictions.

The effect of fabric geometrical patterns of the parent composites on the bound prediction is worth examining. The bound prediction of Kevlar/epoxy is represented in Fig. 6.37 by either $n^{\alpha}_{\mathrm{fm}} = n^{\alpha}_{\mathrm{wm}} = 0$ or $r = C_{\beta}/C_{\alpha} \to \infty$. Similarly, the carbon/epoxy system corresponds

Fig. 6.37. $\bar{A}_{11}/h$ vs. relative fiber volume fraction. h denotes specimen thickness; UB, upper bound; LB, lower bound. Experimental results of Zweben and Norman (1976); (●) fabric; (▲) laminate. (After Ishikawa and Chou 1982a.)

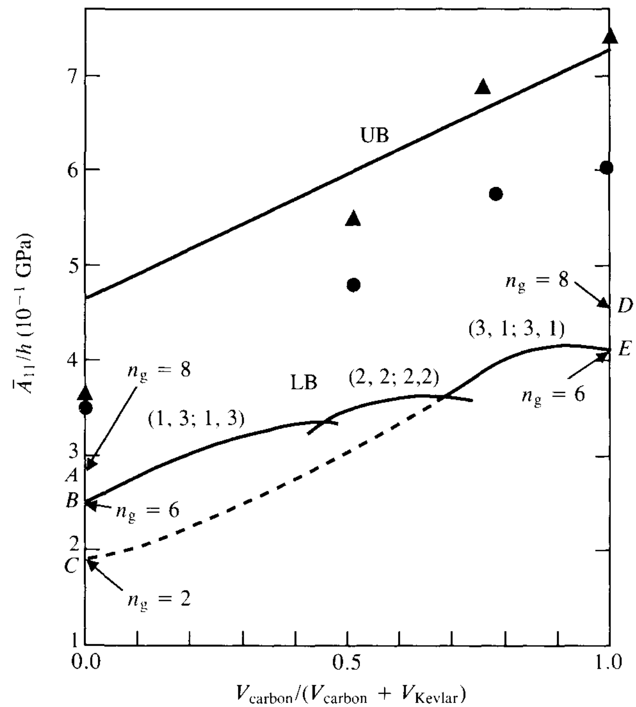

to the case of either $n^{\beta}_{\mathrm{fm}} = n^{\beta}_{\mathrm{wm}} = 0$ or $r = 0$. The lower bound predictions based on different combinations of n_{g} and n_{m} yield different results. Point A in Fig. 6.37 indicates the combination $n_{\mathrm{g}} = 8$ and $n^{\alpha}_{\mathrm{fm}} = n^{\alpha}_{\mathrm{wm}} = 0$. Point B is for the limiting case of $n_{\mathrm{g}} = 8$, (1, 3; 1, 3) and for $r \to \infty$; this case is equivalent to $n_{\mathrm{g}} = 6$ and $n^{\alpha}_{\mathrm{fm}} = n^{\alpha}_{\mathrm{wm}} = 0$. Point C is obtained from the case of $n_{\mathrm{g}} = 8$, (3, 1; 3, 1) and $r \to \infty$. The same weaving pattern can be achieved for $n_{\mathrm{g}} = 2$ and $n^{\alpha}_{\mathrm{fm}} = 0$. Discussions similar to the above can be made for the case of the carbon/epoxy system. Point D is for $n_{\mathrm{g}} = 8$ and $n^{\beta}_{\mathrm{fm}} = n^{\beta}_{\mathrm{wm}} = 0$. Point E is for $n_{\mathrm{g}} = 8$, (3, 1; 3, 1) and $r \to 0$; this is equivalent to $n_{\mathrm{g}} = 6$ and $n^{\beta}_{\mathrm{fm}} = n^{\beta}_{\mathrm{wm}} = 0$. The transition of the geometrical pattern from $n_{\mathrm{g}} = 8$ to either $n_{\mathrm{g}} = 2$ or 6 as r approaches the limiting values can be understood from Figs. 6.38(a) and (b), as well as Eqs. (6.71) and (6.73).

Fig. 6.38. The transition of fabric geometrical pattern as affected by r. (a) $n_{\mathrm{g}} = 8$ (3, 1; 3, 1) and $r = \frac{1}{4}$; this pattern becomes $n_{\mathrm{g}} = 6$ as $r \to 0$. (b) $n_{\mathrm{g}} = 8$, (3, 1; 3, 1) and $r = 8$; this pattern becomes $n_{\mathrm{g}} = 2$ as $r \to \infty$. (c) Homogeneous interlacing for $n_{\mathrm{g}} = 8$, (2, 2; 2, 2) and $r = \frac{1}{4}$; this pattern becomes $n_{\mathrm{g}} = 4$ as $r \to 0$, (d) Heterogeneous interlacing for $n_{\mathrm{g}} = 8$, (2, 2; 2, 2) and $r = \frac{1}{4}$; this pattern becomes a cross-ply laminate as $r \to 0$. (After Ishikawa and Chou 1982a.)

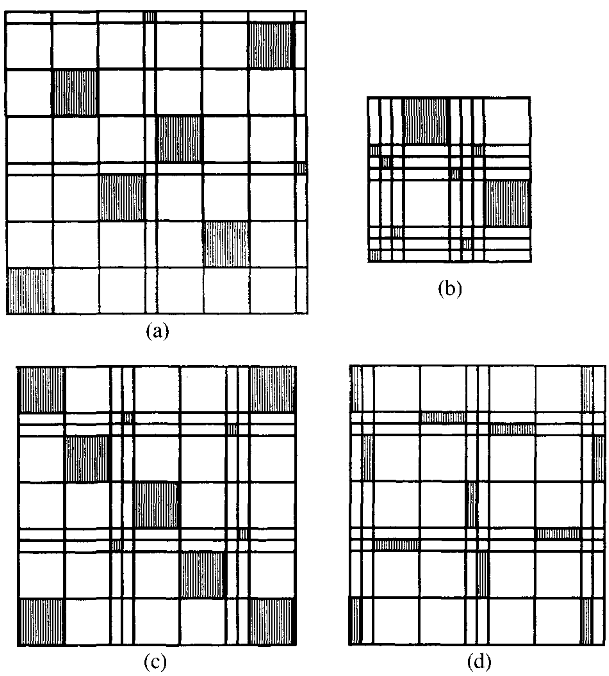

The relationship between $\bar{B}_{11}/h^2$ and the relative fiber volume fraction is demonstrated in Fig. 6.39 for $n_g = 8$ and $n_{fm} = n_{wm} = 4$. Results for both homogeneous and heterogeneous interlacings are shown. In the case of homogeneous interlacing, i.e. (1, 3; 1, 3), (2, 2; 2, 2) and (3, 1; 3, 1), the basic trends of the lower bounds are similar to the predictions shown in Fig. 6.37. However, the upper bound predictions in this case are also affected by the fabric parameters. In the case of heterogeneous interlacing (2, 2; 2, 2), both the upper and lower bound predictions tend to be very large values when $r = 0$ and $r \to \infty$. As a result, extremely large coupling effects are seen in these limiting cases.

6.10 Hybrid fabric composites: crimp and bridging models

Although the bounds for the elastic properties of hybrid fabric composites can be conveniently estimated by the mosaic model, the upper and lower bounds are rather far apart. An improved analysis based upon the 'crimp model' and 'bridging model' developed for non-hybrid fabric composites is described.

In the following analysis, we specify $n_g = 8$ and the fiber material repeating parameters (n^{α}_{fm}, n^{β}_{fm}; n^{α}_{wm}, n^{β}_{wm}) are of three types: (3,

Fig. 6.39. $\bar{B}_{11}/h^2$ vs. relative fiber volume fraction; —— upper and lower bound predictions for homogeneous interlacing; —·—·— upper and lower bound predictions for heterogeneous interlacing; ——— one-dimensional approximate solution. (After Ishikawa and Chou 1982a.)

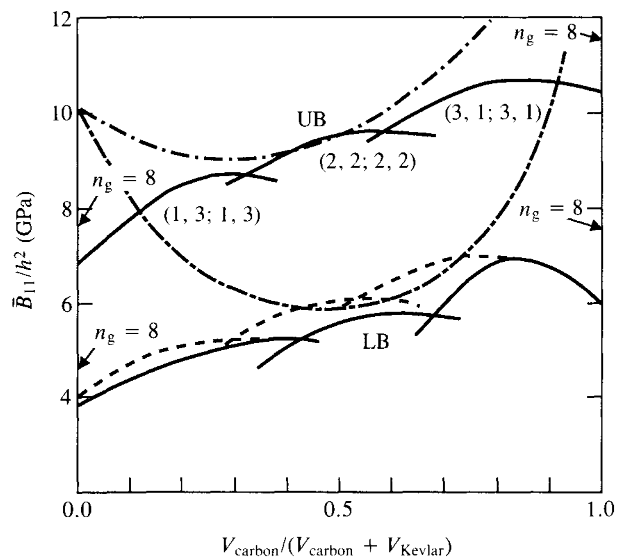

1; 3, 1), (1, 1; 1, 1) and (1, 3; 1, 3). Also, homogeneous interlacing is considered in the analysis. Furthermore, the calculation procedure for the system (1, 3; 1, 3) is the same as that for the system (3, 1; 3, 1) by interchanging the α and β materials. Therefore, only the systems of (3, 1; 3, 1) and (1, 1; 1, 1) need to be considered in the analysis.

6.10.1 *Crimp model*

The crimp model takes into account fiber continuity; sectional shapes of some typical interlacing regions are shown in Figs. 6.40(a) and (b). The sinusoidal type functions used in Section 6.5 for describing the undulation shapes are adopted here. For the

Fig. 6.40. Typical structures of interlaced regions of hybrid fabric composites; h denotes plate thickness and h_t indicates the total thickness of the yarns. (a) Filling: α material; warp: α or β material. (b) Filling: β material; warp: α or β material. (After Ishikawa and Chou 1983d.)

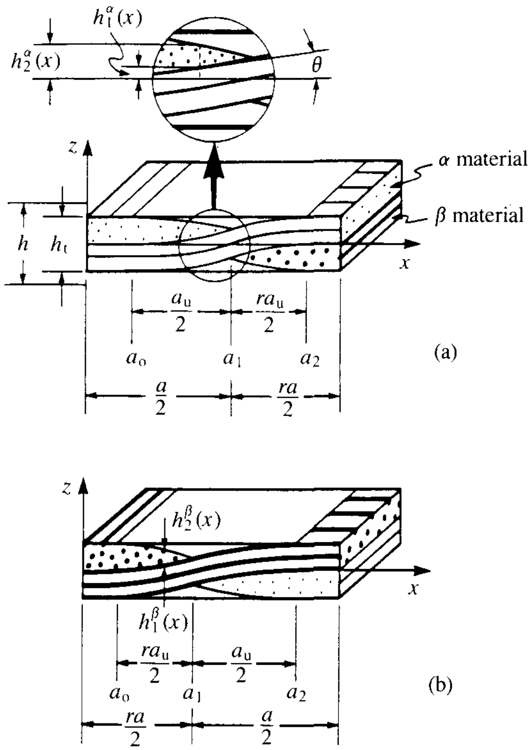

case where the filling yarn is composed of α material (Fig. 6.40a), the height of the filling yarn is given by

$$h_1^{\alpha}(x)=\begin{cases}0 & (0\le x\le a_{\mathrm{o}})\\ \left\{1+\sin\left[\left(x-\dfrac{a}{2}\right)\dfrac{\pi}{a_{\mathrm{u}}}\right]\right\}\dfrac{h_{\mathrm{t}}}{4} & (a_{\mathrm{o}}\le x\le a_1)\end{cases} \tag{6.78}$$

When the filling yarn is composed of β material, the height of the filling yarn is given by

$$h_1^{\beta}(x)=\begin{cases}0 & (0\le x\le ra_{\mathrm{o}})\\ \left\{1+\sin\left[\left(x-\dfrac{ra}{2}\right)\dfrac{\pi}{ra_{\mathrm{u}}}\right]\right\}\dfrac{h_{\mathrm{t}}}{4} & (ra_{\mathrm{o}}\le x\le ra_1)\end{cases} \tag{6.79}$$

where h_{t} denotes the total thickness of the yarns.

Corresponding to the cases of Eqs. (6.78) and (6.79), the heights of the warp yarns are given, respectively, by

$$h_2^{\alpha}(x)=\begin{cases}\dfrac{h_{\mathrm{t}}}{2} & (0\le x\le a_{\mathrm{o}})\\ \left\{1-\sin\left[\left(x-\dfrac{a}{2}\right)\dfrac{\pi}{a_{\mathrm{u}}}\right]\right\}\dfrac{h_{\mathrm{t}}}{4} & (a_{\mathrm{o}}\le x\le a_1)\end{cases} \tag{6.80}$$

$$h_2^{\beta}(x)=\begin{cases}\dfrac{h_{\mathrm{t}}}{2} & (0\le x\le ra_{\mathrm{o}})\\ \left\{1-\sin\left[\left(x-\dfrac{ra}{2}\right)\dfrac{\pi}{ra_{\mathrm{u}}}\right]\right\}\dfrac{h_{\mathrm{t}}}{4} & (ra_{\mathrm{o}}\le x\le ra_1)\end{cases} \tag{6.81}$$

It should be noted that Eqs. (6.78)–(6.81) are written for the portion of the undulated region where the filling yarn is beneath the warp yarn.

A key assumption made in the fiber crimp model (Ishikawa and Chou 1982b) is that the classical laminated plate theory is applicable to each infinitesimal slice of material of width dx. Then the local plate extensional stiffness coefficients for the portion where the filling yarn is composed of α material, are given by

$$A_{ij}^{\alpha\xi}(x) = Q_{ij}^{\mathrm{M}}\left(h - \frac{h_t}{2} + h_1^{\alpha}(x) - h_2^{\alpha}(x)\right)$$

$$+ Q_{ij}^{\mathrm{F}\alpha}(x)\frac{h_t}{2} + Q_{ij}^{\mathrm{W}\xi}(h_2^{\alpha}(x) - h_1^{\alpha}(x)) \tag{6.82}$$

where the superscripts F, W and M denote the filling yarn region, warp yarn region, and pure matrix material, respectively; ξ stands for α or β material, and h denotes the total laminate thickness, including the pure matrix layers. Furthermore, the first superscript of A_{ij} indicates the filling material and the second one the warp material. This convention is followed for all the stiffness and compliance constants throughout this analysis.

Likewise for the portion of the laminate in Fig. 6.40(b), where the filling yarn is composed of β material,

$$A_{ij}^{\beta\xi}(x) = Q_{ij}^{\mathrm{M}}\left(h - \frac{h_t}{2} + h_1^{\beta}(x) - h_2^{\beta}(x)\right)$$

$$+ Q_{ij}^{\mathrm{F}\beta}(x)\frac{h_t}{2} + Q_{ij}^{\mathrm{W}\xi}(h_2^{\beta}(x) - h_1^{\beta}(x)) \tag{6.83}$$

Similarly, expressions for $B_{ij}^{\alpha\xi}(x)$, $B_{ij}^{\beta\xi}(x)$, $D_{ij}^{\alpha\xi}(x)$ and $D_{ij}^{\beta\xi}(x)$ can also be obtained.

The local thermal deformation coefficients can be obtained by replacing Q_{ij} in Eq. (6.83) by $Q_{ij}\alpha_j$ (Eqs. (6.6) and (6.7)). For instance,

$$\tilde{A}_x^{\alpha\xi}(x) = q_x^{\mathrm{M}}\left(h - \frac{h_t}{2} + h_1^{\alpha}(x) - h_2^{\alpha}(x)\right)$$

$$+ q_x^{\mathrm{F}\alpha}(x)\frac{h_t}{2} + q_x^{\mathrm{W}\xi}(h_2^{\alpha}(x) - h_1^{\alpha}(x)) \tag{6.84}$$

where $q_x = Q_{11}\alpha_{xx} + Q_{12}\alpha_{yy} + Q_{16}\alpha_{xy}$. Explicit expressions of off-axis properties in the filling yarn region, $Q_{ij}^{\mathrm{F}\xi}(x)$, are given in Section 6.5. The local compliance constants $A_{ij}^{\prime\xi\eta}(x)$, $B_{ij}^{\prime\xi\eta}(x)$ and $D_{ij}^{\prime\xi\eta}(x)$ are obtained by inverting $A_{ij}^{\xi\eta}(x)$, $B_{ij}^{\xi\eta}(x)$ and $D_{ij}^{\xi\eta}$, where ξ and η indicate α or β material. Then, the thermal coefficients $\tilde{A}_i^{\prime\xi\eta}$ and $\tilde{B}_i^{\prime\xi\eta}$ can be obtained from Eq. (6.9).

Finally, consider again the one-dimensional idealized model of a hybrid laminate. The average extensional compliance for the portion containing α yarns is defined as

$$\bar{A}_{ij}^{\prime C\alpha\xi} = \frac{2}{a}\int_0^{a/2} A_{ij}^{\prime\alpha\xi}(x)\,\mathrm{d}x = \left(1 - \frac{a_{\mathrm{u}}}{2}\right)A_{ij}^{\prime\alpha\xi} + \frac{2}{a}\int_{a_{\mathrm{o}}}^{a_1} A_{ij}^{\prime\alpha\xi}(x)\,\mathrm{d}x \tag{6.85}$$

For the case of β filling yarns,

$$\bar{A}_{ij}^{\prime C\beta\xi} = \left(1 - \frac{a_{\mathrm{u}}}{a}\right)A_{ij}^{\prime\beta\xi} + \frac{2}{ra}\int_{ra_{\mathrm{o}}}^{ra_1} A_{ij}^{\prime\beta\xi}(x)\,\mathrm{d}x \tag{6.86}$$

The superscript 'C' in Eq. (6.85) signifies the fiber crimp model. The other averaged compliance constants $\bar{B}_{ij}^{\prime C\alpha\xi}$, $\bar{B}_{ij}^{\prime C\beta\xi}$, $\bar{D}_{ij}^{\prime C\alpha\xi}$ and $\bar{D}_{ij}^{\prime C\beta\xi}$ can be obtained in a similar manner. Expressions for the averaged in-plane thermal expansion coefficients can be obtained from Eqs. (6.85) and (6.86) by replacing $A_{ij}^{\prime}$ by the appropriate $\tilde{A}_i^{\prime}$. Also, the thermal bending coefficients can be easily obtained. However, it should be noted that $\bar{B}_{ij}^{\prime C\xi\eta}$ and $\bar{\tilde{B}}_i^{\prime C\xi\eta}$ do not vanish when the integrations in Eqs. (6.85) and (6.86) are carried out over the entire length of $a(1+r)/2$ (Fig. 6.40), unlike the cases of non-hybrid fabrics. This fact is caused by the difference in yarn width and properties of the constituent fibers of the fabric. Finally, the averaged stiffness constants $\bar{A}_{ij}^{C\xi\eta}$, $\bar{B}_{ij}^{C\xi\eta}$ and $\bar{D}_{ij}^{C\xi\eta}$ can be obtained by inverting these averaged compliance constants. Then the averaged thermal constants $\bar{\tilde{A}}_i^{C\xi\eta}$ and $\bar{\tilde{B}}_i^{C\xi\eta}$ are obtained from the inverted form of Eq. (6.9). It should be noted that the thermoelastic constants derived here are based upon the definitions of $h_1(x)$ and $h_2(x)$ given in Eqs. (6.78)–(6.81), i.e. the filling yarn is situated beneath the warp yarn. Thus, the coupling stiffness constants for the right-hand portions of Figs. 6.40(a) and (b) for instance, are denoted by $-\bar{B}_{ij}^{C\alpha\beta}$ and $-\bar{B}_{ij}^{C\beta\alpha}$, respectively.

6.10.2 *Bridging model*

The case of fabrics with $n_{\mathrm{g}} = 8$, $(n_{\mathrm{fm}}^{\alpha}, n_{\mathrm{fm}}^{\beta}; n_{\mathrm{wm}}^{\alpha}, n_{\mathrm{wm}}^{\beta}) = (3, 1; 3, 1)$ and homogeneous interlacing pattern is considered first. A possible shape of the minimum repeating unit is indicated in Fig. 6.41 as the area *ABCD*. The three-dimensional view of this repeating unit showing the interlaced configurations of the α and β yarns is given in Fig. 6.42, which consists of five regions R_1, R_2, R_3, R_4 and R_5, arranged in series along the loading direction. However, other choices for the division in regions are possible. It is assumed in the following analysis that the resultant force in the loading direction of every region is identical.

To exemplify the analysis of the bridging model, region R_2 is considered. Region R_2 consists of four sub-regions labeled R_2^1, R_2^2, R_2^3 and R_2^4 (see Fig. 6.43). By assuming an iso-strain condition for the sub-region, the average compliance constant of each region can be found. Then, the averaged stiffness constants of each sub-region are obtained by inverting the corresponding compliance constants. On the basis of the assumption of iso-strain, the average stiffness of the entire region R_2 can be determined. The elastic constants of the other regions can also be determined following this procedure.

For the fabric composite of Fig. 6.42, it is assumed that each

Fig. 6.41. A hybrid fabric with homogeneous interlacing, for $n_g = 8$, $n_{fm} = n_{wm} = 4$; α and β indicate two types of yarn material; *ABCD* and *EFGD* denote two choices of repeating units. (After Ishikawa and Chou 1983d.)

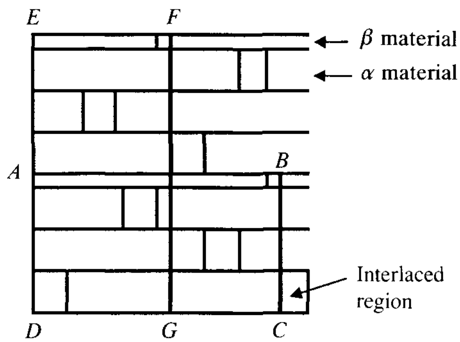

Fig. 6.42. A bridging model for $n_g = 8$ and the (3, 1; 3,1) case (region *ABCD* of Fig. 6.41). (After Ishikawa and Chou 1983d.)

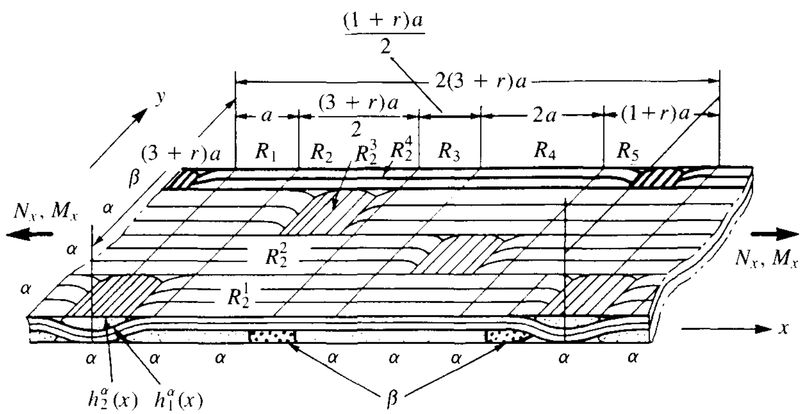

region, R_1, R_2, R_3, R_4, or R_5 carries the same load N_x. Thus, the compliance constants of the entire composite can be regarded as the volume average of the compliances of the individual regions. Then, the inversion of the compliance constants gives the stiffness coefficients of the entire composite unit cell, $\bar{A}_{ij}$, $\bar{B}_{ij}$ and $\bar{D}_{ij}$. The basic idea of the analysis briefly outlined above is identical to that of the 'bridging model' of Section 6.6 in which only non-hybrid composites are considered. The details of the derivations of elastic and thermal deformation constants can be found in Ishikawa and Chou (1983d).

Both regions *ABCD* and *EFGD* of Fig. 6.41 can be treated as repeating regions for the entire fabric composite. A three-dimensional view of region *EFGD* can also be found in Ishikawa and Chou (1983d). As to the case of the (1, 3; 1, 3) material combination, the thermoelastic constants can be obtained from the above procedure by simply interchanging the α and β materials. Ishikawa and Chou (1983d) have also examined the case of a fabric of $n_g = 8$ with homogeneous interlacing and material repeating parameters (2, 2; 2, 2). The cases of (3, 1; 3, 1), (1, 3; 1, 3) and (2, 2; 2, 2) give all possible fiber material combinations for homogenous interlacing in hybrid fabrics with the given fabric parameters.

6.10.3 *Numerical results and summary of thermoelastic properties*

Numerical work has been performed to examine the thermoelastic properties of a carbon/Kevlar/epoxy hybrid fabric composite. The basic material properties of unidirectional laminae of carbon/epoxy and Kevlar/epoxy are given in Table 6.2. The fiber volume fraction of all the unidirectional laminae is assumed to be

Fig. 6.43. Detailed view of region R_2 in Fig. 6.42. (After Ishikawa and Chou 1983d.)

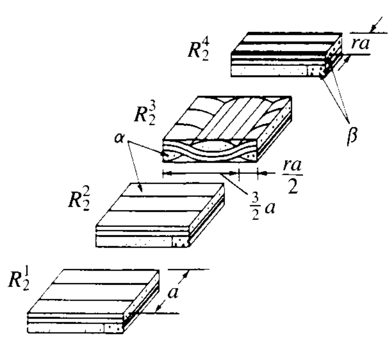

65%, which is slightly higher than the total fiber volume fraction of the fabric composite due to the presence of pure matrix layers.

Figure 6.44 shows the predictions of the extensional stiffness of the bridging model as well as those from the bound approach (Fig. 6.37) of Ishikawa and Chou (1982a) for a carbon/Kevlar/epoxy system of $n_g = 8$. Three different material repeating parameters are presented and the theoretical curves are obtained by changing r, the yarn width ratio of α and β materials. Because values of r far from unity are impractical, the curves in Fig. 6.44 are truncated. The predictions based upon the bridging concept fall in between the upper and lower bounds and compare very favorably with the experimental data of Zweben and Norman (1976).

The following is a summary of the analysis of thermoelastic properties of hybrid woven fabric composites:

(1) The structural characteristics of woven hybrid fabrics have been identified by the material parameter n_m (n_{fm} and n_{wm}) as well as the geometrical parameter n_g (n_{fg} and n_{wg}). If the

Fig. 6.44. $\bar{A}_{11}/h$ vs. relative fiber volume fraction of carbon/Kevlar/epoxy composites with $n_g = 8$; ——— bound theory; —— bridging model; (● and ▲ experimental data for fabric and cross-ply laminate composites, respectively; ($h = h_t$, $h/a = 0.4$). (After Ishikawa and Chou 1983d.)

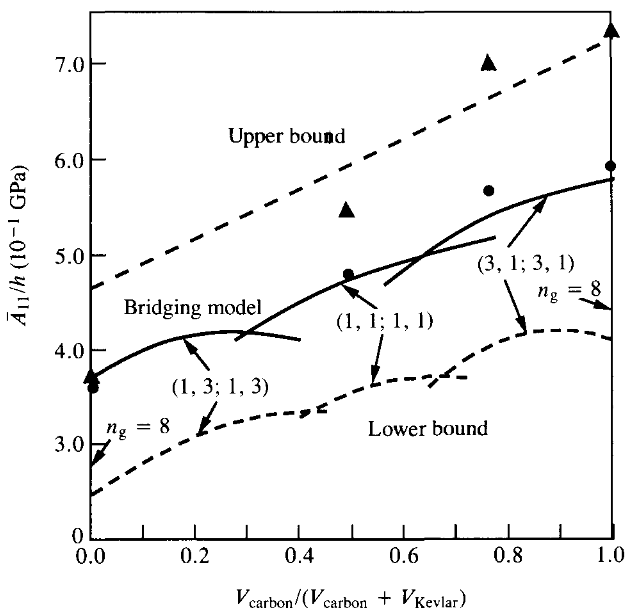

n_g and n_m of a fabric are numbers not divisible by each other in one or both directions (filling and warp) there is a unique interlacing pattern. There is more than one type of interlacing pattern if n_g and n_m are numbers divisible by each other in both directions.

(2) In the analysis of the mosaic model, the fabric composite is regarded as an assemblage of asymmetrical cross-ply laminates. Upper and lower bounds for the elastic stiffness and compliance of hybrid composites have been obtained assuming iso-strain and iso-stress, respectively. The influence of fabric parameters on elastic properties can be assessed using this model.

(3) The magnitude of the coupling terms of B_{ij} and B'_{ij} depends on whether n_g and n_m are numbers divisible by each other. In the case where n_g and n_m are numbers divisible by each other in both the warp and the filling directions, the upper and lower bounds of B_{ij} and the lower bounds of A_{ij} and D_{ij} are influenced by the interlacing types.

(4) The transition of n_g from one value to another occurs as the ratio of yarn width of the component fibers approaches zero or infinity. In such extreme cases, the magnitude of the coupling terms becomes very large, especially for heterogeneous interlacing. The distinct interlacing types for given n_g and n_m, however, render nearly identical solutions for the bounds when the yarn width ratio is around unity.

(5) The one-dimensional fiber undulation or crimp concept has been modified to treat the interlacing of two different types of fibers, and it has been incorporated into a general 'bridging model' for predicting thermoelastic properties of hybrid fabric composites.

(6) The predicted values of the axial elastic stiffness constant are insensitive to the choice of a repeating unit of the fabric material.

6.11 Triaxial woven fabric composites

6.11.1 *Geometrical characteristics*

Biaxial woven fabrics exhibit relatively low elastic moduli or low resistance to extension when deformed along the bias direction (45° to warp and filling) as compared with deformation in the warp and filling directions. A triaxial woven fabric (Doweave fabric), is composed of three sets of yarns (two sets of warp yarns and one set of filling yarn), which intersect and interlace with one another at 60° angles as shown in Fig. 6.45.

For the purpose of identification, the warp yarns are called 'one o'clock' and 'eleven o'clock' warps. The filling yarn is horizontal and is interwoven with the warp yarns in different sequences depending on the fabric style. The geometry of the fabric can vary from a very open but stable construction, such as basic weave, and stuffed basic weave (which has additional yarns in the filling direction), to a tightly packed construction, such as the bi-plane weave. Figure 6.46(a) shows a schematic diagram of the stuffed basic weave. The bi-plane weave is quite similar to the basket weave of biaxial woven fabrics. As shown in Fig. 6.46(b), the filling yarns in a bi-plane weave are woven both over and under two sets of warp yarns to form a closed construction.

With the load bearing yarns arranged in three instead of two directions, the triaxial woven fabrics yield more isotropic responses to both tensile and shear deformations, offering an alternative to the inherent structural weakness of conventional biaxial fabrics. The ability of the triaxial woven fabrics to maintain structural integrity

Fig. 6.45. Triaxial woven fabric. (After Yang and Chou 1989.)

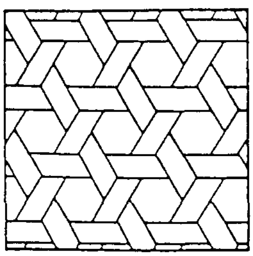

Fig. 6.46. The geometries of (a) stuffed basic triaxial woven fabric and (b) bi-plane weave triaxial woven fabric. (After Yang and Chou 1989.)

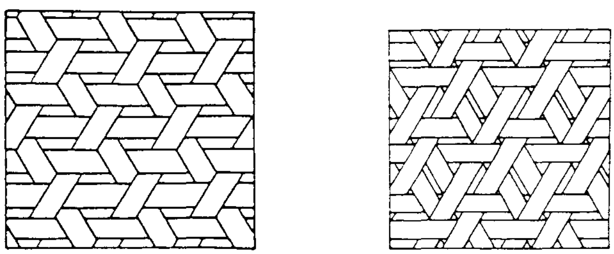

(a) (b)

even with a very open construction is quite unique among textile structures.

The filling yarn of a triaxial woven fabric may be composed of bundles of different size and material from the warp yarns. Therefore, hybrid fiber constructions are available for triaxial woven fabrics as for biaxial woven fabrics. Also, by proper selection of material combinations, yarn sizes and fabric weaving patterns, a wide range of geometrical and mechanical properties can be engineered in triaxial woven fabrics.

Although considerable effort has been made to investigate the mechanical behavior of triaxial woven fabrics (see Dow 1969; Dow and Tranfield 1970; Skelton 1971; Scardino and Ko 1981; Schwartz, Fornes and Mohamed 1982; Schwartz 1984), the properties of composites reinforced with triaxial woven fabrics have not been adequately evaluated. Dow (1982) developed an analytical method; the geometrical model used for the calculation of the fiber volume fraction and elastic properties of the triaxial woven fabric composite resembles the crimp model of Fig. 6.17. The undulated yarns are divided into segments and each of these segments is treated as an off-axis short-fiber composite lamina. The elastic properties of the triaxial fabric composite unit cell are calculated by averaging the contribution from each of the short-fiber composites.

In the following, a more refined analytical model is developed to predict the thermoelastic properties of triaxial fabric composites. An outline of the methodology of analysis is given first. It is then extended to biaxial, non-orthogonal woven fabric composites. Numerical results of the thermoelastic properties are presented as a function of the fabric construction parameters. The contents of Sections 6.11.2 and 6.11.3 are excerpted from Yang and Chou (1989).

6.11.2 *Analysis of thermoelastic behavior*

For the purpose of analyzing the thermoelastic constitutive relations of triaxial woven fabric composites, a unit cell of basic triaxial weave is identified, as shown in Fig. 6.47, which contains three impregnated yarn bundles oriented in space and interstitial matrix regions. Repeating the unit cell in the fabric plane obviously reproduces the complete triaxial woven structure. This methodology can easily be extended to treat other types of weaving patterns.

The concept of the 'crimp model' (Ishikawa and Chou 1982b) is extended to the following analysis. In this model, each impregnated yarn bundle is further idealized as an undulated unidirectional lamina as shown in Fig. 6.48. The geometrical configuration of each undulated lamina can be simulated as follows. First, consider the lamina of filling yarns. The upper boundary for the undulated configuration is given by (Fig. 6.48a)

$$H(x_1) = \left[1 + \sin\frac{\pi x_1}{l_1}\right]\frac{H_t}{2} \qquad (0 \leq x \leq 2l_1) \tag{6.87}$$

Here, x_1 coincides with the x axis and H_t is the thickness of the undulated lamina.

Next, the form of fiber undulation in the one o'clock warp lamina as shown in Fig. 6.48(b) is

$$H(x_2) = \left[1 - \sin\left(x_2 - \frac{l_2}{2}\right)\frac{\pi}{l_2}\right]\frac{H_t}{2} \qquad (0 \leq x_2 \leq 2l_2) \tag{6.88}$$

Here, x_2 is in the direction of 60° from the x axis. Similarly, in the eleven o'clock warp lamina (Fig. 6.48c), the form of fiber undulation is

$$H(x_3) = \left[1 + \sin\left(x_3 - \frac{l_3}{2}\right)\frac{\pi}{l_3}\right]\frac{H_t}{2} \qquad (0 \leq x_3 \leq 2l_3) \tag{6.89}$$

where x_3 is in the direction of $-60°$ from the x axis.

The crimp in the undulated laminae reduces the composite stiffness as compared with that of straight reinforcements. The local off-axis angle of each undulated lamina along the x_1, x_2 and x_3

Fig. 6.47. Unit cell structure of the basic triaxial woven fabric composite. (After Yang and Chou 1989.)

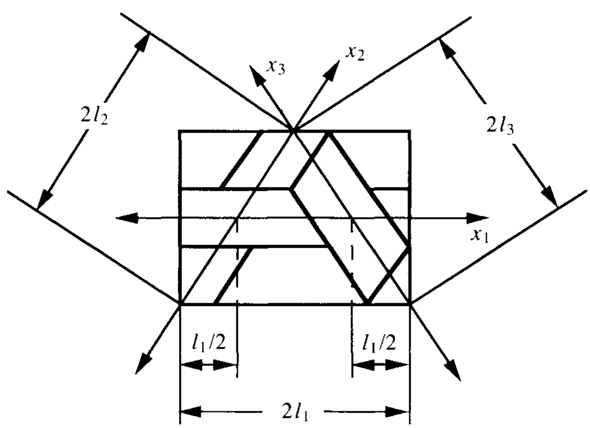

directions can be obtained by

$$\theta = \tan^{-1}\frac{\mathrm{d}H(x_i)}{\mathrm{d}x_i} \qquad (i = 1,\ 2 \text{ or } 3) \tag{6.90}$$

The effective thermoelastic properties of each undulated lamina can be derived through the following procedures. First, the undulated lamina can be regarded as an assemblage of many small pieces

Fig. 6.48. Geometrical configurations of undulated filling and warp laminae. (After Yang and Chou 1989.)

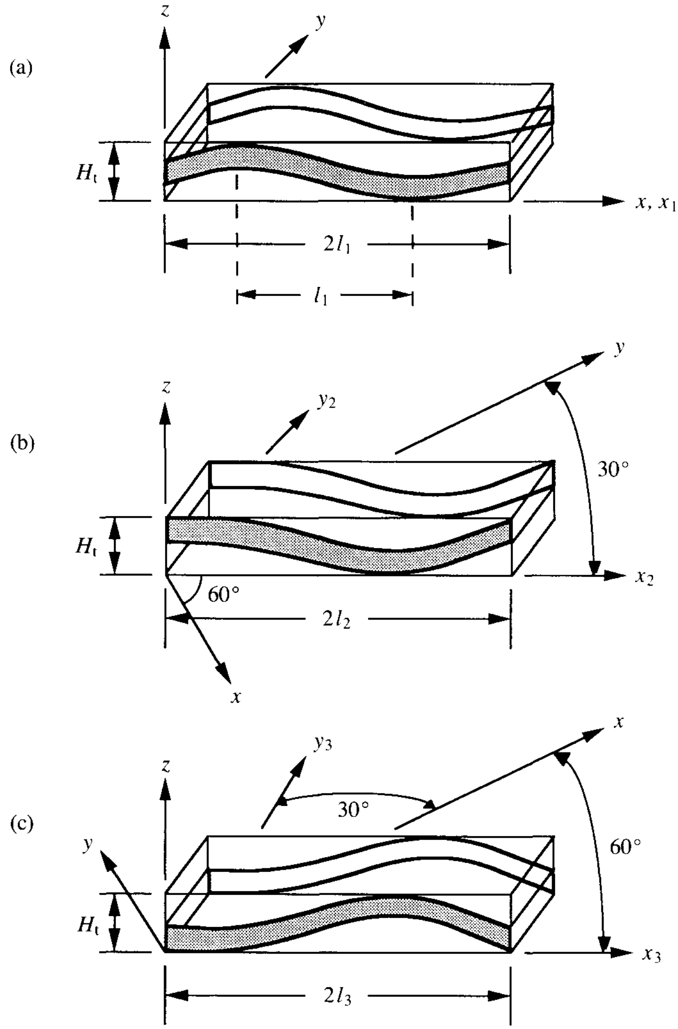

of unidirectional lamina. Each of these segments is uniquely characterized by an off-axis angle as defined in Eq. (6.90). The reduced effective thermoelastic properties in the x direction for the filling lamina are the same as those given in Eqs. (6.24) and (6.51).

By assuming that each of these short composite laminar segments is subjected to the same stress, the strain in each segment is

$$\begin{aligned}\varepsilon_{xx}(\theta) &= \frac{\sigma_{xx}}{E_{xx}(\theta)}\\ \varepsilon_{yy}(\theta) &= -\nu_{xy}(\theta)\frac{\sigma_{xx}}{E_{xx}(\theta)}\end{aligned} \tag{6.91}$$

The normal strains averaged over the length $2l_1$ along the x direction are

$$\begin{aligned}\bar{\varepsilon}_{xx} &= \frac{1}{2l_1}\int_0^{2l_1} \varepsilon_{xx}(\theta)\,\mathrm{d}x\\ \bar{\varepsilon}_{yy} &= \frac{1}{2l_1}\int_0^{2l_1} \varepsilon_{yy}(\theta)\,\mathrm{d}x\end{aligned} \tag{6.92}$$

The average longitudinal Young's modulus, transverse Young's modulus and Poisson's ratio can be obtained as

$$E_{xx} = \frac{\sigma_{xx}}{\bar{\varepsilon}_{xx}} \qquad E_{yy} = E_{22} \qquad \nu_{xy} = -\frac{\bar{\varepsilon}_{yy}}{\bar{\varepsilon}_{xx}} \tag{6.93}$$

The average in-plane shear modulus can be obtained by assuming that each of these segments is subjected to the same shear strain. Thus,

$$G_{xy} = \frac{1}{2l_1}\int_0^{2l_1} G_{xy}(\theta)\,\mathrm{d}x \tag{6.94}$$

Thus, the averaged stiffness constants of the undulated filling lamina can be obtained by using Eq. (6.10).

The average thermal expansion coefficients along the x and y directions are defined as

$$\begin{aligned}\alpha_{xx} &= \frac{1}{2l_1}\int_0^{2l_1} (\alpha_{11}\cos^2\theta + \alpha_{22}\sin^2\theta)\,\mathrm{d}\theta\\ \alpha_{yy} &= \frac{1}{2l_1}\int_0^{2l_1} \alpha_{yy}(\theta)\,\mathrm{d}x = \alpha_{22}\\ \alpha_{xy} &= \frac{1}{2l_1}\int_0^{2l_1} \alpha_{xy}(\theta)\,\mathrm{d}x = 0\end{aligned} \tag{6.95}$$

The procedures outlined above can be applied to obtain the effective thermoelastic properties of both one o'clock and eleven o'clock warp laminae along the x_2 and x_3 directions, respectively. However, the x_2 and x_3 directions are, respectively, at 60° and −60° off-axis orientations with respect to the x axis. The effective properties of these two warp laminae in the x–y plane can be obtained by the following coordinate transformation (Jones 1975):

$$\begin{aligned}
\bar{Q}_{11} &= Q_{11}\cos^4\phi + 2(Q_{12}+2Q_{66})\sin^2\phi\cos^2\phi \\
&\quad + Q_{22}\sin^4\phi \\
\bar{Q}_{12} &= (Q_{11}+Q_{22}-4Q_{66})\sin^2\phi\cos^2\phi \\
&\quad + Q_{12}(\sin^4\phi+\cos^4\phi) \\
\bar{Q}_{22} &= Q_{11}\sin^4\phi + 2(Q_{12}+2Q_{66})\sin^2\phi\cos^2\phi + Q_{22}\cos^4\phi \\
\bar{Q}_{16} &= (Q_{11}-Q_{12}-2Q_{66})\sin\phi\cos^3\phi \\
&\quad + (Q_{12}-Q_{22}+2Q_{66})\sin^3\phi\cos\phi \\
\bar{Q}_{26} &= (Q_{11}-Q_{12}-2Q_{66})\sin^3\phi\cos\phi \\
&\quad + (Q_{12}-Q_{22}+2Q_{66})\sin\phi\cos^3\phi \\
\bar{Q}_{66} &= (Q_{11}-Q_{22}-2Q_{12}-2Q_{66})\sin^2\phi\cos^2\phi \\
&\quad + Q_{66}(\sin^4\phi+\cos^4\phi) \\
\bar{\alpha}_{xx} &= \alpha_{xx}\cos^2\phi + \alpha_{yy}\sin^2\phi \\
\bar{\alpha}_{yy} &= \alpha_{xx}\sin^2\phi + \alpha_{yy}\cos^2\phi \\
\bar{\alpha}_{xy} &= (\alpha_{xx}-\alpha_{yy})\sin\phi\cos\phi \\
\bar{q}_x &= \bar{Q}_{11}\bar{\alpha}_{xx} + \bar{Q}_{12}\bar{\alpha}_{yy} + \bar{Q}_{16}\bar{\alpha}_{xy} \\
\bar{q}_y &= \bar{Q}_{12}\bar{\alpha}_{xx} + \bar{Q}_{22}\bar{\alpha}_{yy} + \bar{Q}_{26}\bar{\alpha}_{xy} \\
\bar{q}_{xy} &= \bar{Q}_{16}\bar{\alpha}_{xx} + \bar{Q}_{26}\bar{\alpha}_{yy} + \bar{Q}_{66}\bar{\alpha}_{xy}
\end{aligned} \tag{6.96}$$

Here, ϕ represents +60° and −60°, respectively, for one o'clock and eleven o'clock warp yarns.

Upon knowing the effective thermoelastic properties of each undulated lamina in the x–y plane, the composite properties can be derived under the assumption that each of these undulated composite laminae is subjected to the same strain along the x direction. Thus, the effective in-plane thermoelastic properties of the triaxial fabric composite unit cell are given as (Rosen, Chatterjee and

Kibler 1977)

$$
\begin{aligned}
Q_{ij}^* &= \sum_{n=1}^{3} V^{(n)} \bar{Q}_{ij}^{(n)} \\
q_x^* &= \sum_{n=1}^{3} V^{(n)} \bar{q}_x^{(n)} \\
q_y^* &= \sum_{n=1}^{3} V^{(n)} \bar{q}_y^{(n)} \\
q_{xy}^* &= \sum_{n=1}^{3} V^{(n)} \bar{q}_{xy}^{(n)}
\end{aligned}
\tag{6.97}
$$

where V is volume fraction and (n) denotes the yarns in the x_1, x_2 and x_3 directions. The thermal expansion coefficients of the triaxial woven fabric composite are found from

$$
\begin{aligned}
\alpha_{xx}^* &= S_{11}^* q_x^* + S_{12}^* q_y^* + S_{16}^* q_{xy}^* \\
\alpha_{yy}^* &= S_{12}^* q_x^* + S_{22}^* q_y^* + S_{26}^* q_{xy}^* \\
\alpha_{xy}^* &= S_{16}^* q_x^* + S_{26}^* q_y^* + S_{66}^* q_{xy}^*
\end{aligned}
\tag{6.98}
$$

Here, S_{ij}^* is the inversion of Q_{ij}^* of Eqs. (6.97).

By assuming that the yarns have a circular cross-section with diameter d, and $l_1 = l_2 = l_3 = l$ for the unit cell of Fig. 6.47, the highest fiber volume fraction that can be obtained for a basic triaxial weave is about 43%. For the yarn spacing/diameter ratios (l/d) of 2, 3, 4, 5 and 6, the fiber volume fraction (V_f) values are, respectively, 42.5, 24, 17.5, 14.2 and 11. Higher volume fractions can be obtained by changing the weave pattern to stuffed basic weave or bi-plane weave. As the l/d ratio increases, the fiber volume fraction decreases and the crimp can be minimized. Thus, the unit cell structure approaches a [0°/±60°] laminate composite with straight reinforcements.

Figures 6.49(a)–(c) demonstrate the variation of longitudinal Young's modulus, in-plane shear modulus and longitudinal thermal expansion coefficient of triaxial woven carbon fabric reinforced epoxy composites with yarn spacing/diameter ratios. The results of [0°/±60°] laminate composites as functions of fiber volume fraction can also be found in these figures. These results all indicate that as l/d increases, the difference in thermoelastic constants between woven structures and straight laminae is reduced as expected.

Even though the stiffness reduction of triaxial woven fabric composites as compared with [0°/±60°] laminates is quite severe when l/d is small, it is feasible to place additional laid-in yarns (non-crimp yarns) in the filling direction to enhance the axial properties as shown in Fig. 6.46(a). Furthermore, fiber hybridiza-

Fig. 6.49. Comparisons of the predicted thermoelastic properties of triaxial woven fabric composite (carbon/epoxy) and [0°/±60°] angle-ply laminate composite (carbon/epoxy) as functions of yarn spacing ratio (l/d). (a) Longitudinal Young's modulus. (b) In-plane shear modulus. (c) Longitudinal coefficient of thermal expansion (CTE). (After Yang and Chou, 1989.)

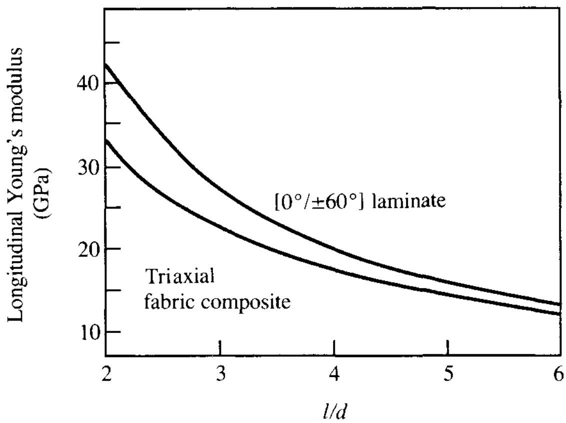

(a)

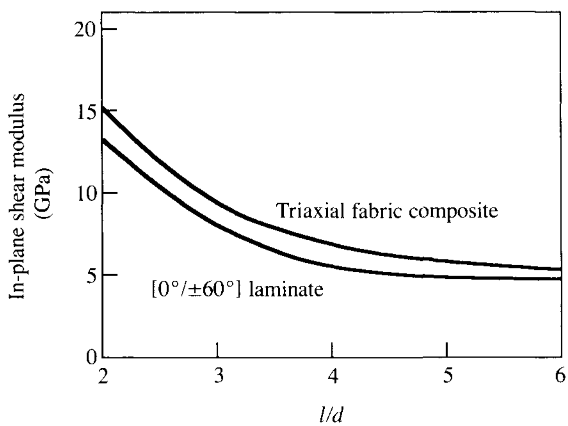

(b)

tion allows considerable design flexibility in meeting the requirements of high performance composites. Thus, by the proper selection of material combinations and fabric structural geometry, a wide range of mechanical properties can be engineered.

6.11.3 *Biaxial non-orthogonal woven fabric composites*

Biaxial non-orthogonal woven fabric composites can be produced by flat braiding, or they could occur in the fabrication of bi-axial orthogonal woven fabric composites. The flow of matrix material and the curvature of the mold surface could distort orthogonal yarns into non-orthogonal positions. The geometry of a non-orthogonal woven fabric is depicted in Fig. 6.50. It can be treated simply as a triaxial woven fabric without the filling yarn. Consequently, the methodology developed for the triaxial woven fabric composites can be readily applied. The composite unit cell is composed of two undulated laminae interlaced together at any angle, the magnitude of which depends upon the braiding pattern or the distortion of the fabric.

Figure 6.51 illustrates the variation of Young's modulus with the braiding angle or the angle of a biaxial non-orthogonal woven fabric composite. Yang and Chou (1989) have also shown that as 2θ decreases below the right angle, the thermal expansion coefficient increases along the y direction and decreases along the x direction; the in-plane shear modulus decreases with the decrease in the bias angle.

Fig. 6.49 (cont.).

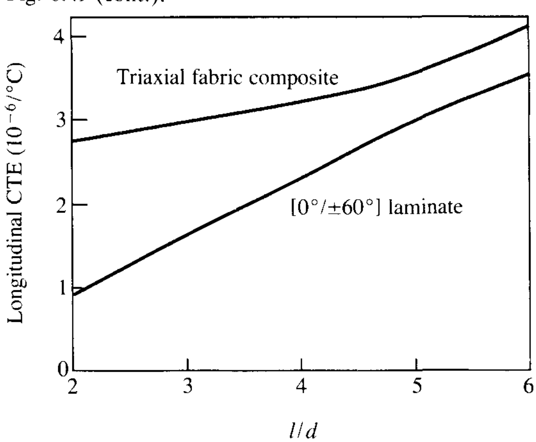

(c)

6.12 Nonlinear stress–strain behavior

The nonlinear stress–strain behavior of fabric composites due to transverse crackings initiated in warp yarns has been discussed in Section 6.7. Although transverse cracking can account for the nonlinearity at small strains, both the filling yarns and the matrix rich regions contribute to the overall nonlinear behavior of fabric composites.

Ishikawa and Chou (1983c) first adopted a one-dimensional (crimp) model to examine the material nonlinearities in the filling yarn and the pure matrix region. This approach is then extended to

Fig. 6.50. A non-orthogonal woven fabric composite and its unit cell for analysis. (After Yang and Chou 1989.)

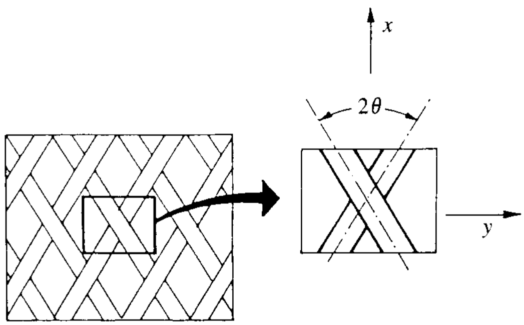

Fig. 6.51. The predicted longitudinal Young's modulus of non-orthogonal carbon fabric/epoxy composites as a function of bias angle ($V_f = 60\%$). (After Yang and Chou 1989.)

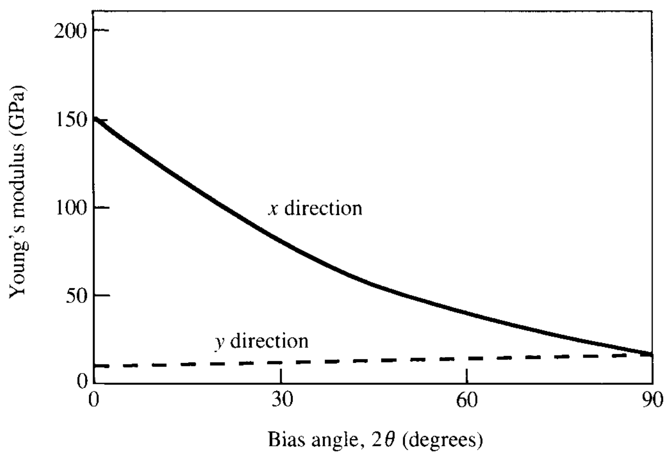

the bridging model for satin weave composites, and combined with the analysis of transverse matrix cracking to provide a more comprehensive description of the nonlinear elastic stress–strain behavior of fabric composites.

The essence of the treatment of Ishikawa and Chou can be understood by considering the filling yarn depicted in Fig. 6.17. Segments of this yarn are subjected to off-axis loading in the x–z plane due to fiber undulation. Thus, nonlinear shear deformation is induced in the filling yarn due to the axial load. Following Hahn and Tsai (1973), the nonlinear shear strain–stress relation is assumed to be

$$\varepsilon_{zx} = S_{55}\sigma_{zx} + S_{5555}(\sigma_{zx})^3 \tag{6.99}$$

Here, S_{55} and S_{5555} represent, respectively, the linear and nonlinear compliance constants. As to the nonlinear shear behavior of the matrix material under tensile loading, the constitutive relation is assumed to follow the same form as Eq. (6.99)

$$\varepsilon^{\mathrm{M}}_{xx} = S^{\mathrm{M}}_{11}\sigma^{\mathrm{M}}_{xx} + S^{\mathrm{M}}_{1111}(\sigma_{\mathrm{xx}})^3 \tag{6.100}$$

Ishikawa and Chou have performed a numerical analysis of the stress–strain relation for glass/polyimide. The basic properties of a unidirectional lamina are given in Table 6.2 and $S_{5555} = 37.0\ (1/\mathrm{GPa}^3)$. The major ambiguity of the analysis lies in the value of the nonlinear shear compliance, S_{5555}. Because of the lack of experimental data, an estimated value based upon the stress–strain curve for a glass/epoxy composite (Jones 1975) is used. The elastic properties of polyimide are $E = 4.31$ GPa and $\nu = 0.36$. The nonlinear extensional compliance $S^{\mathrm{M}}_{1111} = 9.88\ (1/\mathrm{GPa}^3)$ is also assumed to be the same as that of epoxy. Other assumptions are that $a = a_{\mathrm{u}} = 0.4$ mm, $h = h_{\mathrm{t}} = 0.244$ mm, and the bending-free state of deformation is valid.

Figure 6.52 indicates the numerical results of this nonlinear analysis (solid line) and the result from the consideration of transverse cracking only (dashed line) for the glass/polyimide composite. Both eight-harness satin ($n_{\mathrm{g}} = 8$) and plain weave ($n_{\mathrm{g}} = 2$) composites are indicated. The experimental stress–strain data of an eight-harness satin as indicated by the dots are included. The nonlinear analysis compares better with the experiment in the range of large strain than the results given by Ishikawa and Chou (1982b) for matrix cracking only. It is also observed that the contribution from shear nonlinearity increases at higher stress levels and for lower n_{g} values. Furthermore, the effect of nonlinearity on the composite behavior from the filling yarn far exceeds that from the pure matrix region.

6.13 Mechanical properties

The microstructure of two-dimensional woven fabric composites is responsible for some unique mechanical properties which are not found in their equivalent cross-ply laminates. The tension–tension fatigue behavior of woven fabric composites has been examined by Schulte, Reese and Chou (1987). In the following, the structure–property relationships are demonstrated in terms of the friction and wear behavior, and the notched strength of woven fabric composites.

6.13.1 *Friction and wear behavior*

When two surfaces interact, contact is made at their asperities. With the application of a normal load and relative motion, plastic deformation at the asperity contact zones occurs. As a result, adhesive junctions are formed which, under the influence of motion, tend to get fractured. Fracture occurs not at the original point of contact, but at some point within the softer material.

Fig. 6.52. Non-linear stress–strain relations of glass/polyimide fabric composites with $a = a_u = 0.4$ mm and $h = h_t = 0.244$ mm. (After Ishikawa and Chou 1983c.)

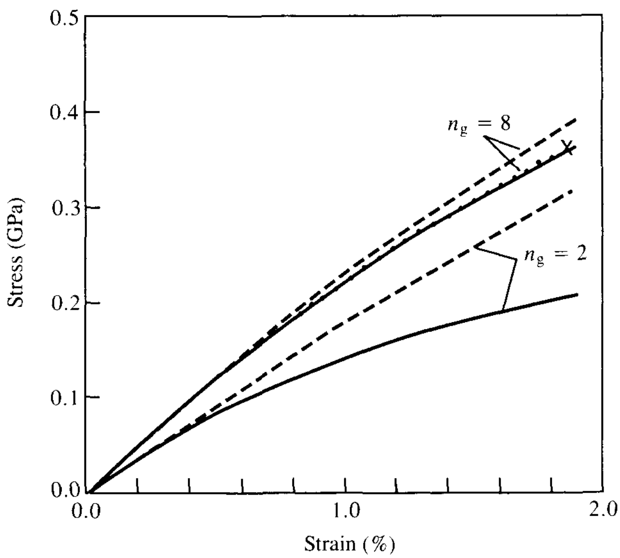

Hence material is transferred from one surface to the other. Subsequently, these transferred particles come loose due to the repeated contact.

In sliding wear, material loss is dominated primarily by adhesive mechanisms and secondarily by surface fatigue and abrasion; the abrasive component increases with increasing surface roughness. As compared with the abrasive wear conditions, the sliding wear process is much milder and is, consequently, extremely sensitive to the microstructure of the surface being worn. This is especially true for composite systems (Mody, Chou and Friedrich 1988).

In sliding wear, the sliding velocity (v) effects are manifested in frictional heating generated at the sliding interface. At some critical velocity, steady-state wear will no longer prevail, and the coefficient of friction and/or the wear rate will increase sharply. Reinforcing fibers usually increase the critical velocity of polymeric matrices. The influences of contact pressure (p) on sliding wear and of temperature on limiting pv values are also of major concern. Other factors include humid environments, counterface properties (i.e. surface roughness, density and height of the asperities), and the state of sliding interface (i.e. lubricants, films). The issue of fiber reinforcement raises additional important parameters, such as the type of fiber preforms, volume fraction and fiber orientation.

Woven forms of fiber reinforcement have demonstrated superior wear characteristics for self-lubricating bearings. Mody, Chou and Friedrich (1988) have investigated the sliding friction and wear of a neat thermoplastic matrix (PEEK), and examined the changes achieved by the incorporation of unidirectional continuous and two-dimensional woven carbon fibers. In their experiments, a pin-on-disc type wear testing machine is used; the specimen temperature, the torque generated at the sliding interface, the sliding velocity (in terms of revolutions per minute), the sliding distance (in terms of the number of revolutions made), and the sliding time are monitored. The sliding counterface is a polished steel surface.

The dimensionless wear rate (w), in the units of μm/m (depth worn per unit distance slid), is computed by using the measured mass loss (Δm) and density (ρ), along with the apparent contact area (A) and the sliding distance (L) in the following form:

$$w = \Delta m/(AL\rho) \tag{6.101}$$

The wear resistance of a material is the reciprocal of the wear rate (w^{-1}). The experiments show that, initially, wear progresses in a non-linear fashion. Later, as a definite sliding interface is established, the steady-state condition prevails, and the mass loss increases linearly with increases in sliding time.

Because of the anisotropic nature of fiber composites, it is important to identify the sliding directions relative to the fiber orientations. Three principal directions for the unidirectional continuous fiber composite have been identified, as shown in Fig. 6.53(a). Fibers in the plane of sliding and parallel to the direction of sliding are termed *parallel* (P). In-plane fibers oriented transverse to the direction of sliding are termed *anti-parallel* (AP), and fibers that stand normal to the plane of sliding are designated as *normal* (N). Following Mody, Chou and Friedrich (1988), six sliding directions are defined for a five-harness satin composite (Fig. 6.53b). The warp direction of the fabric, which has 80% of the fibers oriented in the direction of sliding, is referred to as the *parallel direction* (P). On the other hand, the filling direction of the fabric, which has 20% parallel to the sliding direction, is referred to as the *anti-parallel direction* (AP). Having thus defined the P and AP directions for the woven fabric system, consider a face perpendicular to the warp direction. This face will have a combination of fibers that stand normal to it, and parallel or transverse to it, depending on the direction of sliding on this face. Similarly, for the face orthogonal to the filling orientation of the fabric, the same reasoning prevails. From Fig. 6.53(b) it can also be concluded that the pair $N_{P(N,P)}$ and $N_{P(N,AP)}$ is the same as the pair $N_{AP(N,P)}$ and $N_{AP(N,AP)}$, if the warp and filling fiber yarns are the same fiber type. (The notations within the parentheses represent fibers of those orientations which are being slid.)

Sliding wear experiments have been conducted by Mody and

Fig. 6.53. Sliding directions with respect to the fiber orientation for (a) a unidirectional continuous fiber composite, and (b) a two-dimensional woven fabric composite. (After Mody, Chou and Friedrich, 1988.)

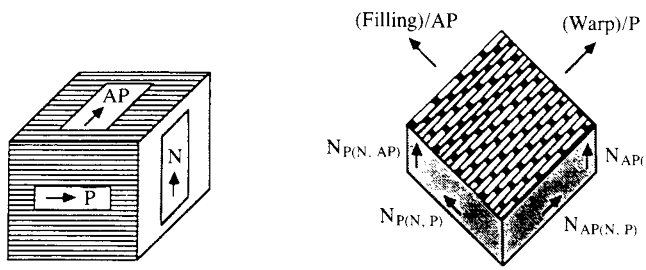

(a) (b)

colleagues for unreinforced PEEK matrix, unidirectional continuous fiber composites, and two-dimensional woven fabric composites at three temperatures (50, 150 and 240°C) and three pv values (0.3, 0.6 and 0.9 MPa m/s). Here p denotes contact pressure and v is sliding velocity. The variations of wear rate for these three material systems at 50°C and $pv = 0.3$ MPa m/s are summarized in Fig. 6.54. The wear rate of unreinforced PEEK is relatively high. In the case of unidirectional carbon/PEEK composites, the wear rates are highly anisotropic with the AP direction showing nearly twice the wear rate of the P and N orientations. For two-dimensional woven fabric composites, owing to the equivalence of the sliding directions $N_{P(N,P)}$ to $N_{AP(N,P)}$, and of $N_{P(N,AP)}$ to $N_{AP(N,AP)}$, four unique sliding directions are identified. These include the P-oriented surface, the AP-oriented surface, the surface containing a combination of N- and P-oriented fibers (N, P), and the fourth, which has a combination of N- and AP-oriented fibers (N, AP). Wear rates of these four surfaces at 50°C turn out to be quite uniform, and thus only their average value is indicated in Fig. 6.54. Models for the wear mechanisms of composites as functions of fiber orientation have been presented by Mody, Chou and Friedrich (1988, 1989).

6.13.2 *Notched strength*

Curtis and Bishop (1984) and Bishop (1989) have assessed the strength behavior of woven fabric composites. It has been

Fig. 6.54. Comparisons of the sliding wear rates of unreinforced PEEK, as well as unidirectional and two-dimensional fabric carbon/PEEK composites, at 50°C and $pv = 0.3$ MPa m/s. (After Mody, Chou and Friedrich 1988.)

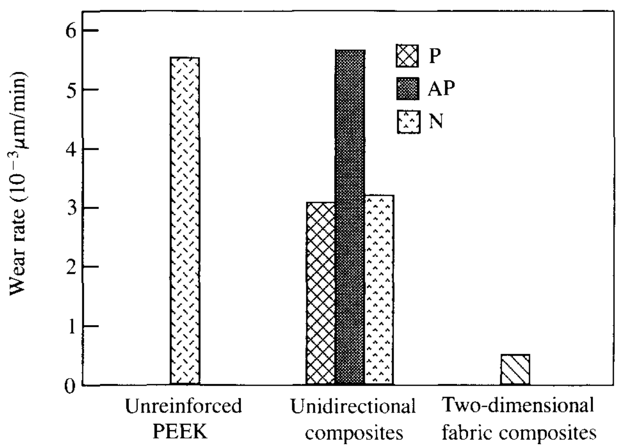

concluded that the woven fabrics are effective in limiting the growth of damage in laminated composites. It is suggested that woven fabrics be utilized in the 45° layers of a [0°/±45°] laminate with the unidirectional non-woven layers providing the needed stiffness and strength in the loading direction. Bishop has devised a scheme for laying up balanced fabric laminates without warping and unnecessary residual stresses; the line of crimped fibers in the fabric is an important parameter in the design of the lay-ups. The mechanical performance of plain and notched laminates under tensile, compressive and fatigue loadings has been reported by Bishop (1989).

To further demonstrate the damage tolerance of woven fabric composites, the example of molded-in holes is discussed below. The process of molding holes into the fabric at the laminate fabrication stage, instead of drilling the holes in the finished laminate, takes advantage of the microstructure of the woven preform. As a result, in the vicinity of the hole the fiber volume fraction is increased at regions where the stress concentrations are high, and the continuity of fiber is maintained.

Chang, Yau and Chou (1987) and Yau and Chou (1988) have examined the notched strength in tension and compression for Kevlar/epoxy and carbon/Kevlar/epoxy hybrid laminates. Specimens with molded-in holes exhibit tensile failure strengths which are up to nearly 40% higher than those of drilled specimens. Figure

Fig. 6.55. Molded-in holes in a carbon–Kevlar/epoxy $[0°]_{4s}$ laminate. (After Chang, Yau and Chou 1987.)

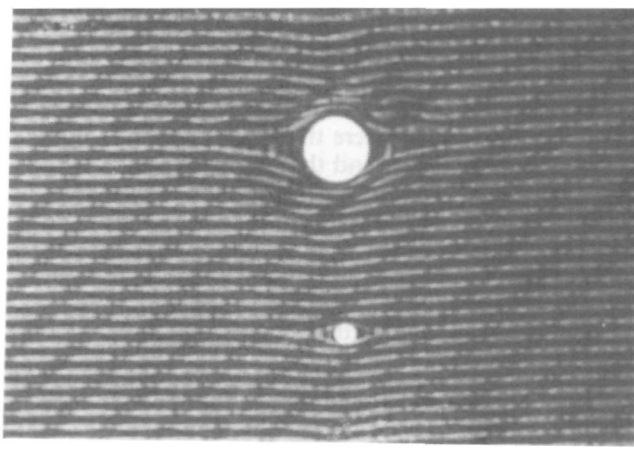

6.55 shows the fiber geometry around molded-in holes in a carbon–Kevlar/epoxy $[0°]_{4s}$ hybrid laminate. The compression behavior of woven carbon fiber reinforced epoxy composites with molded-in holes can be found in the work of Ghasemi Nejhad and Chou (1990a&b).